

PHOTON ABSORPTIOMETRY IN THREE COMPONENT SYSTEMS

PHOTON ABSORPTIOMETRY IN THREE COMPONENT SYSTEMS;  
BONE MINERAL AT THE SPINE  
AND IN THE PRESENCE OF A HIP PROSTHESIS

By

THOMAS JOSEPH FARRELL, M.Sc.

A Thesis

Submitted to the School of Graduate Studies  
in Partial Fulfilment of the Requirements  
for the Degree  
Doctor of Philosophy

McMaster University

February 1990

DOCTOR OF PHILOSOPHY (1989)  
(Physics)

McMaster University  
Hamilton, Ontario

TITLE: Photon Absorptiometry in Three Component Systems;  
Bone Mineral at the Spine and in the Presence of  
a Hip Prosthesis

AUTHOR: Thomas Joseph Farrell B.Sc. (University of Toronto)

B.Ed. (University of Toronto)

M.Sc. (University of Western  
Ontario)

SUPERVISOR: Dr. C.E. Webber

NUMBER OF PAGES: xiii,203

## ABSTRACT

The non-invasive measurement of the mass of bone is a clinically relevant problem. The bone is one component of a composite system. At the spine it may include fat, lean and bone mineral. At a hip prosthesis it may include soft tissue, bone mineral and metal. The measurement of the attenuation of photons of different energies can be used to determine the mass of one or all of the components of the composite system.

The first system is currently measured using only two photon energies by assuming that it is a two component system. A model was developed which predicts the effect of the third component, fat, and was validated using phantom measurements. Typical parameters for the volume and spatial distribution of fat *in vivo* were determined using CT scans. In combination with the model a median error of 8% is introduced by the third component. The feasibility of using a third energy to correct for the error was investigated. A model for the variance of the bone measurement normalized to emitted photon flux was developed. The optimal set of photon energies yielded a minimum value for the variance. However, this variance was excessively high, requiring a radiation dose 3000 times that for dual photon absorptiometry.

For the second system a triple photon absorptiometry technique was developed using the isotopes  $^{203}\text{Hg}$  and  $^{141}\text{-}$

Ce. The technique was shown to be valid, but the variance was high due to cross-over of high energy photons in the detector and by scattering. In order to make measurements with a precision of 1%, counting times of 70 hours are required. Monte Carlo simulations were performed to determine the optimal geometry to reduce cross-over from scattering. However, cross-over cannot be reduced sufficiently with  $^{203}\text{Hg}$  and  $^{141}\text{Ce}$ . A three isotope source is required to make clinical bone measurements at a prosthesis.

## ACKNOWLEDGMENTS

I wish to thank all those who were instrumental in making this thesis a reality. Foremost on this list is Dr. Colin Webber who is owed much gratitude for his continued patient guidance and support. The ideas for the projects originated with him and I was given the liberty to pursue them. The staff of the nuclear medicine department, at the reactor and in NRB, particularly Kenrik, were most supportive and deserve thanks for putting up with me.

Sincere gratitude must be given to my colleagues who provided interesting discussions, banal abstractions and generally contributed to making my time at McMaster rewarding. Special mention must be made of Alois, Ted and Dave - we all started together and were all in some measure part of Colin's clan.

I wish to acknowledge the important contribution of my wife Maureen for her continued support and enthusiasm over the long haul. Thank you also to our families for all the help they have given us. Finally I would like mention the little ones Emily and Peter, who, like this thesis are a product of my years at McMaster. They did not really help with the thesis, but they have made every day a little more pleasant to live.

## TABLE OF CONTENTS

	PAGE
DESCRIPTIVE NOTE .....	ii
ABSTRACT .....	iii
ACKNOWLEDGEMENTS .....	v
TABLE OF CONTENTS .....	vi
LIST OF FIGURES .....	ix
LIST OF TABLES .....	xiii
CHAPTER 1 - BONE MINERAL MEASUREMENTS .....	1
1.1 Introduction .....	1
1.2 A Description of Osteoporosis .....	2
1.3 Bone Mineral Measurement for Osteoporosis .	4
1.4 Patterns of Loosening of Hip Prosthesis ...	10
1.5 Methods of Evaluating Hip Prostheses .....	12
1.6 The Physical Basis for Triple Photon Absorptiometry .....	13
CHAPTER 2 - THE ERROR DUE TO FAT IN DPA MEASUREMENTS ..	21
2.1 Introduction .....	21
2.2 Model for error due to fat .....	23
2.3 Phantom measurements .....	27
2.4 In vivo fat distribution - single slice ...	29
2.5 In vivo fat distribution - multiple slice .	36
2.6 The effect of fat on DPA accuracy .....	41
CHAPTER 3 - FEASIBILITY OF TPA AT THE LUMBAR SPINE ....	44
3.1 Variance of TPA measurements .....	44
3.2 Selection of photon energies .....	49
3.3 Simulation of TPA .....	53
3.4 The effect of uncertainty in attenuation coefficients .....	56
3.5 Count requirements and relative dose in TPA .....	60
3.6 Feasibility of TPA at the spine .....	63
CHAPTER 4 - TRIPLE PHOTON ABSORPTIOMETRY FOR THE HIP ..	64
4.1 Physical Parameters for TPA .....	64
4.2 Development of TPA source .....	69
4.3 Transmission measurement procedure .....	76
4.4 Phantom materials .....	82
4.5 Simulation of phantom TPA .....	85
4.6 Phantom verification of TPA .....	87
4.7 Variance of Phantom TPA .....	99

CHAPTER 5 - DESCRIPTION AND VALIDATION OF MONTE CARLO CODE .....	108
5.1 Introduction .....	108
5.2 Pseudorandom number generator .....	109
5.3 Overview of Monte Carlo code .....	113
5.4 Mechanics of photon transport simulation ..	116
5.5 Scoring scatter flux .....	118
5.5.1 Mechanics of analogue scoring ....	120
5.6 Variance reduction .....	121
CHAPTER 6 - THE FEASIBILITY OF TPA AT THE HIP .....	127
6.1 Variance of TPA .....	127
6.2 Intensity ratios of incident beams .....	130
6.3 Monte Carlo simulation parameters .....	134
6.4 Energy response of the 5.08 cm NaI detector .....	137
6.5 Scatter flux estimation .....	141
6.5.1 Single scatter flux .....	141
6.5.2 Multiply scattered flux .....	146
6.6 Cross-over and variance for varying geometry .....	153
6.7 Source Strength Requirements and feasibility of TPA .....	157
CHAPTER 7 - CONCLUSION .....	160
7.1 Bone mineral absorptiometry at the spine ..	160
7.2 TPA at the hip prosthesis .....	163
7.3 TPA: a final word .....	164
BIBLIOGRAPHY .....	166
APPENDIX 1 - STATISTICAL TESTS OF RANDOM NUMBER GENERATOR .....	175
APPENDIX 2 - SIMULATION PROCESSES .....	179
A2.1 Photon creation .....	179
A2.2 Path and path length determination .....	179
A2.3 Determination of interaction type .....	181
A2.4 Coherent scattering .....	182
A2.5 Compton Scattering .....	184
A2.6 Calculation of new direction cosines .....	187
APPENDIX 3 - BASIC CODE OF MONTE CARLO SUBROUTINES ....	192
APPENDIX 4 - BASIC CODE FOR INTENSITY RATIO CALCULATION .....	196

APPENDIX 5 - CONVOLUTION OF CIRCULARLY SYMMETRIC FUNCTION WITH A UNIFORM CIRCLE .....	197
APPENDIX 6 - GEOMETRIC EFFICIENCY OF DETECTOR WITH PHOTON ANGLE .....	202

## LIST OF FIGURES

Figure	Description	Page
1.1	Geometry of bone mineral measurement techniques .....	5
1.2	Equivalent representations for transmission measurements .....	15
2.1	Dual photon bone mineral image obtained using the modified rectilinear scanner .....	28
2.2	Plot of bone mineral error against $\Delta f(d-t)/t$ .....	30
2.3	CT transverse images through a lumbar vertebra showing the shape of the region of interest and the histograms of CT numbers .....	32
2.4	Location of measurement regions on CT image ...	33
2.5	Fat deviation for 11 single scan measurements at each region .....	35
2.6	Fat deviation for 15 multiple scan patients including individual and mean measurements .....	37
2.7	Fat deviation as a function of age .....	39
2.8	Fat deviation as a function of fat fraction at the spine .....	40
2.9	Projected error in the measurement of bone mineral as a function of bone mineral density .	42
3.1	Normalized variance for different combinations of the other two energies .....	51
3.2	Normalized variance for different forms of the factor $f(E)$ .....	52
3.3	Normalized variance for different crossover values .....	54
3.4	Model used for simulation of TPA at the spine .	55
3.5	Algorithmn for generating Gaussian variates ...	57

3.6	Simulated TPA images for elliptical cylinders of bone with various thicknesses .....	58
3.7	RMS deviation bone mineral content as a function of number of transmitted photons and crossover .....	59
3.8	Frequency distribution of normalized variance generated by Monte Carlo simulation .....	61
4.1	Schematic diagram of hip prosthesis .....	66
4.2	Mass attenuation coefficients for tissue and Vitallium .....	68
4.3	NaI spectra of 203-Hg and 141-Ce .....	75
4.4	Schematic diagrams of source containers, and source holder .....	77
4.5	Transmitted intensity of 203-Hg photons through steel .....	80
4.6	Schematic diagrams of detector holder and collimator and source holder and lead castle ..	81
4.7	System deadtime as a function of count rate ...	83
4.8	Phantom geometry used for TPA simulation .....	88
4.9	Simulated TPA images for rectangular aluminum regions with various thicknesses .....	89
4.10	Phantom material thicknesses for various configurations .....	91
4.11	Phantom material thicknesses for TPA pseudoscans .....	101
4.12	Phantom pseudoscans for rectangular plates of aluminum with various thicknesses .....	106
5.1	Division of set of $p=10$ words of length $q=6$ into a set of 6 shift registers of 10 bits ....	111
5.2	Scheme of random number generator .....	112
5.3	Mechanisms for photons to be transmitted through a slab of tissue .....	115

5.4	Geometry of collision density estimator .....	119
5.5	Reselection volume for collision density estimator .....	122
5.6	Comparison of analogue scoring with direct scoring for different reselection lengths for a scoring point on the pencil beam .....	125
5.7	Comparison of analogue scoring with direct scoring for different reselection lengths for a scoring point not on the pencil beam .....	126
6.1	Schematic diagram of geometry for calculation of intensity ratio for different collimators ..	131
6.2	Fraction of total flux as a function of radius of detector collimator for source collimator used for phantom measurements .....	133
6.3	Intensity ratio as a function of radius of detector collimator for source collimators of various thickness .....	135
6.4	Probability of counting pulse in Tl X-ray window as a function of photon energy .....	140
6.5	Mean detector response for 10 keV intervals as a function of photon energy for Tl X-ray window .....	142
6.6	Mean detector response for 10 keV intervals as a function of photon energy for 279 keV photon window .....	143
6.7	Single scatter Tl X-ray probability as a function of radius from pencil beam for typical phantom configuration using Tl X-rays .....	144
6.8	Single scatter probability for 279 keV and Tl X-ray window as a function of radius from the pencil beam for a typical phantom configuration using 279 keV photons .....	145
6.9	Multiple scatter probability for Tl X-ray window for typical phantom configuration as a function of radius from the pencil beam and cosine of polar angle .....	148

6.10	Multiple scatter probability for Tl X-ray window for 279 kev photons as a function of radius for $\cos(\theta)=1$ .....	149
6.11	Cross-over due to scatter as a function of radius of detector collimator for source collimators of various radii .....	155
6.12	Variance of bone mineral measurement per unit counting time as a function of detector collimator radius for source collimators of various radii .....	156
A1.1	Frequency distributions for some random number statistical tests .....	177
A2.1	Frequency distributions generated by sampling Coherent scatter angle for water .....	185
A2.2	Scheme for random sampling Compton scattering angle due to Kahn .....	188
A2.3	Frequency distributions generated by sampling incoherent scatter angle for water .....	189
A2.4	Scheme for random sampling sine and cosine of azimuthal angle .....	190
A5.1	Evaluation of convolution of a ring with a uniform circle .....	199
A5.2	Plots of radial functions of a ring of unit height, a uniform circle and the convolution of the ring and the circle .....	201
A6.1	Evaluation of geometric efficiency of detector collimator for a point at the entrance of the colimator and a given polar angle .....	203

## LIST OF TABLES

Table	Description	Page
2.1	The value of the fat effect parameter by source of linear attenuation coefficients .....	26
4.1	Elemental composition of Vitallium FHS .....	65
4.2	Isotopes identified in preliminary spectra ....	71
4.3	Isotopes produced by irradiation of Hg for three days .....	72
4.4	Isotopes produced by irradiation of Ce for three days .....	73
4.5	Composition of Vitallium and Stainless Steel ..	84
4.6	Mass attenuation coefficients for phantom materials .....	86
4.7	Fitted and measured linear attenuation coefficients for phantom materials .....	93
4.8	Cross-over factors for phantom configurations .	95
4.9	Attenuation factors for phantom configurations .....	97
4.10	Aluminum thickness by TPA and expected values .	98
4.11	Linear attenuation coefficients of phantom materials from pseudo-scans and expected values .....	103
4.12	Aluminum thickness from pseudo-scans and expected values .....	105
6.1	Isotopes used to determine detector response ..	139
6.2	Scatter flux ratios for some phantom configurations .....	152
A1.1	Chi-squared values for statistical tests of random number generator .....	178

## CHAPTER 1

### BONE MINERAL MEASUREMENTS

#### 1.1 Introduction

Noninvasive techniques for the measurement of skeletal status have been available since the inception of medical radiology. More recently, the development of sophisticated techniques allow the quantitative measurement of bone mineral content with increasing accuracy and precision. Each technique has its merits and deficiencies when compared with other methods. Their relative value must be determined by assessment of how they achieve their primary purposes, to differentiate a diseased population from a normal population, and to monitor the progress of the disease or treatment for the disease. These techniques will generally prove useful for metabolic bone diseases or other conditions which involve reduction in bone mineral content, or osteopenia.

There are two related problems which fit into this category. The first involves the measurement of lumbar spine bone mineral content for the assessment of osteoporosis. The second involves the measurement of femoral shaft bone mineral content following the implantation of a metal hip prosthesis. In this work the feasibility of a new technique

which utilizes the transmission of photons of three different energies, triple photon absorptiometry, will be examined.

### 1.2 A Description of Osteoporosis:

Osteoporosis is defined as the reduction of the amount of mineralised bone, and it involves the deficiency of both the bone mineral hydroxyapatite as well as the collagen matrix upon which the mineral is laid (Mazess, 1979). The osteoporotic bone appears normal histologically (Wasserman and Berzel, 1987) and there are no biochemical changes which are associated with other bone disorders such as osteomalacia and hyperparathyroidism (Houston, Joiner and Trounce, 1975). The risk of fracture is elevated; atraumatic fracture is frequently the initial presentation of the otherwise asymptomatic condition.

The skeletal system is composed of two different types of bone, compact cortical bone and the less dense trabecular bone. The most frequent fracture sites are those with greater proportions of trabecular bone, namely the vertebrae, the proximal femur and the distal radius (Melton and Riggs, 1983). Twenty-five percent of women over 60 years of age will have vertebral fractures while 32% of women over 90 will have hip fractures (Wasserman and Barzel, 1987). Studies have indicated that reduction in bone mineral content may be an important risk factor for fracture at

these sites, and that a fracture threshold may exist (Bohr and Schaadt 1983, Melton and Riggs 1983, Melton et al 1986).

The loss of bone mineral is attributed to an imbalance in the normal processes of bone formation and resorption. In normal aging the average rate of bone loss for females would be 1% per year between the ages of 45 and 75 slowing to 0.4% per year for ages greater than 75. Peak bone loss rates may be as high as 3% per year for a short time period following menopause or oophorectomy (Wahner 1987). In osteoporotic females the rates of loss may be 50% higher than for normals, so that the typical 60 - 70 year old osteoporotic may have bone mineral content 10 to 15% lower than normal counterparts (Mazess 1979, Riggs et al 1982).

The technique chosen for bone mineral measurement should satisfy the following criteria: the bone mineral content at the measurement site should be correlated with the fracture risk or the fracture threshold at an important site; for example the bone mineral at the distal radius is used to predict the risk of vertebrae fracture, and the reproducibility should be sufficient to demonstrate clinically significant (5%) differences in bone mineral content over protracted or relatively short periods of time (Wahner 1983). As will be presented in the next section the presently available array of techniques meet these criteria

with varying degrees of success.

### 1.3 Bone Mineral Measurement for Osteoporosis:

A number of non-invasive techniques for the measurement of bone mineral content have developed, each of which involves the interaction of radiation with tissue through absorption or scattering processes. These interactions are either measured directly, or indirectly by transmission measurements, the latter being the predominant method. There are a number of comprehensive reviews of these methods (Wahner, Dunn, and Riggs, 1983. Mazess, 1983. Goodwin 1987) so only a brief discussion of their relative merits will follow.

Compton and coherent scattering are two related techniques which measure scattering directly by using a collimated beam of gamma photons to irradiate a small volume of trabecular bone, usually in the calcaneus (with predominantly trabecular bone it is thought to be correlated with overall skeletal status even though it is rarely a fracture site itself [Vogel Wasnich and Ross 1988]). The intensity of the photons scattered out of the bone at a given angle is the product of the incident intensity of the beam, the scattering volume and the macroscopic scattering probability at that angle for the tissue (figure 1.1). The latter factor is the product of the effective atomic differential cross-section for the tissue and the density of

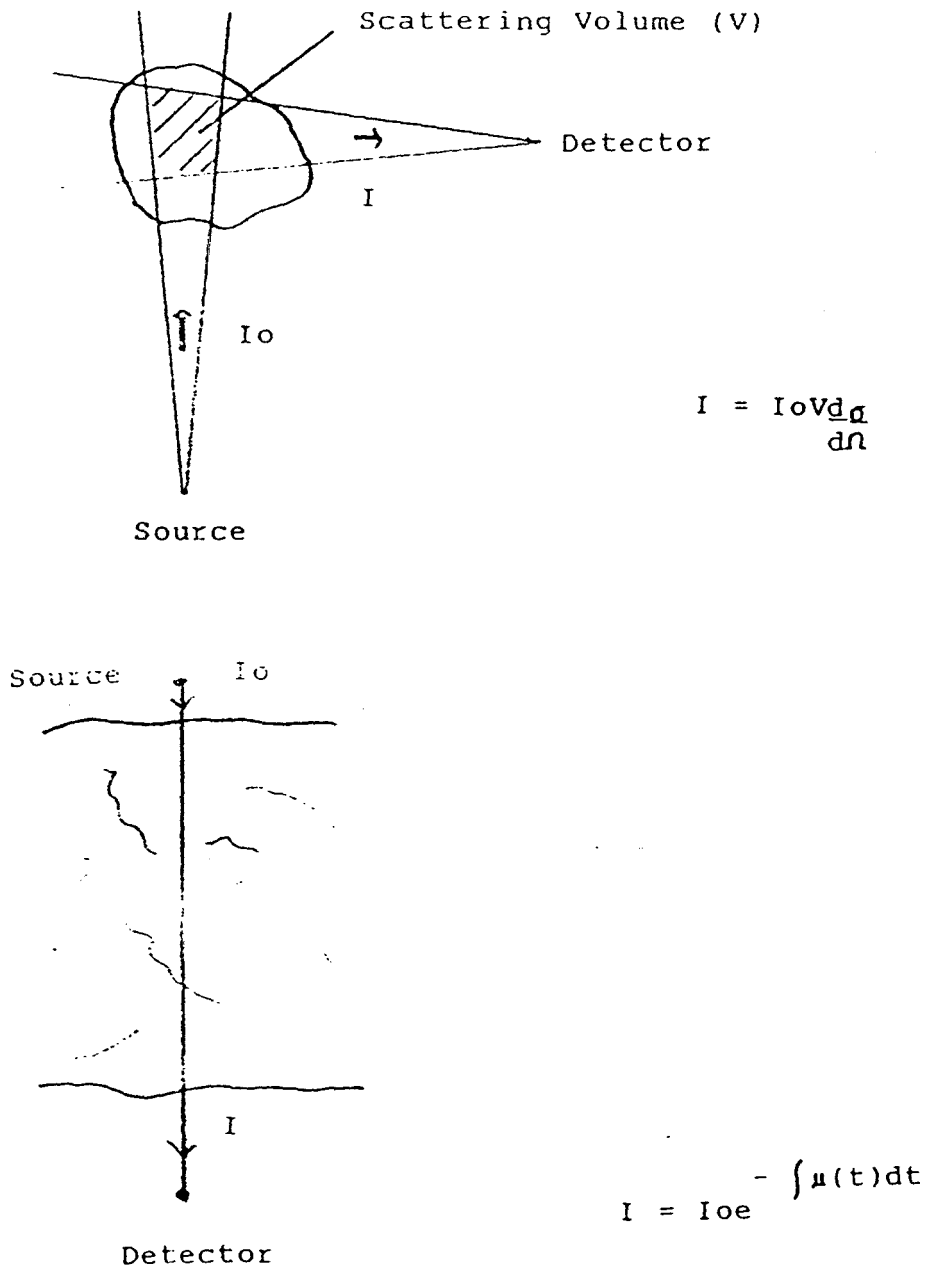


FIGURE 1.1 Geometry of bone mineral measurement techniques: a) Scattering measurements, b) Transmission measurements.

the tissue, both of which are related to bone mineral content. The scattered intensity is affected by attenuation of both the incident and scattered beams and by multiple scattering.

Compton scattering using  $^{153}\text{Sm}$  (Garnett et al 1973) or  $^{137}\text{Cs}$  (Hazan et al 1977) was the first of these techniques to be used clinically. The reproducibility of the measurements was of the order 1.5%, however the technique was affected by multiple scatter with typical errors of 10% (Webber 1981). More recently coherent scattering has been investigated (Kerr et al 1980, Karrellas et al 1983, Ndlovu personal communications). It is expected that this technique may be more sensitive to differences in bone mineral content than Compton scattering since the atomic differential cross-section for coherent scattering is more strongly dependent upon atomic number than is Compton scattering.

Neutron activation analysis of calcium involves the direct measurement of the absorption of a beam of neutrons by the tissue. Radioactive  $^{49}\text{Ca}$  is produced by the capture of thermal neutrons by  $^{48}\text{Ca}$ . This decays with a half-life of 8.9 minutes, emitting a 3.1 Mev gamma ray isotropically. The intensity of the emitted photons is a product of the neutron flux, the volume of irradiation and the macroscopic absorption probability, which is the product of the atomic absorption cross-section and the density of  $^{48}\text{Ca}$ . The

emitted intensity is affected by attenuation of both neutrons and photons, as well as by interference from other neutron activation products, such as  $^{24}\text{Na}$  (Cohn 1981).

The choice of irradiation site ranges from the hand or torso to the whole body with isotopic sources, accelerators and reactors used to produce the neutrons. Each choice of site has its limitations. The hand is convenient to measure, but may not be highly correlated with fracture risk. The torso site includes the vertebrae, but measurements here have relatively high standard deviations (4%). The whole body measurement is accurate (5%) and precise (1%), but measurements do not distinguish high fracture risk sites (Cohn 1981).

Transmission methods are used to determine bone mineral content by measurement of the attenuation of photons in the diagnostic energy range through the tissue. These methods utilize the attenuation factor,  $Y$ , which is based upon the fundamental relationship between the incident intensity of the radiation,  $I_0$ , and the transmitted intensity,  $I$ , as given in equation 1.1 (figure 1.1).

$$Y = \ln(I_0/I) = \int \mu(t)dt \quad 1.1$$

The attenuation factor is equal to the integral of  $\mu(t)$ , which is the macroscopic linear attenuation coefficient and is a function of the energy of the radiation and the atomic composition of the tissue. The various transmission methods

extract bone mineral content differently from the attenuation factor. These differences affect the validity of each method.

Single photon absorptiometry, SPA, measures the attenuation of a collimated beam of photons of a single energy through the tissue (Cameron and Sorenson 1963, Karajalainen 1973). Since the attenuation is due not only to the bone mineral but also the overlying soft tissue, the attenuation factor is compared to the attenuation through an equal thickness of soft tissue, the difference being proportional to the lineal density of bone mineral. In practice one assures an equal transmission thickness by immersion in water, so the technique is restricted to such locations as the distal radius or the os calcis.

The precision of the technique is quite good, with long term reproducibility of 1.5%. This is degraded by repositioning errors of 4% (Wahner, Riggs and Beabout 1977) so that precision may be of the order 7% (Mazess, Cameron and Miller 1972). The accuracy is affected by fat, a constituent of soft tissue, which is not compensated for by immersion in water. Errors due to fat have been estimated to range from 8.5% (Wooten, Judy and Greenfield 1973) to 15% (Zeitzi 1972).

In dual photon absorptiometry, DPA, the transmission of photons of two different energies is measured (Wilson and

Madsen 1977, Dunn, Wahner and Riggs 1980, Krolner and Pors Neilsen 1980). If the tissue is composed of only two components, such as soft tissue and bone mineral, then the differential attenuation of the two photons is used to determine the thickness of either component (this will be described in detail later). The effect of fat can be reduced by choosing a baseline in regions with no bone mineral.

The technique has the advantage that it does not require constant thickness of tissue and can be used for the hip, lumbar vertebrae or the whole body. The long term reproducibility for patients is of the order 4% and may be as low as 2.5% for modern machines. Errors can be introduced by inhomogeneous distributions of fat, the magnitude of which are examined in this study.

Quantitative computed tomography, QCT, uses tomographic reconstruction to obtain the transaxial distribution of attenuation coefficients in Hounsfield units. The trabecular bone can be isolated within the vertebrae or the hip uncomplicated by overlying tissue using either a single energy or a dual energy approach (Cann and Genant 1980, Reiser and Genant 1984). Reference standards which contain well defined amounts of bone equivalent material are used to calibrate the Hounsfield units to effective mineral density.

The reproducibility is of the order of 2.5% for

single energy QCT, but is worse at 21% for the dual energy approach (Goodwin 1988). The accuracy is better for dual energy QCT than for single energy which can have errors due to fat of the order 20% (Laval-Jeantet et al 1986).

Clearly each of these techniques has its deficiencies, and no one method is ideal. DPA may seem to be the best approach at present for choice of site, precision, and low radiation dose. The effect of inhomogeneous fat needs to be addressed, and perhaps remedied with triple photon absorptiometry.

#### 1.4 Patterns of Loosening of Hip Prosthesis:

The evolution of the surgical procedure of total hip arthroplasty has been assisted by a combination of gradual development and engineering of the prosthesis and major advances in the selection of biocompatible materials. The first of these was the development of the metal alloy 'Vitallium', composed of chromium, cobalt and molybdenum by Venable and Stuck in 1938. This alloy is biologically inert and has the necessary strength, and durability to be used for load bearing implants. The second major advance was the introduction by Charnley of high density polyethylene for bearing surfaces in the 1960s. This has appropriate friction and wear characteristics for joint linings. The prosthesis is designed to withstand the stresses of normal motion over extended periods. Unfortunately, such mechanical devices do

not have the self regenerative capacity of the original biological tissue so that wear is inevitable, with the end result being failure of the prosthesis primarily by loosening (Bechtol 1983, Haberman 1986).

The incidence of loosening of the femoral prosthesis has been described in a large number of cases and varies widely from study to study. The rates vary from 1.1% to 50%, which reflects real differences in surgical technique as well as differences in clinical definition of loosening (Paterson et al 1986, Haberman 1986). Loosening can be caused by infection, but the majority of loosening is aseptic and may be associated with resorption of bone (Freiberger 1986). The incidence of calcar resorption ranges from 16% to 69% (Haberman 1986) with calcar resorption reported in greater than 50% of loosening cases and femoral cortex resorption in 5% of cases (Carlsson and Gentz 1980).

Loosening associated with bone resorption may follow different patterns. Atrophy of the supporting cortical or trabecular bone may occur due to redistribution of stress in the presence of the prosthesis (Woo et al 1976). Alternatively, resorption at the bone-cement/prosthesis interface may be due to histiocytic reaction to wear and corrosion products (Willert and Semlitsch 1976, Winter 1976). Radiological evidence for prosthesis loosening relies upon demonstration of resorption of bone at the bone

prosthesis interface.

### 1.5 Methods of Evaluating Hip Prostheses:

As mentioned in the previous section, the incidence of prosthesis loosening depends strongly upon the clinical definition of loosening. Assessment of loosening can be classified into two categories: demonstration of degradation of the bone-cement/prosthesis interface and measurement of movement between the bone and the prosthesis.

The simplest technique which fits the first category is direct visualization of a radiolucent zone adjacent to the stem of the prosthesis (Paterson, Fulford and Denham 1986). The other techniques rely upon intra-articular injection of some agent which can enter the region of resorbed bone for visualization. Examples of this include radionuclide arthrography using  $^{99m}\text{Tc}$  sulphur colloid imaged with a gamma camera (Uri et al 1984), contrast arthrography with radiological contrast agents using either standard radiographs or subtraction techniques (O'Neil and Harris 1984) and scintigraphy with  $^{99m}\text{Tc}$  MDP and  $^{67}\text{Ga}$  which assesses both increased bone activity and infection (Rushton et al 1982).

The second type of technique, roentgen stereophotogrammetric analysis, RSA, uses tantalum markers to demonstrate relative movement of the prosthesis and bone (Mjoberg et al 1986). The markers are placed in the

trochanters and act as a reference for the position of the femoral prosthesis. Serial radiographs can demonstrate displacement associated with loosening.

While each of these techniques is suitable for demonstration of a loose prosthesis, none assesses the bone during the loosening process. The high attenuation of photons by the metal Vitallium makes standard bone content techniques unsuitable at this site. While some attempts have been made to modify CT images using multiplanar reconstruction (Fishman et al 1986) or by interpolation of Hounsfield numbers at the prosthesis (Seitz and Ruegsegger 1982), these do not produce reliable measurements of the bone mineral content about the prosthesis. Triple photon absorptiometry may prove a viable method to assess the bone mineral at this site.

#### 1.6 The Physical Basis for Triple Photon Absorptiometry:

The attenuation of a beam of photons of energy  $E$  by a complex system like the human body can be described by the attenuation factor,  $Y(E)$ , which is the natural logarithm of the ratio of the original intensity,  $I_0$ , and the attenuated intensity,  $I$  (which is an energy dependent version of expression 1.1). The attenuation factor is given by the integral of the linear attenuation coefficient,  $\mu$ , at each position,  $x$ , along the path length through the body (figure 1.2). That is

$$Y(E) = \ln(I_0/I) = \int \mu(E,x) dx \quad 1.2$$

In general  $\mu(E,x)$  is a function of the local density and atomic composition of the tissue. It can be represented by the weighted sum of the linear attenuation coefficients of certain basis phases,  $\phi$  (figure 1.2). In such cases the attenuation factor is described as the sum of attenuation factors due to equivalent thicknesses of the basis phases. That is

$$Y(E) = \sum [\mu(E,\phi)t(\phi)] \quad 1.3$$

The equivalent thicknesses can be recovered by determining the attenuation factor at different energies by transmission measurements. If  $\mu$  represents the matrix of linear attenuation coefficients for the different phases at the different energies then

$$\tilde{Y} = \mu \tilde{t} \quad 1.4$$

where  $Y$  and  $t$  are the attenuation factor and thickness matrices respectively. If the matrix  $\mu$  is non-singular, the equivalent thicknesses are found from the inverse matrix as shown in equation 1.5.

$$\tilde{t} = \mu^{-1} \tilde{Y} \quad 1.5$$

For DPA, two basis phases, soft tissue and bone mineral, are utilized to describe the attenuation of the body. However, other two phase basis sets have been suggested, examples of which include photoelectric and

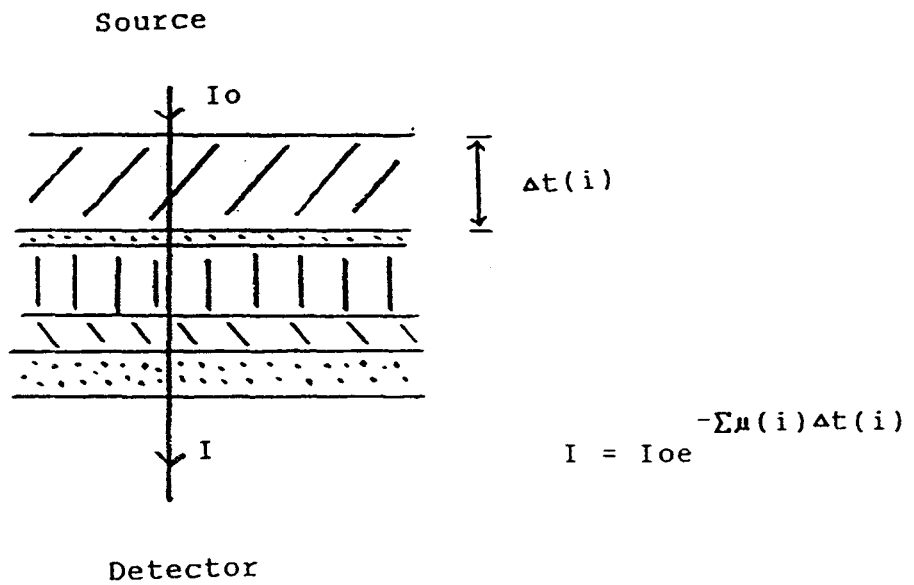
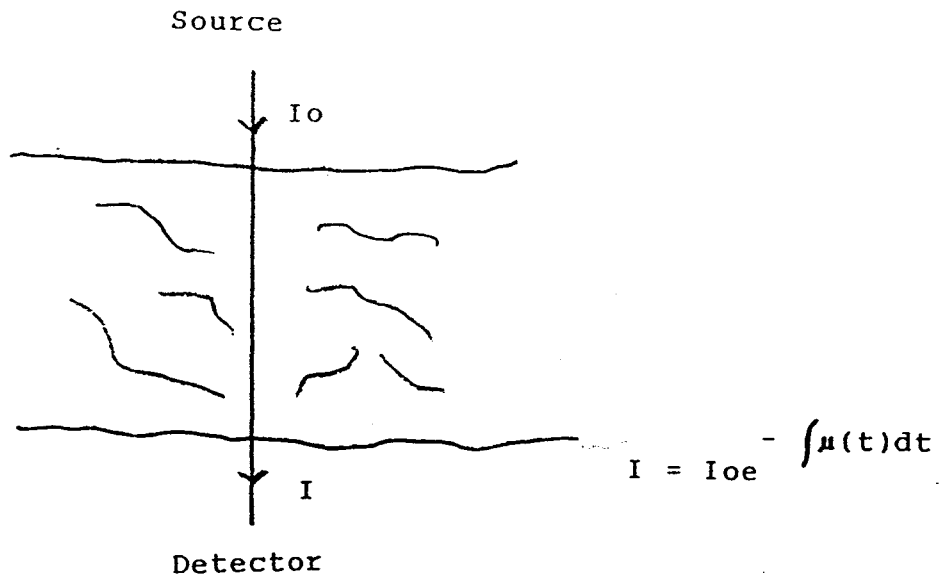


FIGURE 1.2 Equivalent representations for transmission measurements.

Compton phases, water and CaCl, Lucite and aluminum (Alvarez and Macovski, 1976; Avrin, Macovski and Zara, 1978; Jackson and Hawkes, 1983; Lehmann et al, 1981; Hawkes, Jackson and Parker, 1986). These have been shown to describe the attenuation of photons by tissue to 1-2% over the diagnostic energy range. However divergences increase to 5% for higher atomic numbered elements such as copper and iodine.

Three phase basis sets have been utilized for removal of iodine contrast from soft tissue and bone images using iodine K-edge techniques (Reiderer, Kruger and Mistretta, 1981). For TPA, two separate three component systems will be considered: bone mineral, lean tissue and fat, and bone mineral, soft tissue and Vitallium. The most natural basis phases to choose will be the constituent components themselves. The feasibility of TPA will depend upon the linear independence of the linear attenuation coefficients of the components at the chosen photon energies.

Some insight into this can be obtained by consideration of the possible photon interactions with the materials at the various photon energies. The linear attenuation coefficient of a material,  $\mu$ , at an energy,  $E$ , is proportional to the sum of the cross-sections for the various photon interaction processes,  $\sigma$ , at the given energy, as in expression 1.6.

$$\mu(E,m) = K \sum \sigma(E,i) \quad 1.6$$

Frequently the cross-sections can be expressed as the product of two terms, one which includes the energy dependence,  $\sigma'(E,i)$ , and the other the atomic number dependence,  $f(Z,i)$ , where  $Z$  is the effective atomic number of the material for a particular process. In such a case, the cross-section can be written as in expression 1.7.

$$\mu(E,m) = \sum f(Z,i) \sigma'(E,i) \quad 1.7$$

Since the term on the left is in fact a matrix element, substitution into equation 1.4 gives a new matrix equation with matrices containing the energy dependence and the atomic number dependence separately.

$$\tilde{Y} = \tilde{f} \tilde{\sigma}' \tilde{t} \quad 1.8$$

The inverse matrices can be used to determine the equivalent thicknesses of the interaction processes if both matrices  $\tilde{f}$  and  $\tilde{\sigma}'$  are non-singular as in equation 1.9.

$$\tilde{t} = \tilde{\sigma}'^{-1} \tilde{f}^{-1} \tilde{Y} \quad 1.9$$

This result suggests that the number of phases that can be recovered from the transmission data is limited by the number of photon interaction processes. The validity of this result will depend upon the nature of the photon interaction processes. For photons in the diagnostic radiology range there are three atomic processes of consequence: incoherent scattering, coherent scattering and

photoelectric absorption. These have been described in great detail by others, (Evans 1955, Hobbie 1987) so only a brief discussion of the relevant points will be given here.

The first of these, incoherent scattering, involves Compton scattering of the incident photon by a single electron of the atom. The differential cross-section for scattering by a free electron is described by the Klein-Nishina formula. Integration over all scattering angles yields the total cross-section for a free electron as given in equation 1.10, with the photon energy,  $E$ , in electron rest mass units.

$$\sigma \propto \frac{(1+E)}{E} \frac{2(1+E)}{1+2E} - \frac{\ln(1+2E)}{E} \quad 1.10$$

$$+ \frac{\ln(1+2E)}{2E} - \frac{1+3E}{(1+2E)}$$

A first approximation of atomic differential cross-sections is given by multiplication of the free electric cross-section by the number of electrons,  $Z$ , which is in the form of equation 1.7. These must be modified by atomic form factors which reduce the cross-section by restricting scattering to events which deliver more than the binding energy of the electron. These effects are small, and primarily affect small scatter angles. Nonetheless, the total cross-sections deviate by a small fraction from a simple multiplication of the free electron cross-section and atomic number.

The second interaction, coherent scattering, involves the non-relativistic scattering of the photon by all the electrons of the atom. The differential cross-section for a free electron is given by the Thompson cross-section. The atomic differential cross-section is given by multiplication of the Thompson cross-section by the square of a form factor,  $F(x,Z)$ , where  $Z$  is the atomic number and  $x$  is the momentum transferred to the atom and is a function of photon energy and scatter angle. The form factor is given as the Fourier transform of the charge density of the atom, and at a given angle and photon energy is approximately proportional to the square of the atomic number. Thus the differential cross-section can be expressed as the product of an energy and an atomic number dependent term, in the form of equation 1.7. Unfortunately the total cross-section is not so easily placed into the form of equation 1.7, and is only approximately proportional to the square of atomic number. Moreover, since the scattering is strongly forward peaked, the total interaction is very small relative to the other interactions, and in broad-beam conditions may be negligible.

The third interaction, photoelectric absorption, involves complete absorption of the photon, with the energy and momentum taken up by the entire atom. Theoretical description of the process has proven difficult over all

energy ranges, but an empirical description of the cross-section is given by equation 1.11, where E represents the photon energy in electron rest mass units.

$$\sigma \sim Z^n E^{-7/2} \quad 1.11$$

This is in the form of equation 1.7, but unfortunately the energy exponent is only valid over certain energy ranges and requires slight modifications to cover the complete range. Moreover there is not complete agreement as to the exponent for the atomic number term ranging from  $n=4$  (Evans 1955) to  $n=5$  (Hobbie 1987).

Overall, the three interaction cross-sections are described by expression 1.7 with small deviations. One of these interactions, coherent scattering, does not contribute greatly to the total interaction of the photon, and in some geometries may be negligible. It is not surprising then that two components accurately describe the attenuation of photons to within small percentages. Triple photon absorptiometry must exploit the small differences due to binding effects in Compton scattering, due to coherent scattering and due to changes in exponents in photoelectric absorption to analyze a three component system. This work will be an examination of the necessity and the feasibility of triple photon absorptiometry for the two systems of interest mentioned previously.

## CHAPTER 2

### THE ERROR DUE TO FAT IN DPA MEASUREMENTS

#### 2.1 Introduction

The theory of multiple photon absorptiometry has been described in the previous chapter, as have several methods of bone densitometry. In this chapter dual photon absorptiometry will be examined in detail. In particular the validity of a dual photon approach to solve a composite system which clearly has more than two components will be examined by determining the magnitude of errors due to fat inhomogeneities in bone mineral measurements at the lumbar spine.

Dual photon absorptiometry (DPA) has certain advantages over other techniques as discussed earlier. The essence of the technique is to assume that the body consists of a two component system, namely soft tissue and bone, and to exploit the different attenuation characteristics of the components at two different photon energies in order to calculate the mass of bone in the beam (Wilson and Madsen 1977, Dunn, Wahner and Riggs 1980, Krolner and Pors Nielsen 1980).

In reality the body consists of at least three components: bone, lean tissue, and fat tissue. If

unaccounted for, the effect of the fat tissue is to reduce the apparent bone mass measurement. However, if it is assumed that the fat is distributed homogeneously, measurements in regions in which there is no bone can be used to establish a baseline, or a relative soft tissue component. This baseline can be used to calculate a corrected bone mass in other regions.

Transmission measurements through the abdomen at the lumbar spine will include fat arising in three principal forms: fat layers which surround organs, fat within bone marrow and layers of subcutaneous fat. Inhomogeneities will most likely be due to fat surrounding organs which themselves are not distributed uniformly within the body.

The effects of inhomogeneous fat distribution have been investigated in the past. Wahner et al (1985) used phantoms and cadaver spines to measure the effects of marrow fat. They found negligible errors provided the aorta was not highly calcified and provided there was not excessive fat adjacent to the vertebrae. Roos et al (1980) measured cadaver sections and found median errors of 10% due to fat adjacent to the spine. Krolner and Pors Nielsen (1980) using tissue substitutes found that significant errors could be introduced by non-uniform fat layers, but that careful selection of the baseline could minimize the error. This work incorporates in vivo measurements of fat distributions

with a model for the errors introduced by fat distributions to estimate in vivo DPA errors that can be expected.

## 2.2 Model for error due to fat

An analytic expression for the error due to fat can be derived from the equations which describe attenuation of photons as given in equation 1.3. For the dual photon system using a high energy,  $E_1$ , and a low energy,  $E_2$ , to find the mass of bone,  $m(b)$ , and the mass of soft tissue,  $m(s)$ , this can be written as

$$Y(E_1) = \mu(b, E_1)m(b) + \mu(s, E_1)m(s) \quad 2.1a$$

$$Y(E_2) = \mu(b, E_2)m(b) + \mu(s, E_2)m(s) \quad 2.1b$$

These can be solved to give the mass of bone  $m(b)$  as

$$m(b) = \frac{(Y(E_1)\mu(s, E_2) - Y(E_2)\mu(s, E_1))}{D(s, b)} \quad 2.2$$

where the denominator is the determinant of the matrix of the mass attenuation coefficients and in general is given by

$$D(s, b) = \mu(s, E_1)\mu(b, E_2) - \mu(s, E_2)\mu(b, E_1) \quad 2.3$$

The effect of a layer of fat is to change the attenuation factors in equation 2.1 by the addition of the attenuation due to fat as given by

$$Y(E_1)' = Y(E_1) + \mu(f, E_1)m(f) \quad 2.4a$$

$$Y(E_2)' = Y(E_2) + \mu(f, E_2)m(f) \quad 2.4b$$

Solving these as before yields

$$m(b)' = m(b) + \frac{D(s, f)m(f)}{D(s, b)} \quad 2.5$$

so that the error in bone mineral,  $\Delta m(b)$ , is given by

$$\Delta m(b) = \frac{D(f,s)m(b)}{D(b,s)} \quad 2.6$$

If the fat were composed of a uniform layer this error could be removed by proper choice of baseline, in effect removing a background signal of bone due to fat. In practice a baseline measurement is made, so that the error which is unaccounted for is due to differences in the mass of fat between the baseline and the position of bone measurement,  $\Delta m(f)$ . The error is now described by the following expression

$$\Delta m(b) = \frac{D(f,s)\Delta m(f)}{D(b,s)} \quad 2.7$$

The fractional error in bone mass is given by

$$\frac{\Delta m(b)}{m(b)} = \frac{D(f,s)\Delta m(f)}{D(b,s)m(b)} \quad 2.8$$

An alternative expression can be derived using the fractional fat content rather than the mass of fat. The fractional fat content is defined as the ratio of fat volume to total soft tissue volume and refers to the cylinder of tissue interrogated by the photon beam. A mineral thickness,  $t$ , is equivalent to the bone mass,  $m(b)$ , divided by the bone mineral density. If  $\Delta f$  is the difference between fractional fat content at the baseline and at the vertebrae, and the patient has thickness  $d$ , the equivalent thickness of fat,  $\Delta f(d-t)$ , is given by the difference of fat mass,  $\Delta m_f$ , divided by the fat density. These equivalent thicknesses can

be substituted into equation 2.8 to yield the expression

$$\frac{\Delta m(b)}{m(b)} = \frac{(d-t)D'(f,s)\Delta f}{t D'(b,s)} \quad 2.9$$

where  $D'(a,b)$  is similar to  $D(a,b)$ , but depends on linear attenuation coefficients rather than mass attenuation coefficients.

Examination of equation 2.9 reveals two terms which describe the patient,  $(d-t)/t$  and  $\Delta f$ , and another term which is independent of the patient,  $D'(f,s)/D'(b,s)$ , a fat effect parameter. Calculation of expected errors in bone measurements will require an estimate of the patient parameters as well as the patient independent parameter which will depend upon the values chosen for the linear attenuation coefficients.

Linear attenuation coefficients for tissues will depend upon the atomic composition of the tissues and are not a trivial exercise to obtain. Webber (1987) has compiled a list of measured as well as derived attenuation coefficients for lean tissue, fat tissue and bone. In addition recommended linear attenuation coefficients are given for use in the energy range 40 kev to 100 kev.

Using these coefficients the quantity  $D'(f,s)/D'(b,s)$  was calculated and the results are given in table 2.1. Clearly, the choice of value of linear attenuation coefficient is critical, with fourfold

Table 2.1 The value of the fat effect parameter by source of linear attenuation coefficients.

<u>Reference</u>	<u>Fat Effect Parameter</u>
Bradley, Chong and Ghose (1986)	-0.0686
Hubbell (1982)	-0.0378
Joyet, Baudraz and Joyet (1974)	-0.0834
Webber (1987)	-0.0535
White and Fitzgerald (1977)	-0.0225

differences possible in the calculation of bone mass errors.

For further calculations using the model of equation 2.9 the recommended coefficients were used to give a value for  $D'(f,s)/D'(b,s)$  of  $-.0535$  for  $^{153}\text{Gd}$ . A similar approach using the recommended attenuation coefficients at 60 keV, and the mean of the coefficients of Rao (1975), Hubbell (1982) and White (1980) gives a value for  $D'(f,s)/D'(b,s)$  for  $^{241}\text{Am}$ - $^{137}\text{Cs}$  of  $-0.0404$ . These values will be used to determine the errors due to measured fat distributions in later sections.

### 2.3 Phantom Measurements

The adequacy of the model as expressed in equation 2.9 was tested by simulating inhomogeneous fat distributions using phantom materials. The DPA measurements were made using a source of  $^{153}\text{Sm}$  (which has the same photon energies as  $^{153}\text{Gd}$  with the same decay daughter  $^{153}\text{Eu}$ ) developed by Bhaskar (1984). This source was mounted on a modified rectilinear scanner which was interfaced to a NOVA computer and transmission measurements were made using a method described in detail by Rowntree (1985). The analysis of the transmission data differed in that images of the DPA scans were generated. Figure 2.1 shows a typical noisy image; the rectangular aluminum region has approximate dimensions of 5 by 10 pixels.

The three tissues lean, fat and bone were

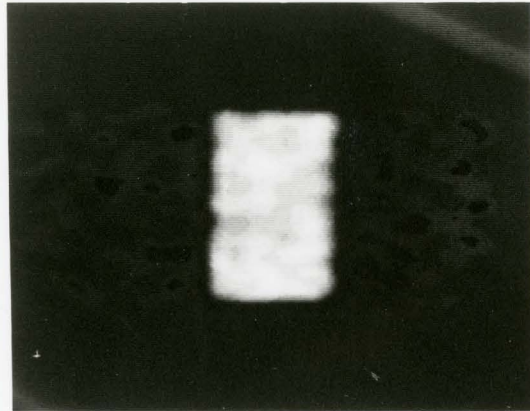


FIGURE 2.1 Dual photon bone mineral image obtained using the modified rectilinear scanner.

substituted with water, polyethylene and aluminum respectively. Because the linear attenuation coefficients for the phantom materials do not exactly match their biological counterparts, the quantity  $D'(f,s)/D'(b,s)$ , the fat effect coefficient, for the phantom materials and for  $^{153}\text{Sm}$  was determined to be  $-0.0459$ .

The fractional error in aluminum thickness was determined for various combinations of thicknesses of phantom materials with 20 cm total thickness by Rowntree (1985) and selected measurements were repeated using the image display analysis to verify the results. The combined sets of data were analyzed by plotting the fractional error against the absolute value of  $\Delta f(d-t)/t$  in figure 2.2. A straight line was obtained with correlation coefficient of 0.98. The slope which should be equal to the fat effect coefficient was  $0.046 \pm 0.006$ . It appears that the analytical model adequately describes the effect of inhomogeneous fat distributions and can be used for further estimates of the error.

#### 2.4 In vivo fat distribution - single slice

Of the two patient dependent parameters in equation 2.9, the first,  $(d-t)/t$ , which describes patient thickness divided by equivalent bone mineral thickness is fairly well defined, whereas the second,  $\Delta f$ , the fat deviation is not. In order to estimate the fat deviation for the population

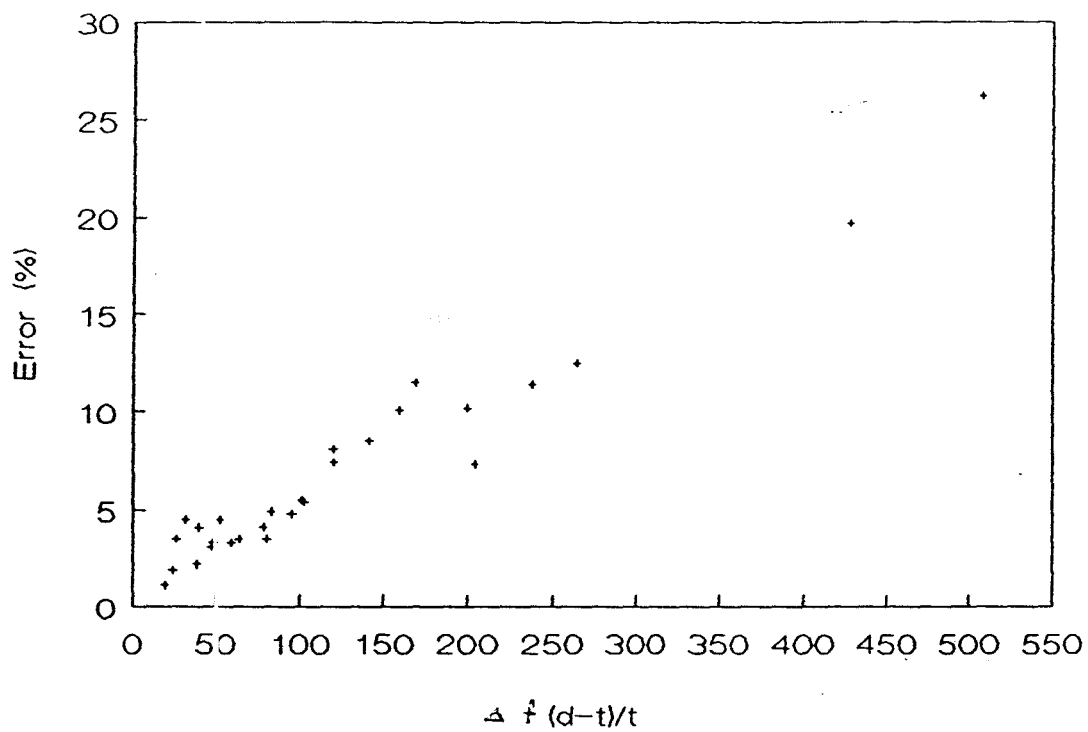


FIGURE 2.2 Plot of bone mineral error against  $\Delta f(d-t)/t$ .  
This should be a straight line with slope  
equal to the fat effect parameter.

seen clinically, CT images centred through a single lumbar vertebral body were obtained and analyzed. These were taken from archived images of a series of 11 patients who were to be scanned for other causes and volunteered for a single additional exposure.

A rectangular region of interest corresponding to the typical field of view for a DPA scan was manually drawn using a joystick and a histogram of CT numbers was created as shown in figure 2.3a. When the region was positioned in soft tissue there were two distinct populations of CT numbers corresponding to lean and fat tissue as in figure 2.3b, whereas when the region was drawn to include the vertebrae a third population of CT numbers appeared which corresponds to bone as in figure 2.3c.

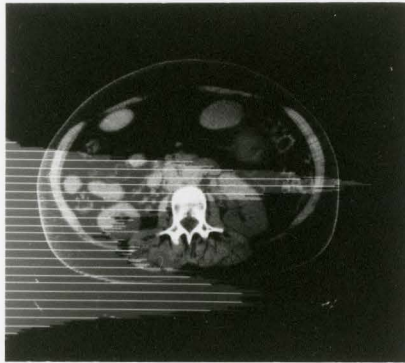
The fractional fat content for a given region of interest was defined as the volume of fat divided by the volume of both fat and lean tissue. This was calculated from the histogram by using the following expression

$$\text{fat content} = \frac{\# \text{ pixels fat}}{\# \text{ pixels fat} + \# \text{ pixels lean}} \quad 2.10$$

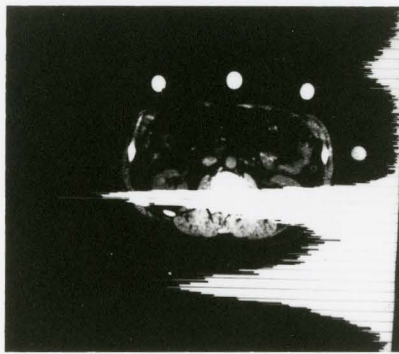
The numbers of pixels were obtained by setting a FWHM window to include either the fat or lean peaks shown in figure 2.3 and determining the area of the peak. The fat content was measured at seven different positions, both over the vertebrae and lateral to it as indicated in figure 2.4.



(a)



(b)



(c)

FIGURE 2.3 CT transverse images through a lumbar vertebra showing the shape of the region of interest (a) and the histograms of CT numbers for regions adjacent to the vertebra (b) and including the vertebra (c). The lean, fat and bone pixels appear as distinct peaks in the histograms.

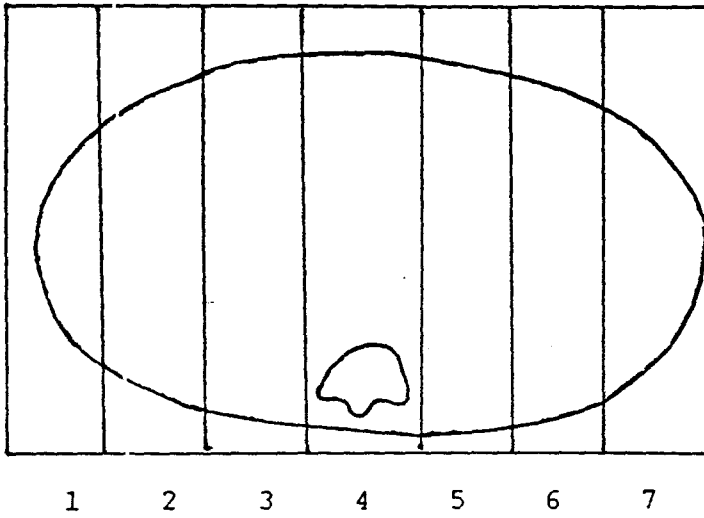


FIGURE 2.4 Location of measurement regions on CT image.

Each region of interest was of a similar size and shape within the reproducibility of a manual drawing procedure.

The fat content deviation was defined as the difference between the fat content at a given location and the fat content at the spine expressed as a percentage. This was calculated for each region and the results are plotted by region in figure 2.5. The fat content deviation increases as the position of the region of interest is moved away from the vertebrae, probably due to reaching the side of the patient with increasing subcutaneous fat.

For this reason a mean fat content deviation was calculated, which is the mean of the deviations for the two regions immediately adjacent to the vertebrae, on either side. In addition, this was expected to mimic the clinical situation most closely, namely that the baseline would include regions on either side of the vertebrae. The mean fat content deviation will be referred to as the fat deviation for the individual scan for the remainder of this discussion.

The fat deviations were found to be both positive and negative depending upon the patient, and there was no significant correlation with either fat content at the vertebrae or with patient age. The magnitude of the fat deviation was not strongly dependent on other patient parameters, and it is unlikely that either age or fat

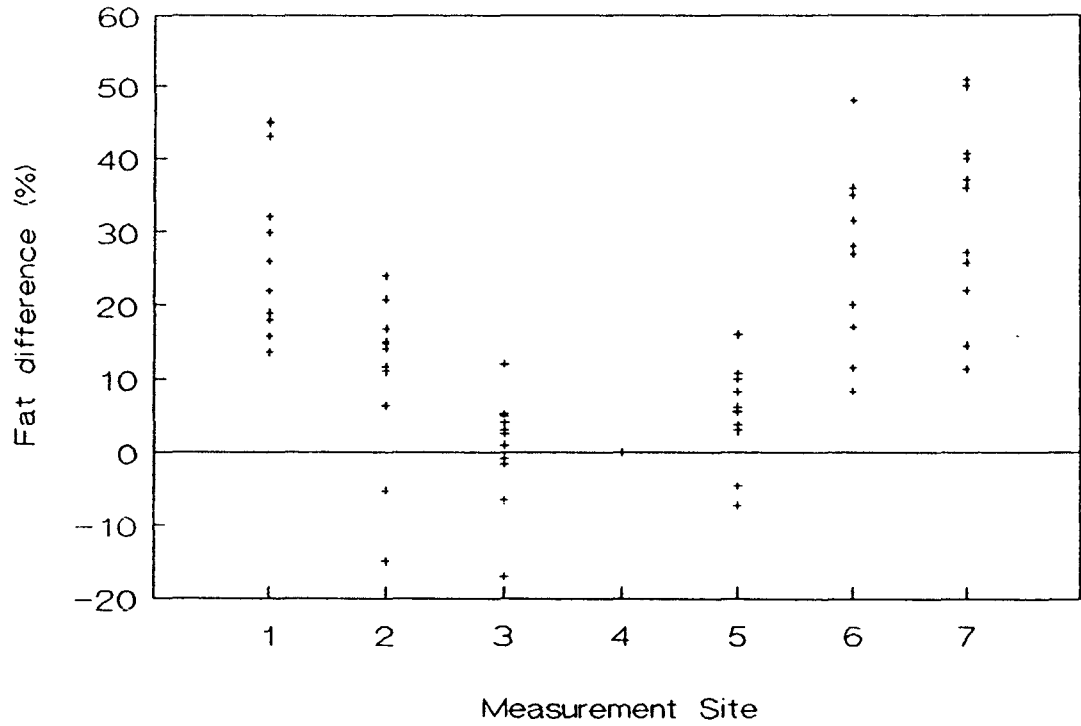


FIGURE 2.5 Fat deviation for 11 single scan measurements at each region.

content is a good predictor of deviation.

The magnitude of fat deviation was found to have a median value of 4.1% with upper and lower quartiles of 7.5% and 3.0% respectively. Fat deviation measurements were repeatable to within 0.8%.

### 2.5 In vivo fat distribution - multiple images

The single scan measurements were made with the assumption that the fat deviation did not vary along the cephalad-caudal axis and that a single measurement is representative of the entire lumbar region. In order to test this, the fat deviation was measured through each of four lumbar vertebrae for 15 volunteers. The fat deviations for the individual vertebrae were determined, and there was little dependence on vertebral body number. In figure 2.6 the individual fat deviation measurements can be seen to cluster about the mean value with little divergence from the mean value. This suggests that there is not enough variation from vertebra to vertebra to be of consequence.

For the multiple scan measurements, as for single image measurements, the fat deviation could be both positive and negative, and there was no strong correlation with age or fat at the spine. The mean fat deviation was found to have a median value of 4.1% with upper and lower quartiles of 12.0% and 1.7% respectively. The mean fat deviation was found with precision of 0.7%.

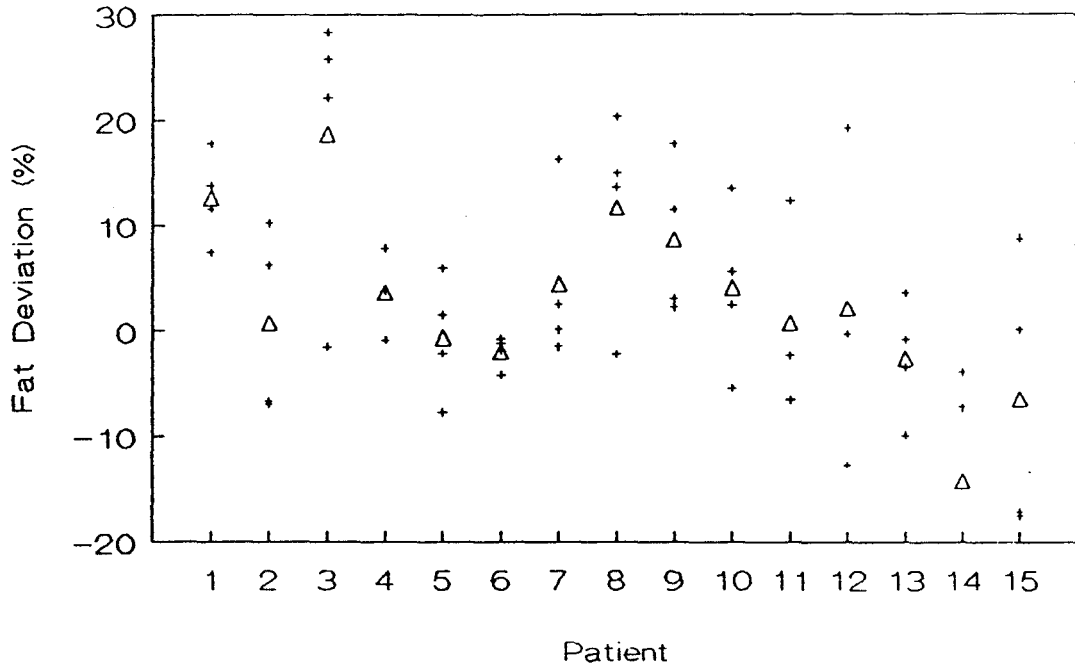


FIGURE 2.6 Fat deviation for 15 multiple scan patients including individual measurements (+) and mean measurements (Δ).

Since the differences in fat content are assumed to be due to deep fat surrounding organs which are large relative to the slice thickness it seems reasonable to assume that the single measurement through the centre of one vertebra is representative of the fat deviation over all four vertebrae. The clustering of the multiple measurements, and the close relationship between the single and multiple measurements suggests that both the single measurements and the multiple measurements represent mean fat deviations which can be expected in the general population. For these reasons the individual results of the first group of images were combined with the mean results of the second group of images to yield fat deviation measurements for 26 patients.

The fat deviations for the combined group are plotted against age in figure 2.7 and against fat at the spine in figure 2.8. The correlation coefficient was calculated for the relationships of fat deviation to age and fat deviation to fat at the spine, and for both was found to be 0.34. This is not significantly different from 0 which suggests that there is no strong correlation between the fat deviation and patient age or fat at the spine.

The magnitude of the fat deviation for the combined populations had a median of 4.4% with upper and lower quartiles of 8.2% and 2.1%. The maximum for an individual was 19.0%.

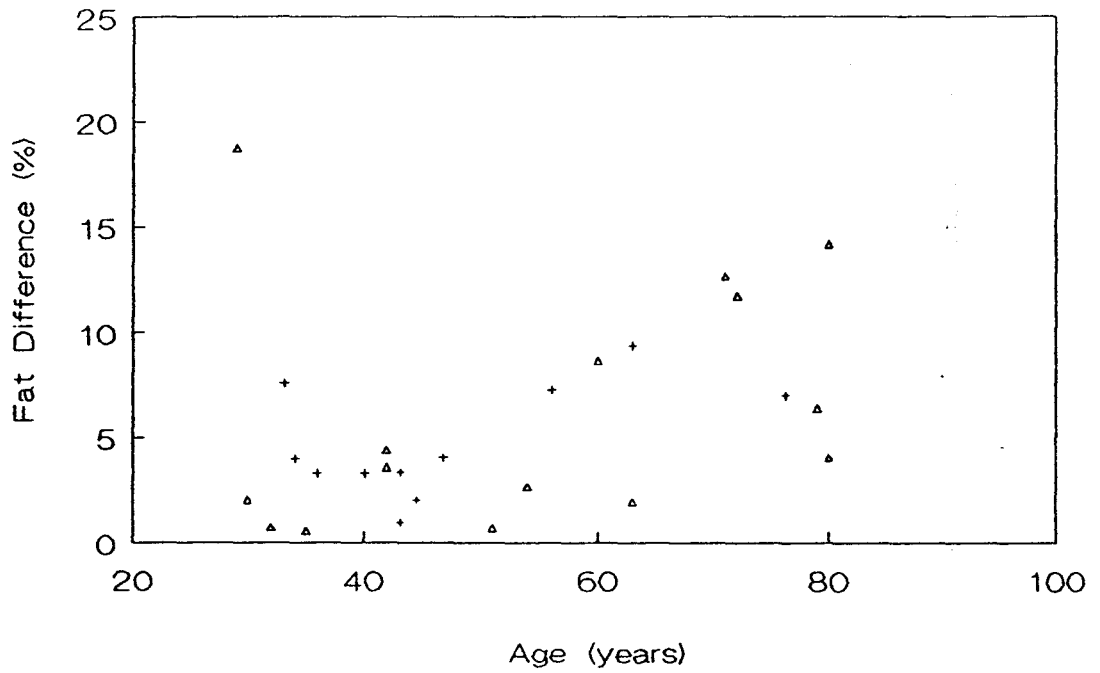


FIGURE 2.7 Fat deviation as a function of age obtained from single (+) or multiple (Δ) measurements.

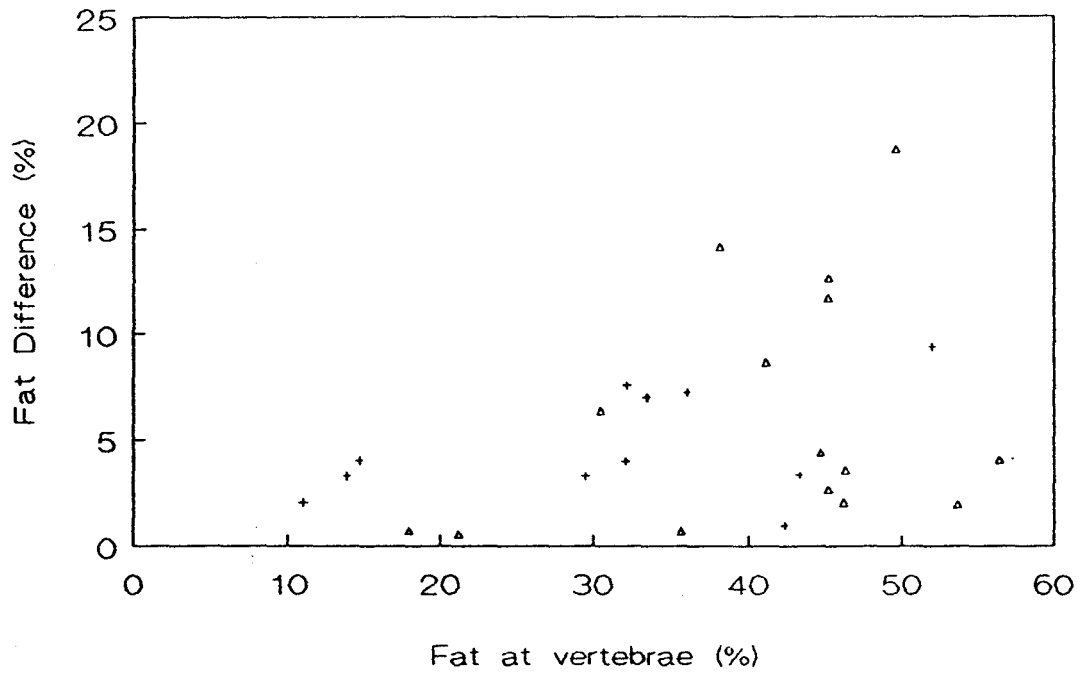


FIGURE 2.8 Fat deviation as a function of fat fraction at the spine including single measurements (+) and multiple ( $\Delta$ ) measurements.

## 2.6 The effect of fat on DPA accuracy

The effect of fat deviations which were measured can be estimated by substitution of typical patient parameters into equation 2.9. This was performed for a 20 cm thick patient for the median, and upper and lower quartiles, with the results plotted in figure 2.9. The typical population seen at McMaster has bone mineral densities (BMD) ranging from 0.8 g/cm<sup>2</sup> to 1.4 g/cm<sup>2</sup> (Webber 1988). Using the median fat deviation of 4.4% suggests that BMD errors of 6 to 11% will be common. Using the upper quartile fat deviation of 8.2%, BMD errors of 11 to 20% are possible. Substitution of the mean BMD value of 1.1 g/cm<sup>2</sup> along with the median fat deviation value yields a median BMD error of 7.9%.

This median error can be compared with the results of Roos et al (1980). Using 241-Am-137-Cs they found median errors of 10%. Using equation 2.9, their error will correspond to a median error of 12% using 153-Gd.

An alternative analysis is to choose an arbitrary BMD error, say 10%, and to determine the fraction of the population which can be expected to have errors of greater magnitude. Choosing a mean BMD value of 1.1 g/cm<sup>2</sup> and a 20 cm thick patient, all patients with fat deviations greater than 5.6% will have BMD errors greater than 10%. Examination of figure 2.9 reveals 10 out of 26 patients with fat deviations greater than 5.6%. In other words about 1/3 of

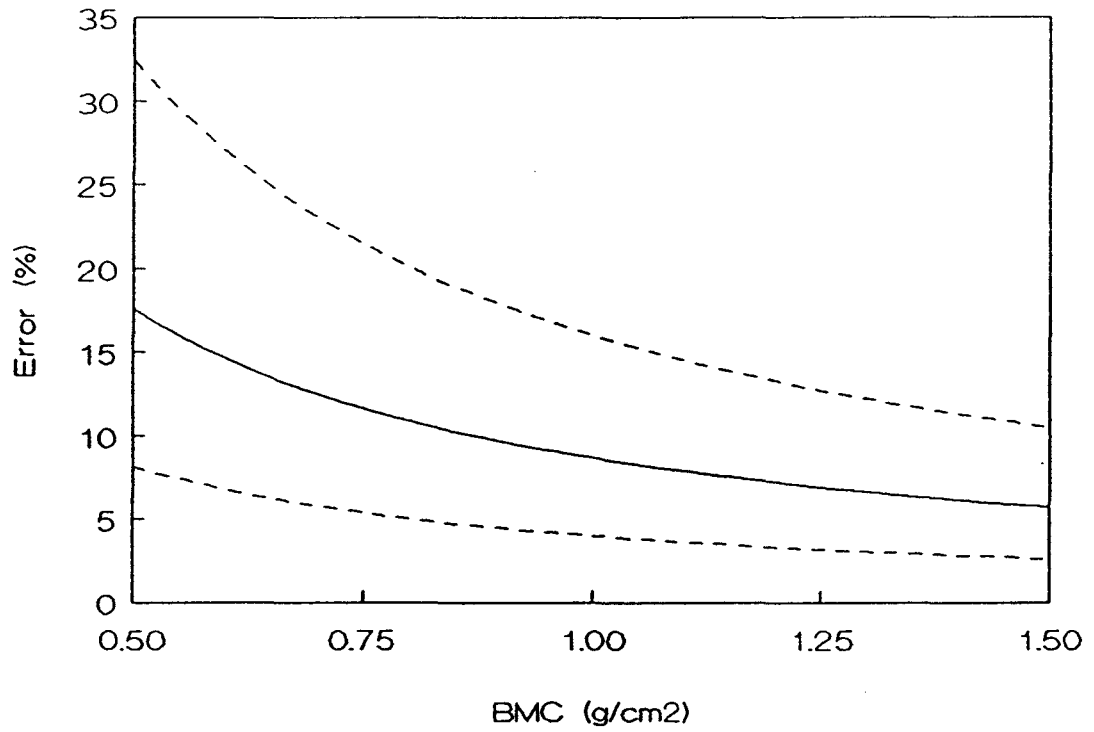


FIGURE 2.9 Projected error in the measurement of bone mineral as a function of bone mineral density. Errors are given for median fat deviations (solid line) as well as for upper and lower quartiles.

the patients will have BMD errors greater than 10%.

It would appear that median fat differences can give rise to BMD errors of the order of 8%. This effect must contribute to the biological variation of DPA measurements. Of more concern, however, is the fact that 1/3 of the population can be expected to have BMD errors in excess of 10% with some errors considerably greater. This is compounded by the fact that the errors increase as the BMD decreases and that the errors cause predominately falsely high BMD measurements. The unfortunate result is that the measurements of most concern are most subject to inaccuracies.

## CHAPTER 3

### FEASIBILITY OF TPA AT THE LUMBAR SPINE

The results of the previous chapter suggest that inhomogeneous distributions of fat at the lumbar spine can introduce errors of greater than 10% in a significant fraction of the patient population, which is in agreement with previous studies (Krolner and Nielsen, 1980, Roos, Hansson and Skoldborn, 1980). The errors are an unavoidable consequence of the DPA technique in which the body is assumed to be composed of two components, mineral and soft tissue. Unfortunately, a third component, fat, is interpreted erroneously as mineral mass.

If the effect of fat could be removed then it might improve the discrimination between normal and osteoporotic populations. An approach might be triple photon absorptiometry (TPA) in which three photon energies are used in a three component body. In this chapter certain theoretical aspects of TPA will be presented with an examination of the variance and accuracy which may be expected. A comparison of the possible merits of TPA compared with DPA will be given.

#### 3.1 Variance of TPA Measurements

The theory of triple photon absorptiometry has been

described in detail in chapter 1, in which the equivalent thickness of a given basis phase is recovered using the attenuation factors (given by equation 1.3) for the three photon energies and the inverse of the linear attenuation coefficient matrix as in equation 1.5, reproduced here as equation 3.1.

$$\tilde{t} = \tilde{\mu}^{-1} \tilde{Y} \quad 3.1$$

with 
$$Y(E) = \ln(I_0/I) = \sum(\mu(E, \phi)t(\phi)) \quad 3.2$$

It was indicated that two basis phases are sufficient to describe the attenuation of diagnostic energy photons to small fractions accurately, so that triple photon absorptiometry will require measuring small differences in attenuation coefficients of the phases. Since the ultimate aim of TPA is to generate bone mineral measurements with good precision, the test of the feasibility of TPA will be the precision of such measurements at reasonable radiation doses.

A fundamental factor which introduces variance into the TPA measurement and will prove to be a limiting factor in the precision of the technique is quantum noise from counting statistics of the transmitted photons. Efforts to choose the photon energies should be directed towards maximizing the statistical precision. The statistical precision for various isotope combinations and patient

geometries has been calculated for DPA using a generalized parameter which was independent of source intensity (Watt 1975, Smith, Sutton and Tothill 1983). A similar treatment can be performed to determine the optimum energies for TPA.

The variance of the bone mineral measurement is a complicated function of the patient geometry, the photon energies and the initial intensities of the three photon beams. However if the patient parameters and the initial photon intensities are held fixed, an expression for the variance can be derived using the standard propagation of errors as described in such sources as Bevington (1969).

If one begins with equation 3.1, the variance is given by the following expression

$$\text{var}(t(b)) = \text{var}\left(\sum \mu^{-1}(b,E)Y(E)\right) \quad 3.3$$

in which  $\mu^{-1}(b,E)$  is an element of the inverse of the matrix  $\mu$ . In practice, the elements of  $\mu^{-1}$  will be obtained directly using phantoms rather than by inverting the matrix  $\mu$ , and errors in the measurement of  $\mu^{-1}$  will result in errors of accuracy rather than loss of precision. For the purpose of this discussion the variance will be considered to be due entirely to counting statistics, and  $\mu^{-1}(b,E)$  can be regarded as a constant. In this case the variance can be written as

$$\text{var}(t(b)) = \sum (\mu^{-1}(b,E))^2 \text{var}(Y(E)) \quad 3.4$$

initial intensities. A normalized variance,  $V$ , which is independent of the initial intensity, is given by multiplication of the variance of the bone mineral by the normalized initial intensity as in equation 3.9.

$$V = \sum [(\mu(b,E))^{-1} e^{2Y(E)} / f(E)] \quad 3.9$$

Typical forms for the factor,  $f(E)$ , are given in equation 3.10.

$$\text{equal initial intensity} \quad f(E) = 1 \quad 3.10a$$

$$\text{equal transmitted intensity} \quad f(E) = e^{Y(E)} \quad 3.10b$$

$$\text{equal dose} \quad f(E) = \frac{1}{(1 - e^{-Y(E)})} \quad 3.10c$$

If the effect of crossover is included, then the normalized variance will change since the value of  $I(E)$  in equation 3.5 will be falsely increased by crossover. If  $I(E)$  represents the transmitted intensity at energy  $E$ , then  $I(E)$  is given by

$$I(E) = I_m(E) - \sum X(E') I(E') \quad 3.11$$

for  $E' > E$

where  $I_m(E)$  represents the measured intensity at energy  $E$  and  $X(E')$  is the crossover from energy  $E'$  to energy  $E$ . Since the variance of  $I_m(E)$  obeys counting statistics, the variance of  $\ln(I(E))$  is given by

$$\text{var}\{\ln[I(E)]\} = [I_m(E) + \sum X(E') I(E')]^2 / I(E)^2 \quad 3.12$$

This can be written as the multiple of  $1/I(E)$  and a crossover term,  $XF(E)$  given by

$$XF(E) = \{Im(E) + \sum (X(E')^2 I(E'))\} / I(E) \quad 3.13$$

Substitution for  $I(E)$  from equation 3.2 and  $Im(E)$  from equation 3.11 gives

$$XF(E) = 1 + \sum \{ [X(E') + X(E')]^2 / f(E') e^{-Y(E')} \} / f(E) e^{-Y(E)} \quad 3.14$$

and the normalized variance,  $V$ , can be written as

$$V = \sum \{ (\mu^{-1}(b,E)) e^{-2Y(E)} [XF(E)/f(E)] \} \quad 3.15$$

This is similar to equation 3.10, with the additional term  $XF(E)$  accounting for crossover.

### 3.2 Selection of photon energies

Once the normalizing correction,  $f(E)$ , and the patient parameters are chosen, the normalized variance can be calculated for any given set of photon energies. In principle the optimum photon energies will be given by the minimum value of the normalized variance over the three space of photon energies. In practice the minimum is difficult to find since the normalized variance diverges when two or more energies are identical. The possible choices of photon energies are reduced further by the practical consideration of the photon energies of available isotopes.

In order to overcome these difficulties it was assumed

that one of the photons would have energy greater than 100 keV so that the dominant photon interaction for all tissues would be Compton scattering. The normalized variance was calculated over the plane of the remaining two photon energies in order to find the minimum. The patient parameters were set to correspond to those typical at McMaster, viz 20 cm total thickness, 30% fat content in soft tissue and  $1.0 \text{ g/cm}^2$  bone mineral areal density. Linear attenuation coefficients were obtained from a parameterization of White and Fitzgerald (1977).

Results for some selected combinations of energy are shown in figure 3.1 with  $f(E)$  set to unity for all photon energies. Two of the energies have been fixed and the value of the normalized variance is plotted for the third energy ranging from 20 to 100 keV. Three different sets of photon combinations are given, with the fixed photon energies at 42 and 103 keV, 60 and 660 keV, and 37 and 145 keV corresponding to  $^{153}\text{Gd}$ ,  $^{137}\text{Cs}$ - $^{241}\text{Am}$  and  $^{141}\text{Ce}$  respectively. The minima at approximately 28 keV and 60 keV for the Cs-Am and Ce curves correspond to the ideal third energy for these isotopes.

Similar data are presented in figure 3.2 with two energies fixed at 103 and 42 keV and the factor  $f(E)$  chosen to correspond to the three different conditions in equation 3.10. Qualitatively the shapes of the curves are similar,

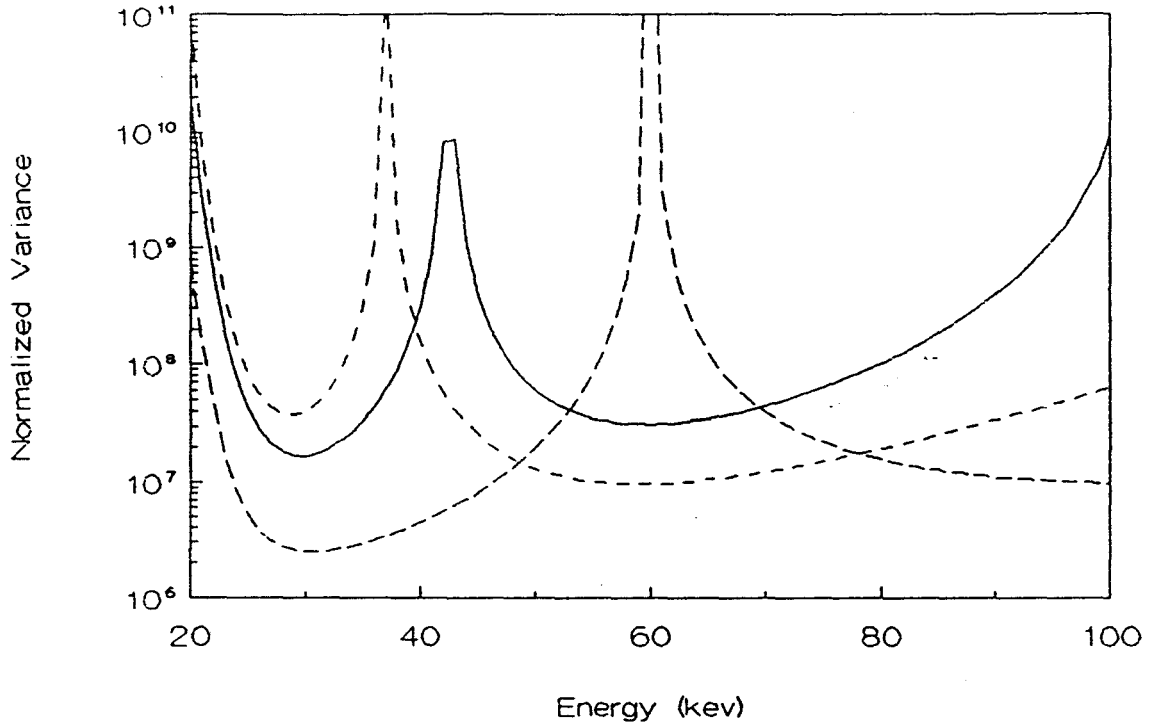


FIGURE 3.1 Normalized variance as a function of one photon energy for different combinations of the other two energies: 103 and 42 keV (—), 145 and 37 keV (---) and 660 and 60 keV (- - - -).

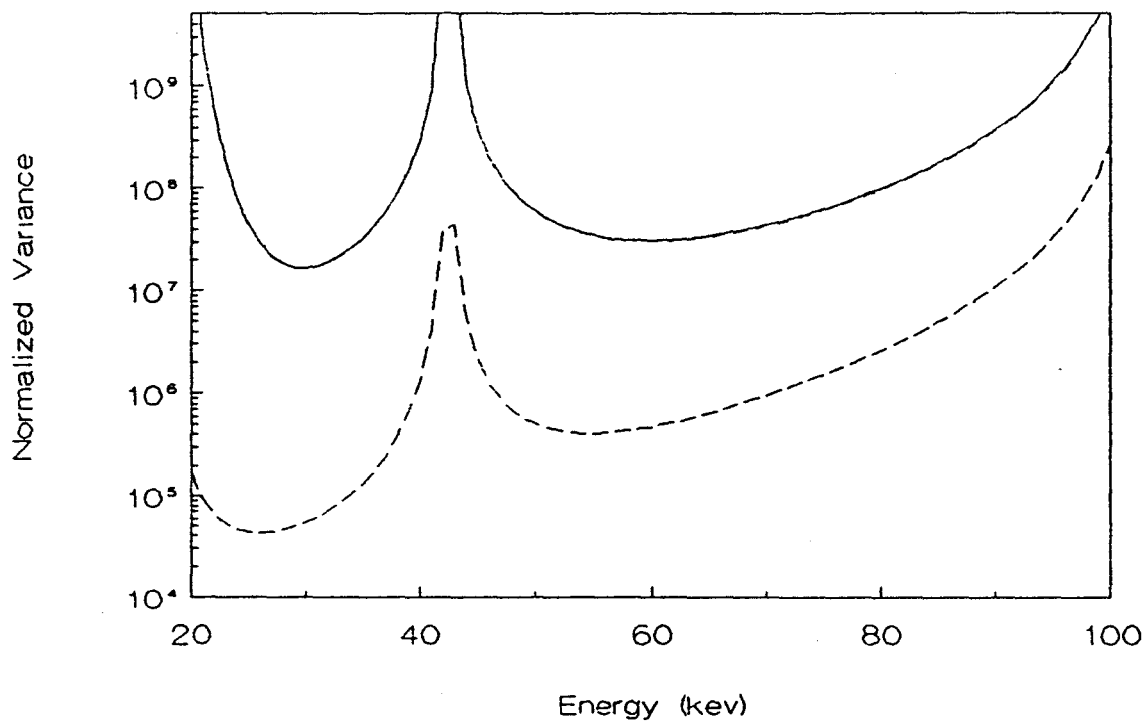


FIGURE 3.2 Normalized variance as a function of one photon energy with the others fixed at 103 and 42 keV. The different curves are for different forms of the factor  $f(E)$ : equal transmitted intensity (—) indistinguishable from equal initial intensity (- - -) and equal dose (- · - ·).

with little change in the location of the minima due to the choice of the form of  $f(E)$ .

Similar data are presented in figure 3.3 with two energies fixed at 103 and 42 keV and the crossover factor ranging from 0 to 10%. Again, the shapes of the curves are qualitatively similar, with little change in the location of the minima due to crossover. The effect of crossover is more pronounced for lower energies which suggests that the optimal combination of energies will not include very low energies. Using these results the combination of 145, 60 and 37 keV using the isotopes  $^{141}\text{Ce}$  and  $^{241}\text{Am}$  was chosen for further analysis of TPA.

### 3.3 Simulation of TPA

The variance of the bone measurement was estimated by computer modelling of the TPA process. Transmission of each photon beam was simulated for a bone mineral equivalent elliptical cross-section cylinder embedded in composite fat and lean tissue. The typical patient parameters referred to earlier were used to determine the attenuation factors,  $Y(E)$ , using the model indicated in figure 3.4.

An initial intensity was chosen which was then used to generate the transmitted intensity for each energy. Statistical fluctuations were introduced using a random Gaussian variate. These were generated using an algorithm given by Lewis (1975) in which random points on the unit

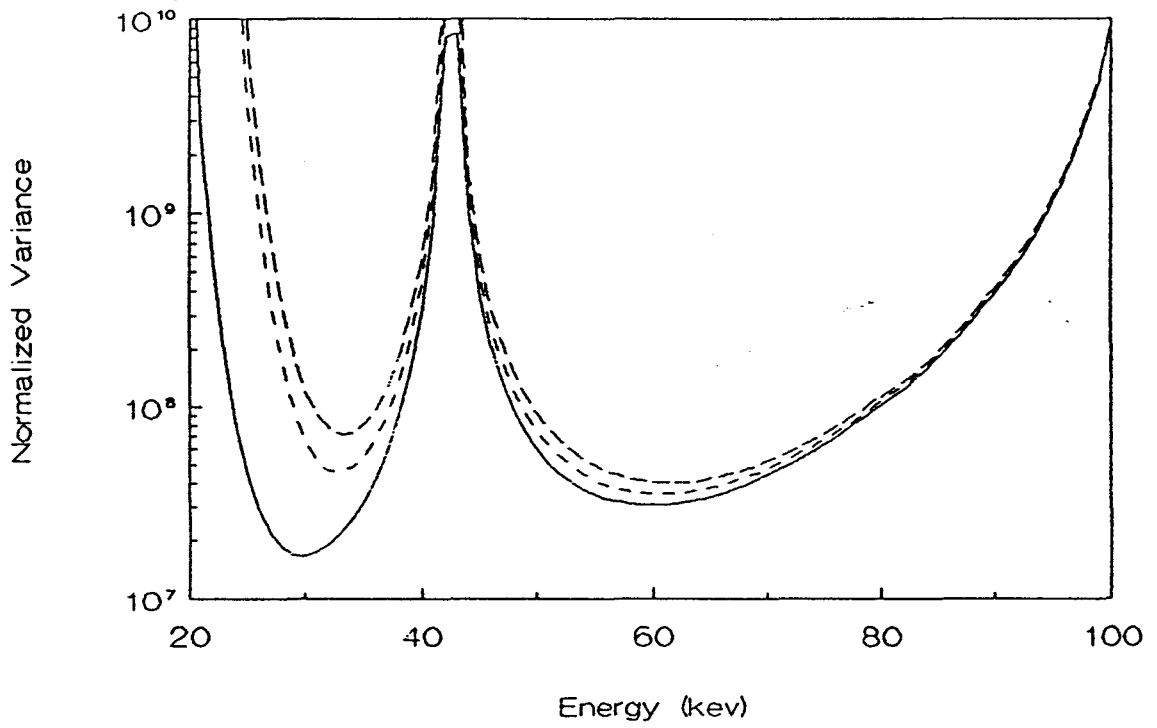


FIGURE 3.3 Normalized variance as a function of one photon energy with the others fixed at 103 and 42 kev. The different curves are for 0% crossover (—), 5% crossover (- - - -) and 10% crossover (- · - · -).

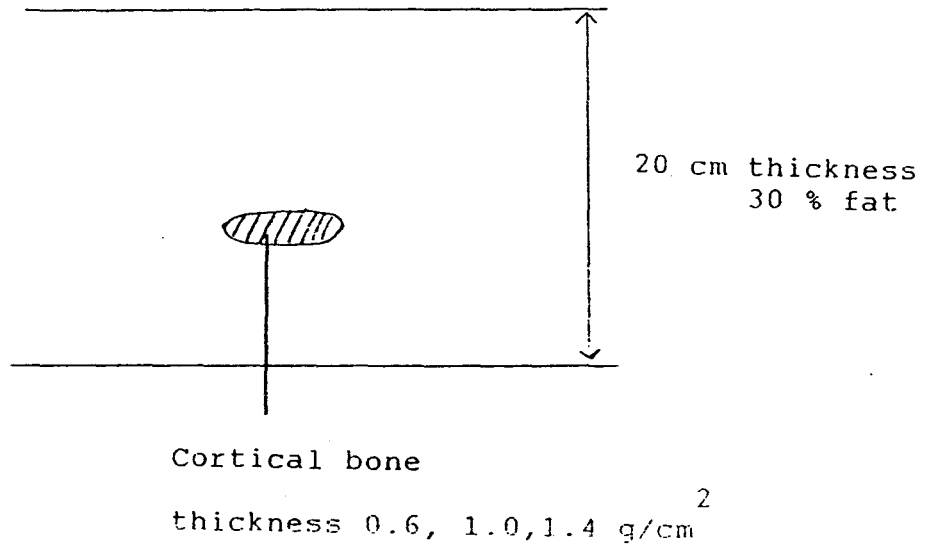


FIGURE 3.4 Model used for simulation of TPA at the spine.

circle are chosen. The unit circle is then inverted to give two gaussian variates with mean 0 and standard deviation 1 as illustrated in figure 3.5.

Inverse linear attenuation coefficients appropriate for the selected photon energies were used to recover the equivalent bone mineral thickness and to generate the simulated TPA images shown in figure 3.6.

The local variance of the bone mineral equivalent thickness was estimated by the root mean squared difference from the expected bone mineral value. The noise amplitude was found for different combinations of crossover and photon intensity, defined as the number of transmitted photons at 145 keV in a region with no bone mineral and is plotted in figure 3.7. The noise amplitude was found to vary as  $\sim 1241(1+0.055 X_0)/\sqrt{N}$  g/cm<sup>2</sup>, where  $X_0$  is the crossover in percent and  $N$  is the number of photons in the 145 keV channel. This expression is valid both for a single pixel as well as for an entire vertebra, and is in agreement with the theoretically derived variance. va

#### 3.4 The effect of uncertainty in attenuation coefficients

The uncertainty in the theoretical variance was determined by Monte Carlo methods. The parametrization of White and Fitzgerald was accurate to within 1%, which could include random deviations as well as deviations correlated with tissue type. Gaussian deviations with a standard

Figure 3.5 Algorithm for generating Gaussian variates,  $g_1$  and  $g_2$ .

```
v1 ← 2*rnd-1
v2 ← 2*rnd-1
r ← v12 + v22
if r > 1 then choose new v1 and v2
f ← [-2 ln(r)/r]1/2
g1 ← f*v1
g2 ← f*v2
```



FIGURE 3.6 Simulated TPA images for elliptical cylinders of bone with thicknesses from left to right of 0.6, 1.0 and 1.4 g/cm<sup>3</sup>. The images from top to bottom are with no statistical noise, with transmitted count rates of 500, 5000 and 50,000 per pixel in the high energy channel.

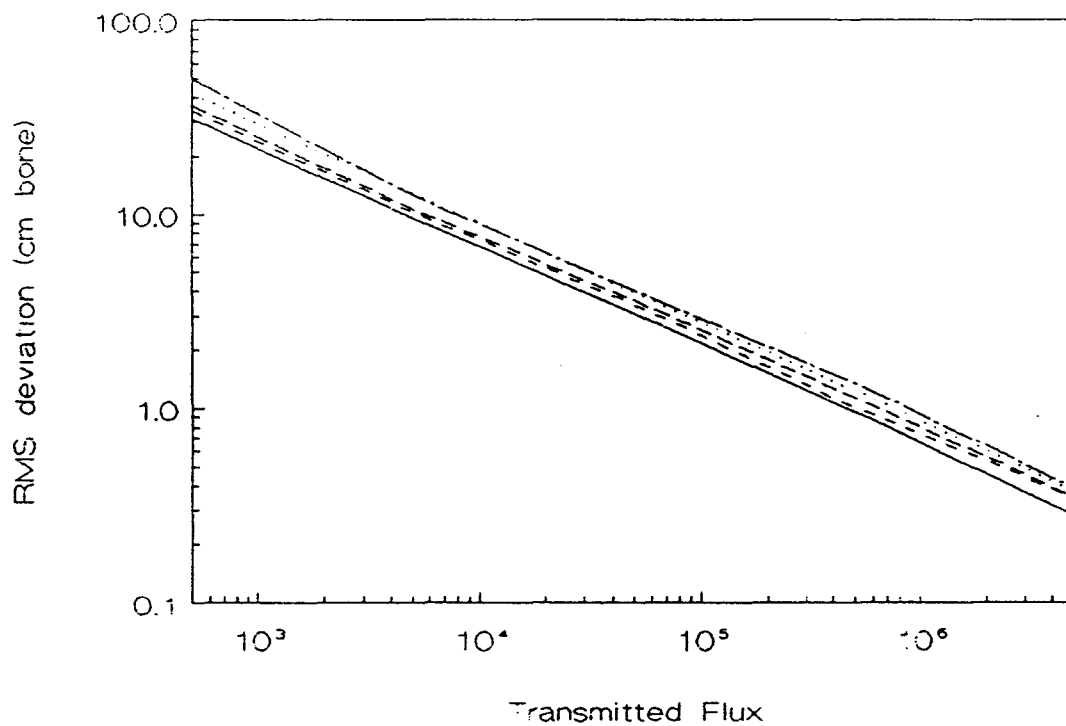


FIGURE 3.7 RMS deviation bone mineral content as a function of number of transmitted photons,  $N$ , and crossover. Proceeding from crossover of 0% (—) to 10% (— - —) in steps of 2.5%.

deviation totalling 1% both random and tissue correlated were added to the linear attenuation coefficient matrix and the variance was determined using equation 3.15. The resultant distributions were log-normal as indicated in figure 3.8. The greatest range in possible values of the variance occurs when the uncertainties are random. This should be expected, since random errors tend to remove the energy and atomic number dependence for the interaction cross-sections, thereby allowing for more phases than interaction types.

The most likely combination of uncertainties was chosen to be 25% random and 75% correlated. This gave distribution of variances with 90% confidence interval  $6.9 \times 10^4$  -  $9.7 \times 10^7$ , compared with the expected value of  $9.6 \times 10^6$ .

### 3.5 Count requirements and relative dose for TPA

The count requirements for TPA can be determined from the expression for the noise amplitude. The bone content must be determined only in the vertebrae, so the vertebrae must be defined for the measurement procedure. It is simplest to do this using the TPA image itself, but the vertebrae can be measured following definition by some other means (Jonson, Roos and Hansson 1986). In the former case, the probability that a true signal be detected above noise becomes greater than 50% when the signal to noise ratio,

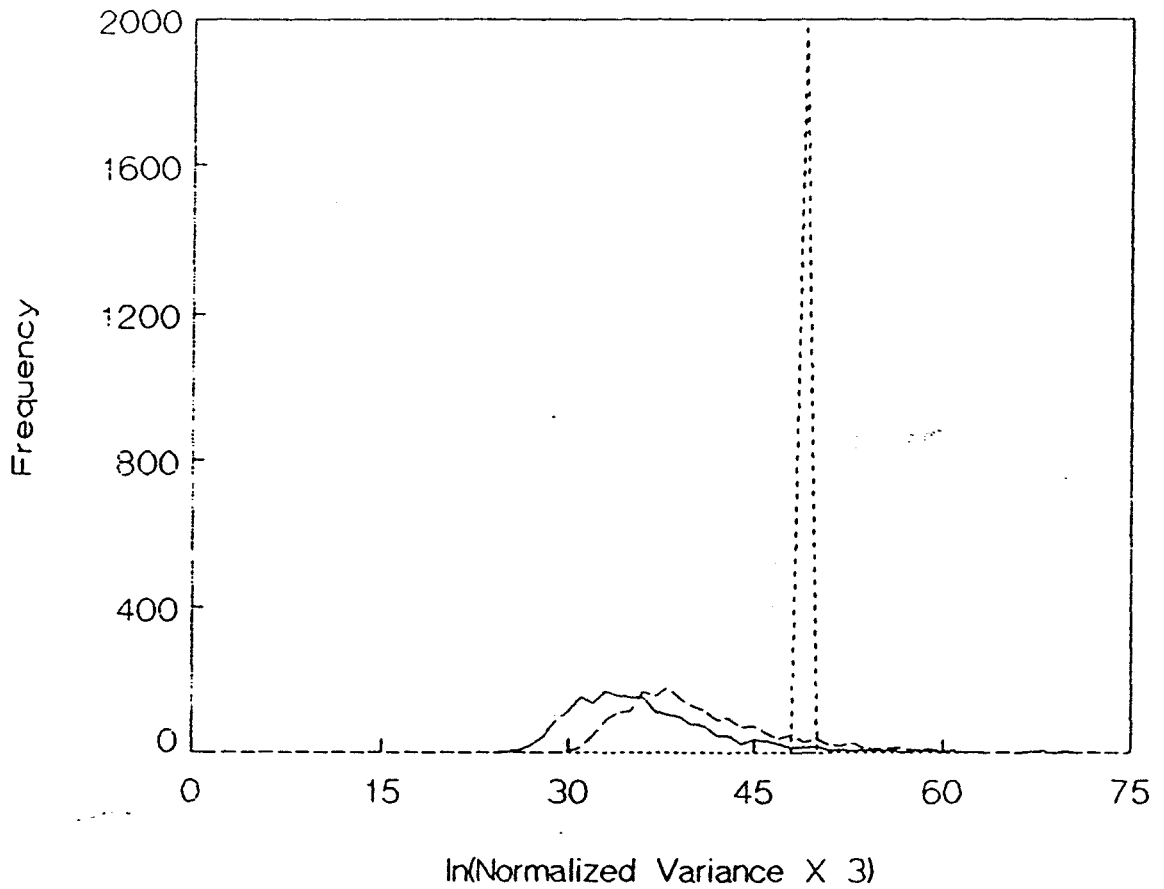


FIGURE 3.8 Frequency distribution of normalized variance generated by Monte Carlo simulation of effect of 1% uncertainty in linear attenuation coefficients with different fractions of correlation between the attenuation coefficients. The three curves represent 0 correlation (—) 50% correlation (— — —) and 100% correlation (- - - -).

SNR, is approximately 2 (Billingsley 1975). For bone mineral of  $1 \text{ g/cm}^2$  and crossover of 3% the number of transmitted photons per pixel must be 8,000,000, which is considerably larger than that encountered in typical DPA measurements. If the number of pixels in the vertebrae is  $\sim 400$  as for DPA, then the precision of the mean bone mineral measurement will be 2.5%.

The ratio of the skin doses for TPA and DPA was evaluated using

$$\frac{D(\text{TPA})}{D(\text{DPA})} = \frac{\sum \mu(E) E I_0(E)}{\sum \mu(E) E I_0(E)}, \quad 3.16$$

where  $\mu(E)$  represents mass energy absorption coefficients taken from Hubbel (1982),  $E$  represents the energy of the photons, and  $I_0(E)$  the incident intensity at that energy, and their product is summed over all photon energies. For TPA,  $I_0$  was determined from the transmitted countrate, while for DPA,  $I_0$  was determined from transmitted countrates seen at McMaster, typically 1500 per pixel. To obtain similar statistical precision the dose for TPA will be approximately 3,000 times the DPA dose. Although the form of equation 3.16 is a crude estimate of the dose, the ratio is so large that any refinements are unnecessary.

If the 90% confidence levels for the variance are used the dose ratio becomes 30 to 30,000 times that for DPA for 2.5% precision. In all likelihood one would like to achieve

precision of 1% or better, which requires a radiation dose at least 200 times that for DPA.

### 3.6 Feasibility of TPA at the Spine

Errors in transmission measurements arise from such factors as scatter, cross-over, beam hardening and statistical fluctuations. When the contribution from only the latter factor is analyzed for TPA using an optimum set of photon energies, the radiation dose associated with a reasonable point variance was found to be 3,000 times that for DPA. Clearly the other sources of error will exacerbate the situation.

These results support the conclusions of Hawkes, Jackson and Parker (1986) and Lehmann et al (1981) who showed that two phases are sufficient to describe the attenuation of tissue to within 1% over the diagnostic energy range. The high dose for TPA illustrates the difficulty of measuring the small attenuation differences between the three tissues. TPA is not a viable solution for this problem since the radiation dose for a reasonable variance is unacceptably large, with 90% confidence levels indicate dose levels 30 to 30,000 times those for DPA assuming a precision of 2.5%.

## CHAPTER 4

### TRIPLE PHOTON ABSORPTIOMETRY FOR THE HIP

In this chapter the problem of triple photon absorptiometry, TPA, for the measurement of bone mineral about a hip prosthesis is examined. The discussion begins with examination of the physical parameters of the problem, is followed by the development of the TPA source and ends with a description of phantom measurements. This will lead into examination of requirements for successful clinical TPA.

#### 4.1 Physical Parameters for TPA

The cause of mischief, and for our purposes, of interest, is the hip prosthesis itself. It is composed of the alloy Vitallium FHS which is specifically formulated for high tensile strength and biocompatibility. As indicated in table 4.1 the alloy is composed primarily of cobalt and has a mean atomic number of 26.3 (Howmedica 1979). The composition is very similar to that of stainless steel with cobalt substituted for iron. The density was determined volumetrically to be  $7.26 \text{ g/cm}^3 \pm 2\%$ .

The prosthesis is asymmetrically shaped (figure 4.1) for optimal load bearing characteristics and has a textured surface at the proximal end for improved adhesion to the

Table 4.1

Elemental composition of Vitallium FHS

<u>Element</u>	<u>Fraction(%)</u>	<u>Atomic Number</u>
Carbon	.05	6
Silicon	.75	14
Manganese	.70	25
Chromium	26.50	24
Molybdenum	5.50	42
Cobalt	66.50	27

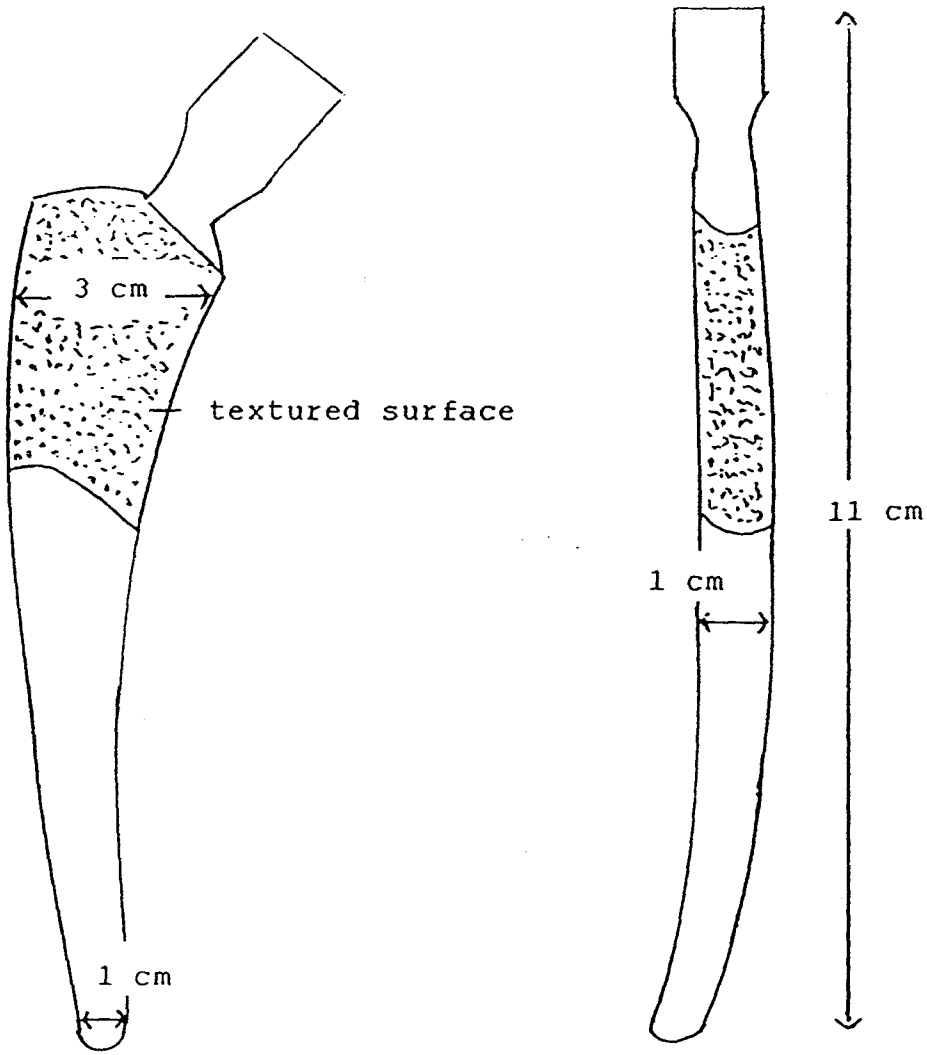


FIGURE 4.1 Hip prosthesis top view (left) and side view (right).

trabecular bone by ingrowth into the texture. The length from proximal to distal end is approximately 8 cm and the cross-section is approximately elliptical with thickness of 1 cm and width of 3 cm at the proximal end tapering to 1 cm at the distal end. The high attenuation of photons in the diagnostic energy range by Vitallium will make it advisable to measure transmission through the shortest pathlength. It may be possible to arrange for patients to lie so that typical transmission pathlengths are between 1 and 2 cms.

The prosthesis is situated in the femur, which has decreasing fractions of trabecular bone from the proximal end towards the centre, and it becomes trabecular again at the distal end. The bone mineral density at the hip will be in the range 0.6 to 1.0 g/cm<sup>3</sup>. The overlying soft tissue will have fat contents in the range 20 to 50% with total thickness in the range 10 to 20 cms, with typical thickness of 15 cm.

The attenuation characteristics of these materials are indicated in figure 4.2. The mass attenuation coefficients were determined using the following parameterization

$$\ln(\mu/p) = \sum_{i=0}^4 a(i)E^i \quad 4.1$$

The parameters,  $a(i)$ , for biological material were taken from White and Fitzgerald (1977) and for phantom materials

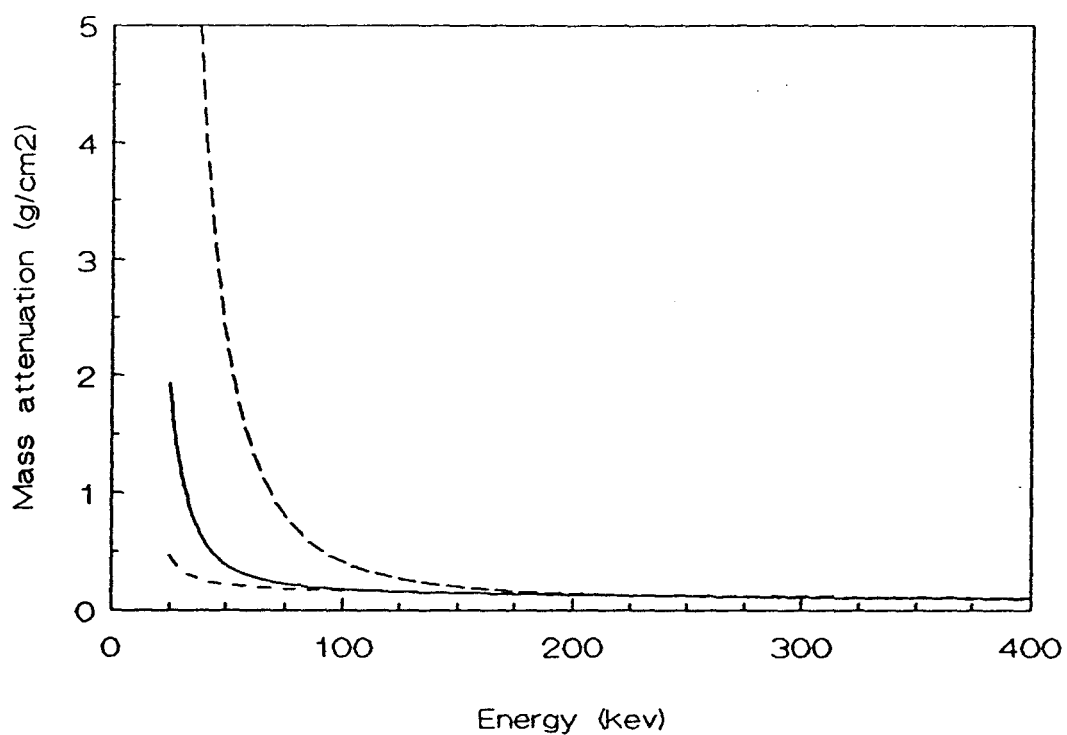


FIGURE 4.2 Mass attenuation coefficients for tissue and Vitallium. The solid curve is for cortical bone while the upper curve is for Vitallium and the lower curve is for muscle.

were obtained from fitting cross-sections from Hubbel et al (1975).

#### 4.2 Development of TPA source

The ideal source for TPA was determined by consideration of appropriate photon energies, half-lives and availability of isotopes. Examination of figure 4.2 reveals that the mass attenuation coefficient for Vitallium increases rapidly for energies below 100 keV whereas those for soft tissue and bone mineral only begin to diverge below 100 keV. The choice of the lowest energy was necessarily a compromise between these two considerations. The other two energies were separated from the lowest energy and each other in order to be resolved using NaI detectors for transmission measurements.

The isotopes  $^{141}\text{Ce}$  with a gamma energy of 145 keV and  $^{203}\text{Hg}$  with gamma energy of 279 keV and Tl x-rays in the range 72 to 80 keV were chosen as a possible TPA source. These feature half lives of 32.5 days for  $^{141}\text{Ce}$  and 46.9 days for  $^{203}\text{Hg}$  which would give the source a moderately useful life. They can be produced readily by neutron activation with thermal cross-sections of 0.6 barns for  $^{140}\text{Ce}$  and 4 barns for  $^{202}\text{Hg}$  (Lederer 1968).

The possibility of producing these sources using naturally occurring elements rather than enriched isotopes was determined by irradiating small quantities of

material. Samples of 34 mg CeO and 7.7 mg HgO were placed in the high flux tube at McMaster Nuclear Reactor for 30 minutes and 210 minutes respectively and allowed to decay for 24 hours. The spectra were obtained using a high purity Germanium detector to identify contaminants and the isotopes which were identified are indicated in table 4.2. These are all produced from different isotopes of Hg and Ce and since all have half-lives shorter than that of  $^{203}\text{Hg}$  and  $^{141}\text{Ce}$  it was considered possible to produce essentially pure sources by allowing the contaminants to decay.

The irradiation and decay times needed to produce pure sources were determined by considering the various isotopes which are produced by neutron irradiation of natural elements. The activity of a given isotope following irradiation is given by

$$A = \frac{ab m N_A \sigma \phi (1 - e^{-\lambda t})}{MW} \quad 4.2$$

where  $ab$  is isotopic abundance,  $m$  is mass of the material,  $N_A$  is Avogadro's number,  $MW$  is molecular weight of the material,  $\sigma$  is the neutron cross-section,  $\phi$  is the neutron flux,  $\lambda$  is the decay constant and  $t$  is the irradiation time. The activities of the neutron activation products were calculated using data taken from Lederer (1968) and are indicated in table 4.3 for Hg and table 4.4 for Ce in which relative activities are given immediately following

Table 4.2 Isotopes identified in preliminary spectra

	<u>Isotope</u>	<u>Half-life</u>	<u>Energy (kev)</u>
HgO	197-Hg	65 hr	190
	197m-Hg	55 min	133
	203-Hg	47 day	279
CeO	141-Ce	32.5 day	145
	143-Ce	34 hr	58,232,294

Table 4.3 Isotopes produced by irradiation of Hg for 3 days

<u>Isotope</u>	<u>Abundance</u>	<u>Half-Life</u>	<u>Cross- Section (barns)</u>	<u>Relative Activity</u>	
				<u>0 days</u>	<u>30 days</u>
197	.0015	65 hr	880.	19.2	.022
197m	.0015	24 hr	25.	1.48	0
199m	.1002	42.6 min	.02	2.67	0
203	.298	46.9 day	4.0	1	1
205	.0685	55 min	.04	28.2	0

Table 4.4 Isotopes produced by irradiation of Ce for 3 days

<u>Isotope</u>	<u>Abundance</u>	<u>Half-Life</u>	<u>Cross- Section (barns)</u>	<u>Relative Activity</u>	
				<u>0 days</u>	<u>30 days</u>
137	.0019	9 hr	6.0	8.6	0
137m	.0019	34 hr	.6	.05	0
139	.0025	140 day	1.0	.001	.0016
139m	.0025	60 sec	.04	8.8	0
141	.8850	32.5 day	.6	1	1
143	.1110	34 hr	1.0	4.8	.00001

irradiation for 3 days and following 30 days decay. The 3 day irradiation time was chosen because the  $^{203}\text{Hg}$  activity saturated in the high flux irradiation tube in three days, whereas the 30 days decay was required to remove most of the contaminants.

Sources were constructed consisting of 600 mg  $\text{CeO}$  and 750 mg  $\text{HgO}$  in graphite capsules. These were irradiated for 3 days in the high flux tube at McMaster reactor and allowed to decay for 30 days. Examination revealed that the  $\text{HgO}$  source had excessive leakage due to radiative heating and subsequent dissociation of  $\text{HgO}$  into the constituent vapours.

To alleviate this problem,  $\text{Hg}_2\text{F}_9$  which is considerably more stable than  $\text{HgO}$  was used. A quantity of 650 mg was sealed in quartz and heated at  $500^\circ\text{C}$  for 2 days with no observable effect. Following this it was irradiated under identical conditions as the  $\text{HgO}$  and found to be intact when removed from storage.

The spectra for  $^{141}\text{Ce}$  and  $^{203}\text{Hg}$  are shown superimposed in figure 4.3. The peaks due to the 279 and 145 keV photons are indicated as is the peak due to the Tl x-rays. These were obtained using a 2 inch  $\text{NaI(Tl)}$  crystal with relatively poor resolution. This will be discussed in greater detail in later sections. The sources were used separately so that only the two peaks from the  $^{203}\text{Hg}$  were

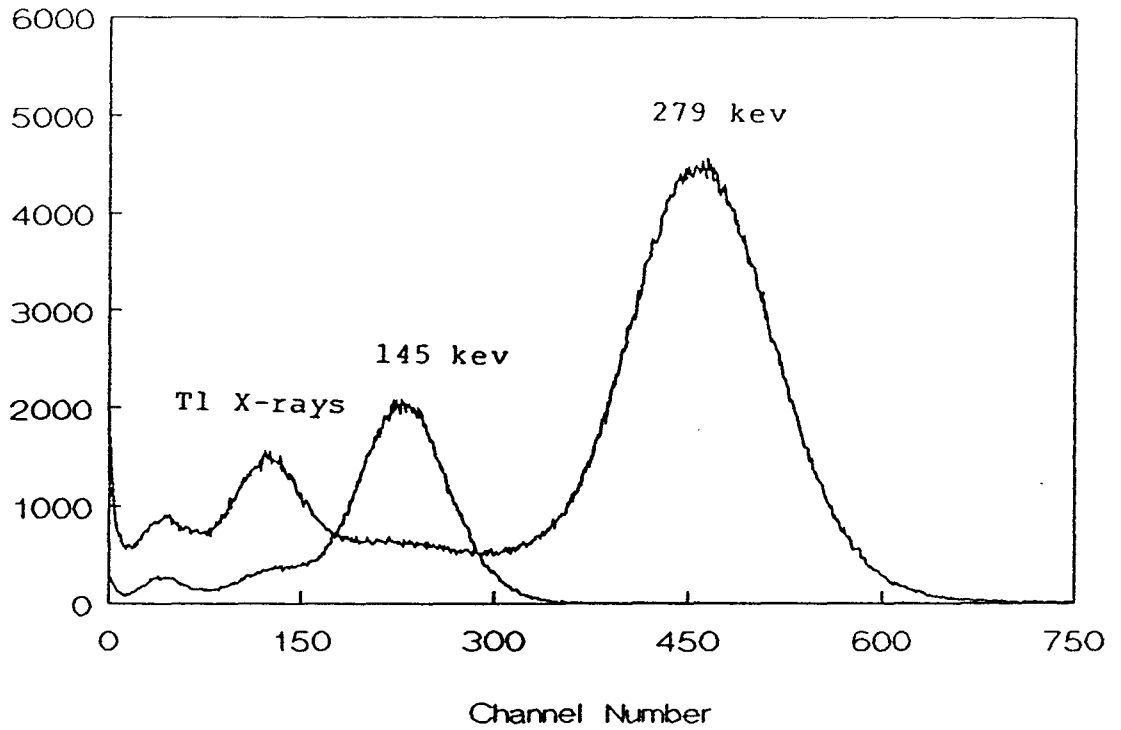


FIGURE 4.3 NaI spectra of  $^{203}\text{Hg}$  and  $^{141}\text{Ce}$  superimposed. The photopeaks at 145 and 279 kev are indicated along with the Tl X-rays.

measured simultaneously.

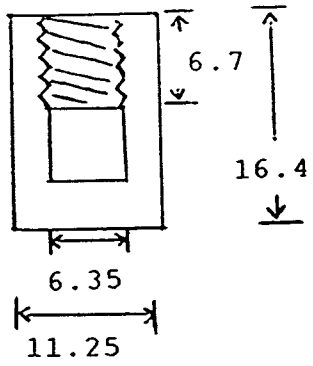
#### 4.3 Transmission measurement procedure

The transmission measurements were made using the modified rectilinear scanner mentioned in chapter 2, with further modifications to account for lower source activity. The  $^{141}\text{Ce}$  source consisted of  $\text{CeO}$  powder placed into a graphite capsule whereas the  $^{203}\text{Hg}$  source consisted of  $\text{Hg}_3\text{F}_2$  powder sealed in quartz. Following irradiation they were placed individually into a source holder. These are illustrated in figure 4.4. The source holder was placed into a lead castle and the beam was directed towards a detector collimator.

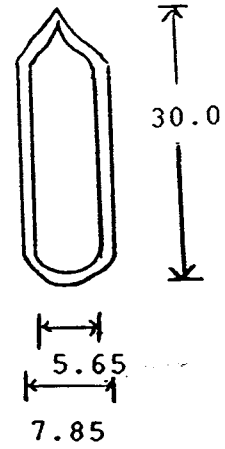
The detector signals were analyzed using two single channel analyzers with windows for two photopeaks, namely the 279 keV photon and Tl x-rays for  $^{203}\text{Hg}$ , or the single 145 keV photon for  $^{143}\text{Ce}$ . The windows were calibrated using a multi-channel analyzer. The SCA output was sent to a 16 bit counter interfaced to a NOVA computer as described in detail by Rowntree (1985). The counters were examined and cleared every second to prevent overflow and subsequent errors.

Two different detectors were used in the measurements. A 1.27 cm NaI detector which had been used for  $^{153}\text{Sm}$  was used for preliminary measurements. This was not ideal for measuring the 279 keV photons for two reasons.

Ce graphite screw  
capsule



Hg sealed quartz



dimensions in mm

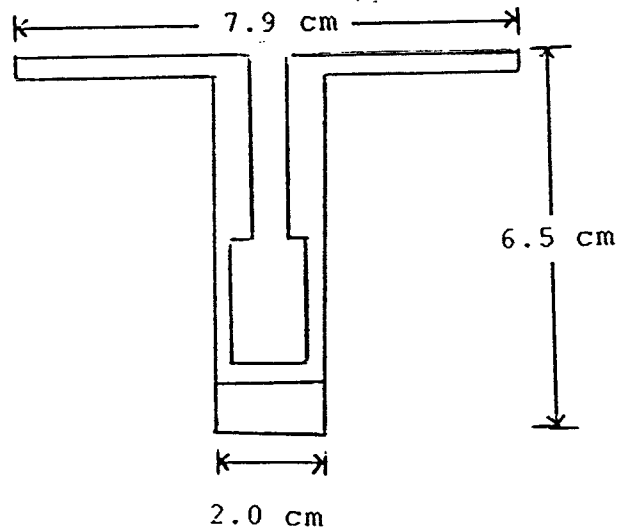


FIGURE 4.4 TPA source containers (top) and source holder (bottom).

Firstly, the probability of any type of interaction in the crystal is given by

$$P = 1 - \exp(-\mu t) \quad 4.3$$

where  $\mu$  is the linear attenuation coefficient for NaI and  $t$  is the thickness of the crystal. For a 1.27 cm crystal using attenuation coefficients from Mannhart (1976) this is 52% at 279 keV. Secondly, only a fraction of these will be photoelectric events, and appear in the photopeak. The rest will be Compton scattered and will deposit only a fraction of their energy in the crystal, with some of these appearing in the window of the lower energy photons. For 279 keV photons approximately 50% of the interactions will be Compton scattered contributing to cross-over.

The cross-over was found to be 34.3% for the small crystal. This was measured by filtering the 203-Hg source with 1 mm Ta, which afforded attenuation of the Tl X-rays by 6 orders of magnitude.

For later measurements a 5.08 cm NaI detector was used. The probability of any interaction in this crystal at 279 keV is 95%, however the fraction of Compton scattered photons will not change. This might suggest that the cross-over will be the same as for the smaller crystal. However the cross-over was reduced because the energy resolution of the detectors were different and the photons scattered within the detector will have a greater probability of

secondary interactions. A Compton scatter followed by a photoelectric interaction will not be distinguished from a single photoelectric event in the detector output and will appear in the photopeak.

The cross-over for the 5.08 cm NaI detector was found to be 12.6%. This was measured by using the Ta filter as before and was verified by measuring the transmission of the Tl X-rays through various thicknesses of steel. The transmitted intensity was fitted to a function of the form

$$I(t) = A \exp[-\mu(Tl)t] + B \exp[-\mu(279)t] \quad 4.4$$

where the parameter B is the initial intensity of the 279 keV photons multiplied by the cross-over fraction. The transmitted intensities are shown in figure 4.5, and are fitted by the following functions

$$I(279) = 2443 \exp(-.8771 t) \quad 4.5a$$

$$I(Tl) = 997 \exp(-5.9779 t) + 309 \exp(-.8771t) \quad 4.5b$$

The detector was held opposite the source castle, and a collimator was attached to the front of the detector holder as indicated in figure 4.6. The source collimator had a diameter of 5mm while the detector collimator was 8 mm in diameter (the source collimator had a diameter of 8 mm using the original HgO source). These did not allow high spatial resolution in the measurements, however the large bores were necessary to ensure high count rates from relatively weak sources.

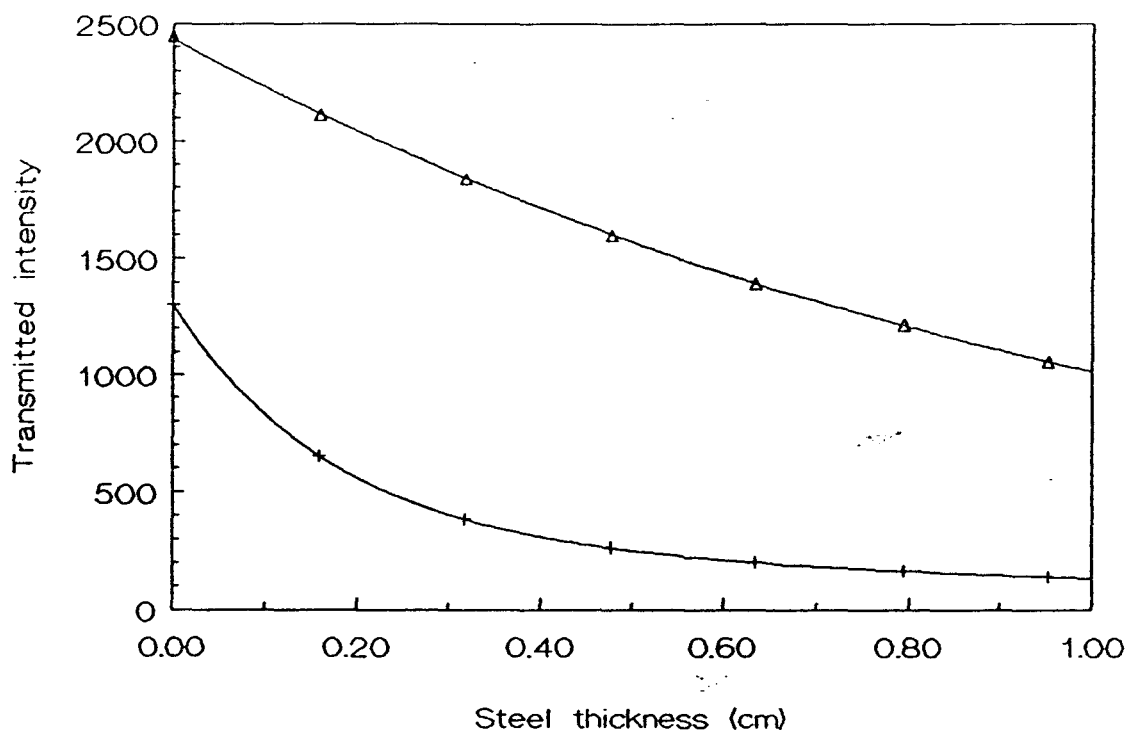


FIGURE 4.5 Transmitted intensity of  $^{203}\text{Hg}$  photons through steel showing the single exponential fit for 279 keV (▲) and the double exponential fit for Tl X-rays (+).

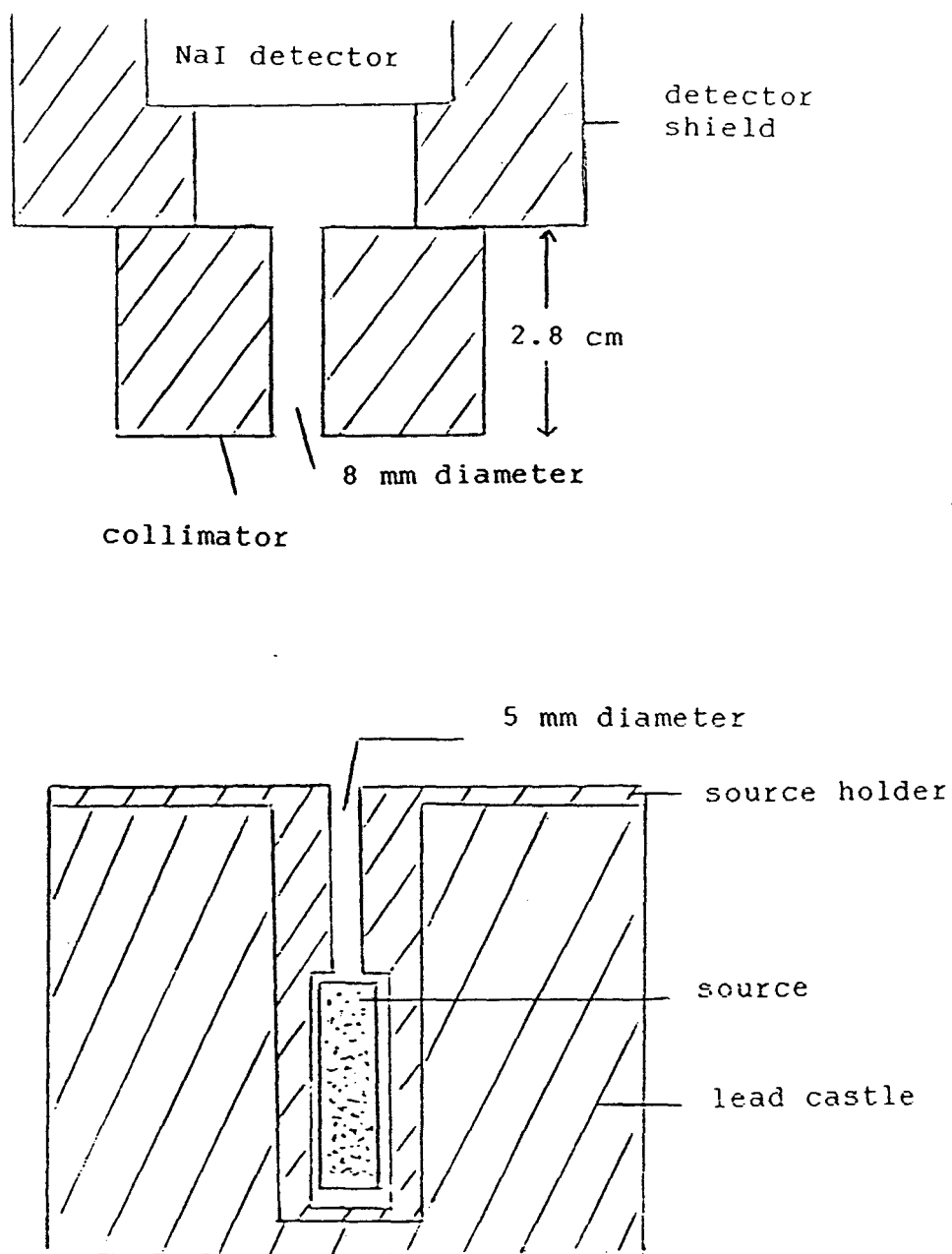


FIGURE 4.6 Schematic diagrams of detector holder and collimator (above) and source holder and lead castle (below).

The deadtime of the detection system was assumed to be non-paralyzable. In this model the ratio of observed to true count rates,  $n/m$ , is given by

$$n/m = 1 - n\tau \quad 4.6$$

where  $\tau$  is the pulse length corresponding to an interaction in the detector (Knoll 1979). Subsequent measurements were corrected for deadtime losses by inverting equation 4.6 to yield the true count rate as

$$m = n/[1-n\tau] \quad 4.7$$

The pulse length was determined by measurement of the deadtime by using a pulser to establish the ratio of observed to true count rates. This was performed for both  $^{141}\text{Ce}$  and  $^{203}\text{Hg}$  at different count rates, with the results plotted in figure 4.7. A straight line was fitted to these data using least squares with the slope of the line equal to the pulse length. This was found to be approximately 9  $\mu\text{s}$ .

#### 4.4 Phantom Materials

For the purpose of this work phantom materials were required to mimic the biological tissues fat, lean and bone as well as Vitallium. For the first three tissues, polyethylene, water and aluminum were chosen, primarily because they had been used for previous work, whereas for Vitallium, stainless steel was chosen. These two materials have similar compositions as indicated in table 4.5. One can almost think of Vitallium as stainless steel with the iron

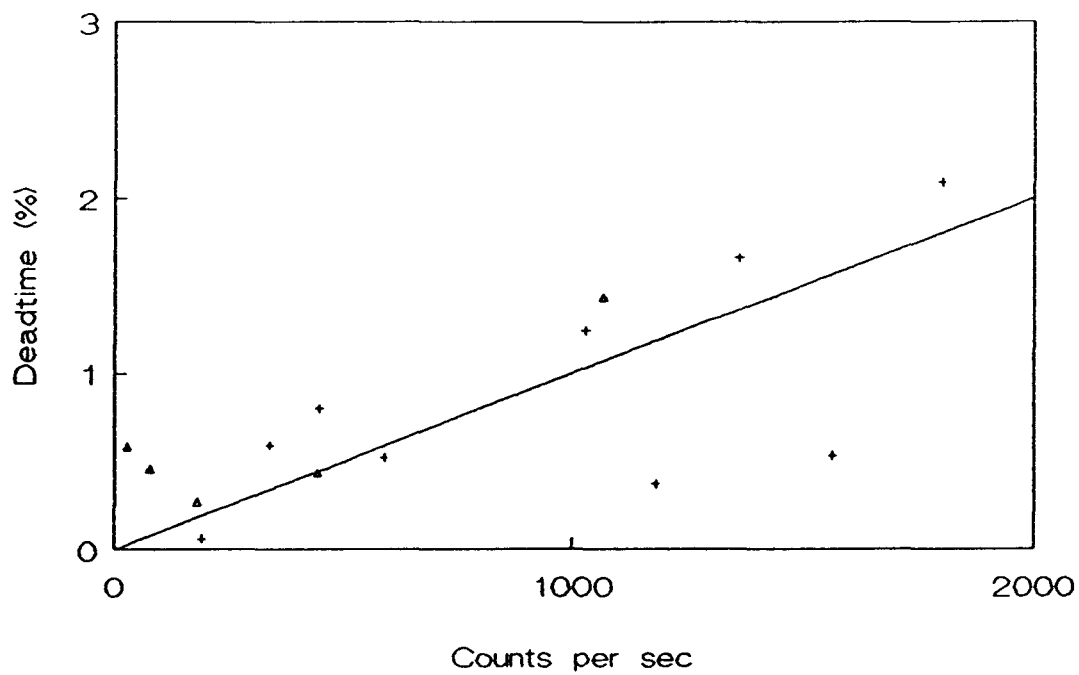


FIGURE 4.7 System deadtime as a function of source count rate for  $^{203}\text{Hg}$  (+) and for  $^{141}\text{Ce}$  ( $\Delta$ ).

Table 4.5 Composition of Vitallium and Stainless Steel

<u>Element</u>	<u>Atomic Number</u>	<u>Fraction (%)</u>	
		<u>Vitallium</u>	<u>Steel</u>
Carbon	6	.05	
Silicon	14	.75	1.00
Chromium	24	26.50	20.00
Manganese	25	.70	2.00
Iron	26		67.00
Cobalt	27	66.50	
Nickel	28		10.00
Molybdenum	42	5.50	

replaced by cobalt.

◆ The attenuation characteristics of the phantom materials were determined by transmission measurements using the 1.27 cm NaI detector and the original HgO source and the CeO source. The linear attenuation coefficients were determined by fitting the logarithm of the transmitted intensities to a straight line using least squares procedure. These were measured as accurately as possible with the weak source, with some transmitted intensities no greater than background. The mass attenuation coefficients were calculated by dividing by the densities of the phantom materials. These are given in table 4.6. In addition the difference between the measured phantom mass attenuation coefficients and the calculated tissue coefficients is given as a percentage of those for the tissues.

#### 4.5 Simulation of Phantom TPA

In order to determine the feasibility of TPA at the hip simulations similar to those in chapter 3 were performed. Linear attenuation coefficients were taken from table 4.6 in order to determine the inverse matrix of attenuation coefficients. For aluminum the evaluated inverse matrix elements were found to be 2.275, -22.15 and 24.851 for the Tl x-rays, 145 keV and 279 photons respectively.

As before, an initial intensity was chosen, and transmitted intensities were calculated using the

Table 4.6 Mass attenuation coefficient for phantom materials

Material (Tissue)	Density g/cm <sup>3</sup>	Mass attenuation coefficient (Differences %)		
		Tl X-ray	145 kev	279 kev
Polyethylene	0.93	.1769 <u>±.0016</u>	.1505 <u>±.0009</u>	.1179 <u>±.0025</u>
(Fat)	0.93	-4.0	-1.3	-5.1
Water	1.00	.1829 <u>±.0017</u>	.1520 <u>±.0018</u>	.1210 <u>±.0018</u>
(Lean)	1.06	0.3	2.1	0.7
Aluminum	2.71	.2336 <u>±.0047</u>	.1351 <u>±.0018</u>	.1138 <u>±.0032</u>
(Bone)	1.89	4.4	-6.9	1.9
Steel	7.86	.7236 <u>±.0048</u>	.1977 <u>±.0008</u>	.1100 <u>±.0007</u>
(Vitalium)	7.26	-10.4	-6.0	2.0

attenuation coefficients for the geometry shown in figure 4.8. Statistical fluctuations were introduced using a random Gaussian variate, and the aluminum thickness was recovered using the inverse matrix terms.

Aluminum thickness images were generated for three different thicknesses (0.25, 0.375 and 0.50 cm) with 0.85 cm of steel. Images for different intensities are given in figure 4.9. The noise amplitude was found to vary as  $31.3/\sqrt{N}$  where N is the number of transmitted photons in a region of soft tissue. This is considerably lower than that for TPA at the spine, and seems to suggest that TPA may be possible at reasonable doses.

#### 4.6 Phantom Verification of TPA

Preliminary phantom measurements were made using the 1.27 cm NaI detector and the weak HgO source with a purpose more concerned with establishing the validity of the TPA technique than with mimicking clinical measurements. Only three of the phantom materials were used, namely steel, aluminum and polyethylene. The elimination of water was necessary to ensure the most accurate reproducibility of transmission thickness when the sources were exchanged, since these materials were solid slabs. This was considered reasonable since the mass attenuation coefficients of water and polyethylene are similar for the three photon energies under consideration.

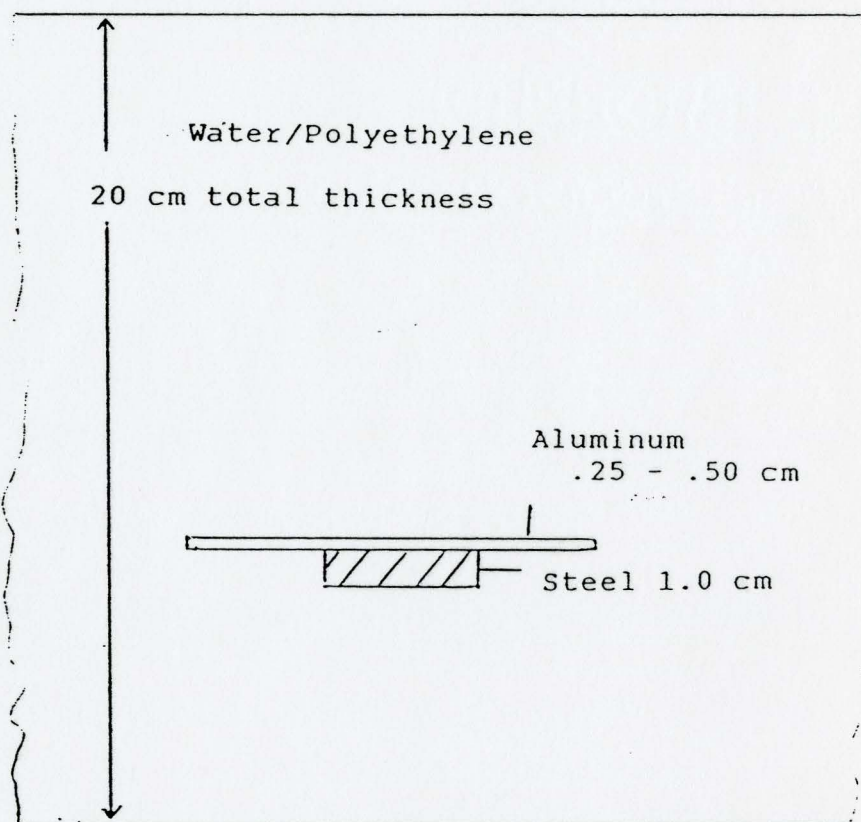


FIGURE 4.8 Phantom geometry used for TPA simulation.

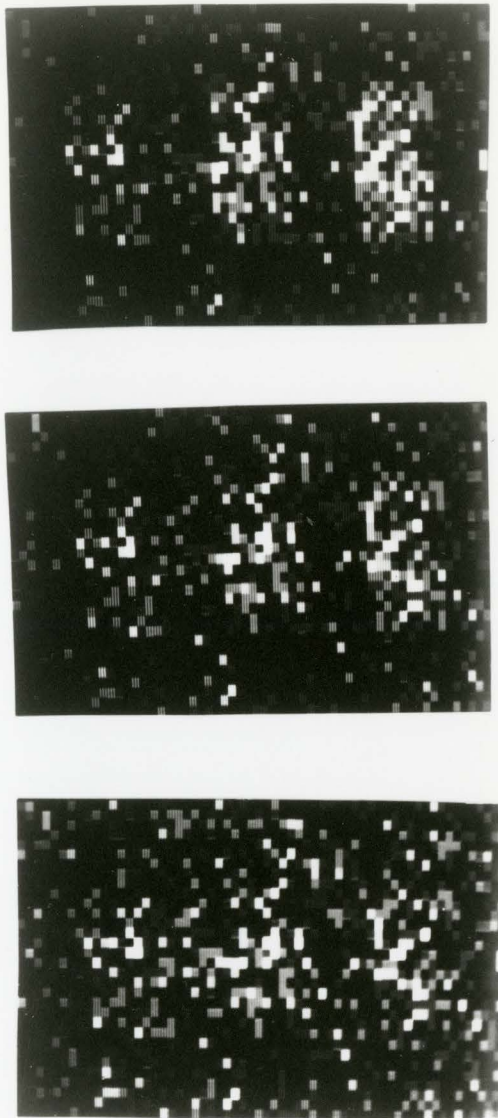


FIGURE 4.9 Simulated TPA images for phantom geometry with rectangular aluminum regions with thicknesses from left to right of 0.25, 0.375 and 0.5 cm. The images from top to bottom are with transmitted count rates of 10,000, 5000 and 1000 per pixel in the high energy channel.

The transmission measurements were performed using a constant thickness of 10 cm of polyethylene with different thicknesses of aluminum and steel. There were 16 different configurations of phantom materials as indicated in figure 4.10. It was hoped that the thickness of aluminum could be recovered from the attenuation factors using the previously calculated inverse linear attenuation coefficients or that correct inverse coefficients could be determined directly by fitting the aluminum thickness to the sum of inverse attenuation coefficients multiplied by attenuation factor.

Background was measured for 10 hours for the  $^{203}\text{Hg}$  source and for 3 hours for the  $^{141}\text{Ce}$  source. The background rates were 2022, 439 and 366 counts per hour respectively for the Tl X-rays, 145 and 279 keV photons. The unattenuated count rates were measured for 60 minutes for  $^{203}\text{Hg}$  and for 20 minutes for  $^{141}\text{Ce}$  and were 181432, 72065 and 66071 respectively for the Tl X-rays, 145 and 279 keV photons.

Transmission measurements were made for each combination of phantom materials for 60 minutes for  $^{203}\text{Hg}$  and 20 minutes for  $^{141}\text{Ce}$ . The measured count rates were corrected for background, source decay and dead time, and the cross-over to the Tl X-rays was corrected by the subtraction of 34.3% of the 279 keV count rates.

The  $^{203}\text{Hg}$  source was very weak following the leakage and was sealed in a different source holder than in

	0.000	0.314	0.662	0.976	Aluminum thickness
0.000	1	2	3	4	
0.159	5	6	7	8	
0.318	9	10	11	12	
0.477	13	14	15	16	
Steel thickness					

FIGURE 4.10 Phantom material thicknesses for various configurations, referred to by arbitrary numerical designation.

figure 4.6. The collimator in this instance was 8 mm in diameter, and the source holder sat above the source castle, reducing the source collimator to detector collimator distance.

The attenuation factors were calculated for each photon energy for each phantom combination and the validity of these were assessed by fitting the attenuation factors to a function of the form

$$Y(E) = \sum \alpha(E,i)t(i) \quad 4.8$$

where  $\alpha(E,i)$  is the linear attenuation coefficient for material  $i$  at energy  $E$ . The results for the fitted attenuation coefficients are compared to the previously measured (or expected) coefficients in table 4.7

The coefficients for 145 and 279 keV are reasonable. However the results for the Tl X-rays are not correct, especially for steel. The most likely explanation for this is that 279 keV photons are scattered within the phantom and are detected as Tl X-rays. This will result in falsely high Tl X-ray transmission rates with corresponding falsely low attenuation factors. This cross-over is seen in dual photon absorptiometry, and is corrected by choosing a cross-over factor which includes both cross-over in the patient and in the detector. Invariably this is a function of patient thickness, however it varies slowly enough that a single value can be used accurately over the normal range of

Table 4.7 Fitted and Measured Linear Attenuation Coefficients for Phantom Materials

Energy	Polyethylene	Aluminum	Steel	
Tl X-rays	.158	.542	3.089	F
	.165	.633	5.687	E
145 kev	.140	.370	1.557	F
	.140	.366	1.554	E
279 kev	.113	.293	.929	F
	.110	.308	.864	E

F - fitted

E - expected

patient thicknesses.

In order to determine the appropriate value of cross-over to use, the expected attenuation factors were calculated for each phantom configuration and were set equal to

$$Y(T1) = \ln[(I_0(T1) - X_0 I_0(279)) / (I(T1) - X_0 I(279))] \quad 4.9$$

which was inverted to give the required cross-over using the following expression.

$$X_0 = [I_0(T1) - I(T1) \exp(Y(T1))] / [I_0(279) - I(279) \exp(Y(TL))] \quad 4.10$$

The required cross-overs are given in table 4.8 and range from 44% to 80% over a very small range of phantom thickness (10-12 cm). To correct for patient cross-over using this method is probably prone to error.

Another approach to correct for the cross-over is to assume that the additional cross-over due to scatter is a fraction of the incident 279 keV flux rather than the transmitted flux. The cross-over would be identical for all phantom configurations which have approximately equal thicknesses. With a constant scatter term the attenuation factor is given by

$$Y(T1) = \ln \frac{I_0(T1) - X_0 I_0(279)}{I(T1) - X_0 I(279) - \text{Scat}} \quad 4.11$$

where  $X_0$  is the cross-over within the NaI crystal. This can be solved to give

$$\text{Scat} = [I(T1) - X_0 I(279)] - \exp(-Y(T1)) [I_0(T1) - X_0 I_0(279)] \quad 4.12$$

Table 4.8 Cross-over factor required for phantom configurations.

Phantom Configuration	Cross-over (%)
1	43.9
2	49.3
3	50.5
4	55.8
5	64.4
6	64.2
7	59.2
8	65.0
9	71.2
10	70.5
11	65.8
12	70.7
13	70.6
14	78.4
15	79.8
16	73.8

The scattered flux was determined using equation 4.12 for all phantom configurations with a mean value of 4428 counts per hour. The attenuation factors were calculated using this result and equation 4.11 and are given in table 4.9 together with the expected attenuation factors. There is general agreement. Another interpretation of equation 4.11 is that the scatter term is in fact an incorrect measurement of the background. This seems unlikely since the correction is twice the measured background rate, which was determined to within 1% by counting for 10 hours.

The inverse linear attenuation coefficients were determined by least squares fitting of the thickness of aluminum to the linear combination of attenuation factors as

$$T(\text{al}) = \sum \kappa(E)Y(E) \quad 4.13$$

where  $\kappa(E)$  is the inverse linear attenuation coefficient. These were found to be  $2.05 \pm 0.61$ ,  $-16.51 \pm 4.82$  and  $17.42 \pm 5.00$  respectively for Tl X-rays, 145 and 279 keV. These compare favourably with the calculated counterparts used in the previous section of 2.27, -22.15 and 24.85.

The thickness of aluminum was calculated using the inverse coefficients and is given in table 4.10. The thickness of aluminum was recovered using TPA and the root mean squared deviation for the phantom configuration was 0.25 cm aluminum. This is not discouraging since the source was very weak (approximately 50 counts per second in the Tl

Table 4.9 Attenuation factors for phantom configurations

Phantom Configuration	Expected	Scatter Flux
1	1.61	1.69
2	1.81	1.87
3	2.03	2.11
4	2.23	2.28
5	2.51	2.42
6	2.71	2.66
7	2.93	2.99
8	3.13	3.14
9	3.41	3.15
10	3.61	3.42
11	3.83	3.86
12	4.03	4.03
13	4.32	3.99
14	4.51	4.00
15	4.74	4.28
16	4.93	5.13

Table 4.10 Comparison of aluminum thickness by TPA with expected aluminum thickness

Phantom Configuration	Aluminum Thickness (cm)	
	Expected	TPA
1	0.000	0.099
2	0.314	0.405
3	0.662	0.633
4	0.976	0.478
5	0.000	0.353
6	0.314	0.520
7	0.662	0.415
8	0.976	0.701
9	0.000	0.337
10	0.314	0.783
11	0.662	0.408
12	0.976	0.928
13	0.000	-0.037
14	0.314	0.459
15	0.662	0.551
16	0.976	0.893

X-Ray window) and a stronger source may result in more precise measurements. This will be discussed in the next section.

#### 4.7 Variance of Phantom TPA

The shortcomings of the preliminary phantom measurements were a result of two factors. The first is that the  $^{203}\text{Hg}$  source was very weak, so that transmitted count rates were not much greater than background. The second is that the cross-over of the 1.27 cm NaI detector was excessive. For the next set of phantom measurements the 5.08 cm NaI detector was used with the  $\text{Hg}_2\text{F}_2$  source. The aims of these measurements were to determine the inverse linear attenuation coefficients more accurately and to determine the precision of the TPA technique.

As mentioned previously, the transmission measurements were made with only a single source in the holder. In order to measure a two-dimensional phantom with the rectilinear scanner two separate scans would have to be made, generating two sets of transmission data. This introduced the possibility of misalignment of the data sets. Although one can conceive of several arrangements to prevent misalignment, for the purpose of these measurements it was more expedient to make pseudo-scan images and to leave misalignment correction as a future refinement. This involved making repeated measurements at a single site on

the phantom with both sources before moving to a different site. These sets of data were combined mathematically to generate TPA images.

The combinations of thicknesses of phantom materials were similar to those in the previous section, with polyethylene at 9.7 cm and aluminum ranging from 0.314 to 0.976 cm. Only one thickness of 0.794 cm steel was used. These were combined to yield a pseudo-scan with the combinations shown in figure 4.11. This pseudo-scan can be considered as three sets of data, each a single thickness of aluminum with steel in the middle. Given the 5 mm diameter of the source collimator, the images would represent real images with dimensions 12 by 8 cms, with aluminum 7 cm wide and steel 2 cms wide. These are somewhat representative of clinical dimensions, except perhaps for the polyethylene thickness. They should reproduce all the features of proper scanned TPA without the difficulties of misalignment, and of course with perfect spatial resolution.

Background was measured for each of the sources for 60 minutes and was found to be 1.55, 0.72 and 0.85 counts per second respectively for Tl X-rays, 145 and 279 kev photons. The unattenuated count rate was measured for 4 minutes and found to be 1462.4, 2620.4 and 2532.6 counts per second respectively for Tl X-rays, 145 and 279 kev photons.

The transmitted intensity was measured for the two

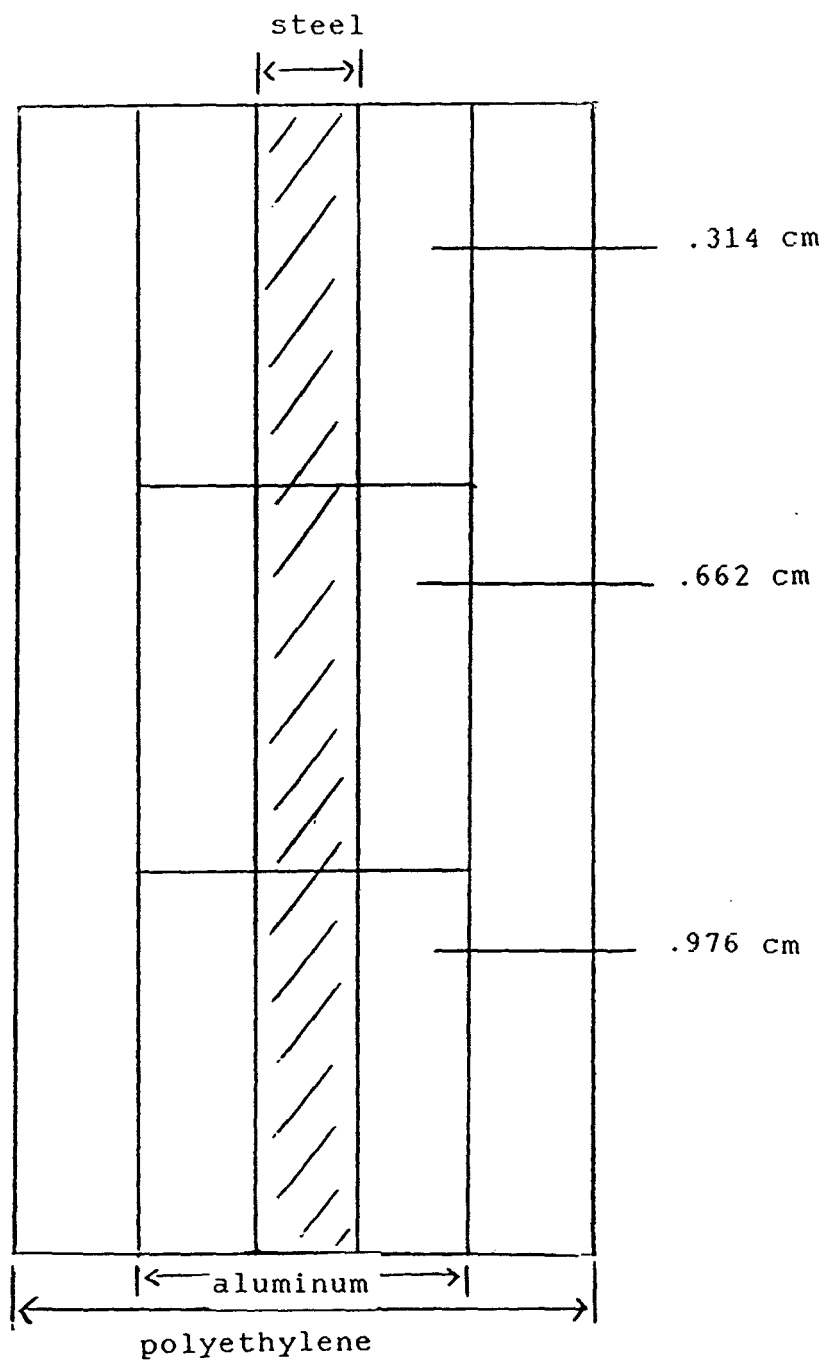


FIGURE 4.11 Phantom material thicknesses for TPA pseudo-scans.

sources independently and was corrected for background, deadtime and source decay as described in the previous section. Measurements were taken for different lengths of time including 1, 5, 10, 50 and 100 seconds per pixel. These data were combined to generate the sets of transmission data for each photon energy.

A cross-over correction of 12.66% was used to remove the cross-over photons from the 279 keV to the Tl X-ray window. However, as in the previous section, this procedure did not correct for cross-over from within the phantom. The linear attenuation coefficients for the various materials were determined using mean attenuation factors for the entire set of phantom data. These are given in table 4.11. The attenuation coefficients are correct for the 145 and 279 keV photons but are not correct for the Tl X-rays.

An analysis similar to that in the previous section was performed to determine the scatter flux. Unlike the previous measurements the cross-over required to give accurate transmission factors was relatively constant at 16.75% with a range of 16.5 to 17.0% for all phantom combinations with aluminum. It was lower at 15.9% at the region with only polyethylene. The more constant cross-over is probably due to better collimation of the source and increased air gap from the phantom to the detector collimator.

Table 4.11 Fitted and Measured Linear Attenuation Coefficients for Phantom Materials

Energy	Polyethylene	Aluminum	Steel	
Tl X-rays	.156	.520	2.907	F
	.165	.633	5.687	E
145 kev	.141	.368	1.552	F
	.140	.366	1.554	E
279 kev	.115	.333	.831	F
	.110	.308	.864	E

F - fitted

E - expected

The inverse linear attenuation coefficients which had been calculated earlier (2.27, -22.14, 24.85) were used to recover the aluminum thickness from the transmission data. The results, however, were incorrect, and are summarized in table 4.12. The attenuation factors from the pseudo-scans were used to determine the best values for the inverse linear attenuation coefficients by least squares fitting of equation 4.13. These were found to be 0.36, -3.7, 4.43 and were used to recover the aluminum thickness with more success as indicated in table 4.12 and by the pseudo-scan images in figure 4.12.

The precision of TPA was determined by calculation of the RMS deviation of the measured aluminum thickness for each thickness both at sites with and without steel. This was found to be quite different if steel was or was not present, but did change appreciably with the thickness of aluminum. The RMS deviation without steel present was found to vary as  $0.242/\sqrt{T}$  cm aluminum with T the counting time in seconds per pixel. The RMS deviation of regions with steel present was  $2.36/\sqrt{T}$  cm aluminum.

These results are further complicated by the fact that the transmission through the steel included pixels with countrates which were negative when the background, cross-over and scatter flux were subtracted. These pixels could not be used to calculate attenuation factors and were

Table 4.12 Aluminum thickness recovered by TPA for 10 seconds per pixel pseudo-scan.

Aluminum Thickness	Calculated Coefficients	Fitted Coefficients
	No Steel	
0.314	-1.20	0.25
0.662	0.21	0.54
0.976	1.00	0.72
	Steel	
0.314	-1.04	0.49
0.662	-0.09	0.67
0.976	1.14	0.91

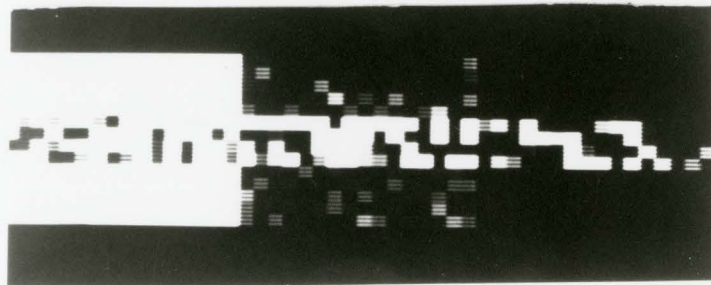
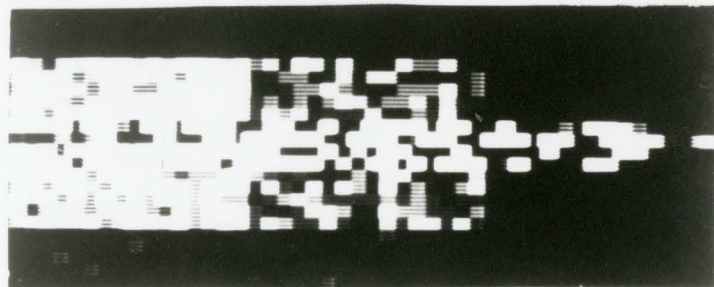
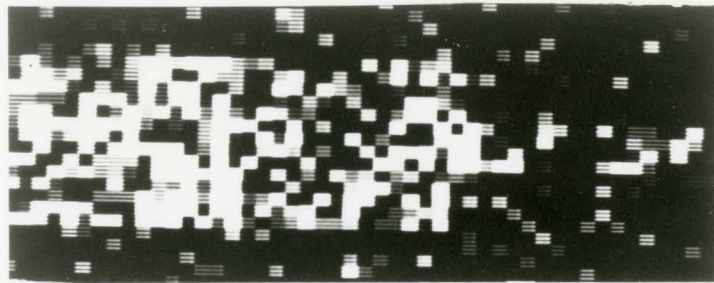


FIGURE 4.12 Phantom pseudoscans for rectangular plates of aluminum of thickness from left to right of 0.976, 0.662 and 0.314 cm. The images from top to bottom were obtained with counting times of 1, 5 and 10 seconds per pixel.

ignored. The fraction of pixels which had less than one count in the Tl X-ray window depended upon the counting time ranging from 73% at 1 second per pixel to 40% at 10 seconds per pixel. The fraction did not change considerably for counting times greater than 10 seconds per pixel. Whether these pixels can be ignored, leaving blank pixels in the TPA image, or whether some arbitrary low count threshold is used the result will be a biased TPA measurement.

From the results of the phantom measurements it appears that TPA using  $^{203}\text{Hg}$  and  $^{141}\text{Ce}$  is possible under some circumstances. However, there is an important question which deserves consideration. Is it possible to make TPA measurements in reasonable counting times with high precision? This will be addressed by Monte Carlo simulation of the photon transmission to determine the scatter flux for various geometries. The Monte Carlo code is described in the next chapter, and the analysis will be given in the following chapter.

## CHAPTER 5

### DESCRIPTION AND VALIDATION OF MONTE CARLO CODE

#### 5.1 Introduction

Monte Carlo methods are a well established technique to solve photon transport problems in radiological applications (Turner, Wright and Ham 1985). The particular problem of the distribution of scattered photons has been addressed for X-ray transmission through tissue (Kallendar 1981, Chan and Doi 1983, Chan and Doi 1986, Persliden and Carlsson 1986, Boone and Seibert 1988). In this work the distribution of photons scattered from pencil beams of monoenergetic photons will be investigated as a function of transmission thickness and photon energy.

The Monte Carlo method is used to obtain statistical estimates of a physical parameter. Pseudorandom numbers are used to sample distributions which model the physical processes of scattering and absorption as photons penetrate materials. Clearly the algorithm used to generate the pseudorandom numbers must be suitable for the task and the physical processes must be modelled correctly.

This chapter is devoted to a description of the code including the random number generator and the distribution sampling techniques as well as a validation of the sampling

and scoring techniques. The Monte Carlo code used in this work was implemented in compiled BASIC and run using IBM® as well as ATARI ST® personal computers. The code for these are included in appendix 3.

### 5.2 Pseudorandom Number Generator

A pseudorandom number generator is an algorithm which can generate successive numbers, usually in the range 0 to 1, which must approximate a random selection as defined by statistical tests. Implemented on a binary computer, it will have a finite period, after which the selection of numbers will be a repetition of the previously selected set of numbers. The ideal pseudorandom number generator will have two important qualities: it will have a long period and will meet all statistical tests which are applied. A generalized feedback shift register was chosen as the pseudorandom number generator for this work since it was most capable of meeting the aforementioned requirements.

A feedback shift register (Lewis 1975) is based upon a primitive polynomial of the form 5.1 using an algorithm which will be described later.

$$x^p + x^q + 1 \quad 5.1$$

It will have period  $2^p - 1$  with the order of the polynomial,  $p$ , usually limited by the wordsize of the computer. The values of  $p$  and  $q$  are restricted to a few combinations

including the useful combination of  $p=31$  and  $q=13$  which gives a generator with a long period. Unfortunately this requires a 32 bit integer, which was not available on the computers used in this work.

A generalized feedback shift register uses a set of  $p$  integers each of wordlength  $w$ . The set of bits at a given position in each integer form a single shift register of  $p$  bits (figure 5.1), with  $w$  such shift registers in all, as the columns in figure 5.1. If these shift registers (each of which is a random number generator) are independent, then the rows in figure 5.1, the integers themselves, will also generate pseudorandom numbers. The independence of the columns is assured by proper initialization of the set of integers (Lewis 1975). The set can be stored at the end of any program to be used as an initialized set for subsequent use.

The values  $p=31$  and  $q=13$  were used with a set of 31 integers of length 16 bits. The algorithm is indicated in figure 5.2 in which the random number is chosen by rotating a pointer through the set of integers rather than actually shifting, and the feedback is provided by the exclusive OR operation (a Boolean algebra operation on two logical variables which returns a true value if either is true but returns a false value if both are true or both are false). The values 0 and 1 are generated because there are

```
1 0 0 0 1 1
0 0 1 1 1 0
1 1 1 0 1 0
1 0 0 1 0 0
1 0 1 0 1 1
0 1 1 0 0 0
0 0 1 0 0 1
1 1 0 0 0 1
0 1 0 1 1 1
0 0 0 1 0 0
```

**Figure 5.1** Illustration of division of set of  $p=10$  words of length  $q=6$  (rows) into a set of 6 shift registers of 10 bits (columns).

```
k ← k + 1  
If k > p then k ← 1  
j ← j + q  
If j > p then j ← j - p  
W(k) ← W(k) XOR W(j)  
Rand ← W(K) / Wmax
```

Figure 5.2 Scheme of random number generator in which Rand is the random number given by division of  $W(k)$  by the largest integer  $W_{max}$ . A pointer,  $k$ , refers to a location in a table of length  $W$  which is the lowest order bit in the 31 bit column. The other pointer,  $j$ , refers to the location of the bit used for the feedback.

considerably less integers possible from a 16 bit word than the period of the random number generator. The complete cycle of these integers, including 0 and 1, is generated repeatedly, however in different order until the period of the random number generator is completed.

Statistical tests of the random number generator are included in appendix 1 and the BASIC code for the random number generator is included in appendix 3.

### 5.3 Overview of Monte Carlo Code

The overall objective of the Monte Carlo simulation is to represent the response of the physical experiment using a mathematical model that describes the behaviour of the photons. The geometry of the source and detector as well as source and detector collimators are parameters which can be adjusted in the simulation to determine the characteristics of the apparatus, or to optimize the physical process. Frequently parameters related to the geometry are entered explicitly in the Monte Carlo code for generation or scoring of photons, although this restricts the usefulness of the particular simulation. In this work a more general approach is taken, using a pencil beam of radiation to determine the point source response of a given patient transmission geometry. Following simulation, the response can be convolved with an arbitrary distribution, representing the source configuration, and can be scored for

an arbitrary detector configuration.

The point source response is generated by determining the probability per incident photon of transmission through a semi-infinite slab of given thickness and composition. As illustrated in figure 5.3, there are three classes of transmitted photons: those with no interactions or directly transmitted, those with a single scatter, and the multiply scattered photons. Of these, the directly transmitted probability can be determined directly from the exponential transmission probability, while the singly scattered probability is given by the integral of the photon flux multiplied by the scatter probability through the slab. Only the multiply scattered component cannot be calculated easily and must be estimated using Monte Carlo simulation (although it is convenient to determine the single scatter component by Monte Carlo as well).

In this work the scheme is to determine the point source response for transmission by determining the scattered contribution using Monte Carlo, and to estimate the response of typical experimental situations by convolution with source distributions, and scoring for detector arrangements. This is similar to work by Kalendar (1981), Chan and Doi (1983, 1986) and Boone and Seibert (1988) who performed simulations for X-ray transmission, producing distributions of scattered photons as a function

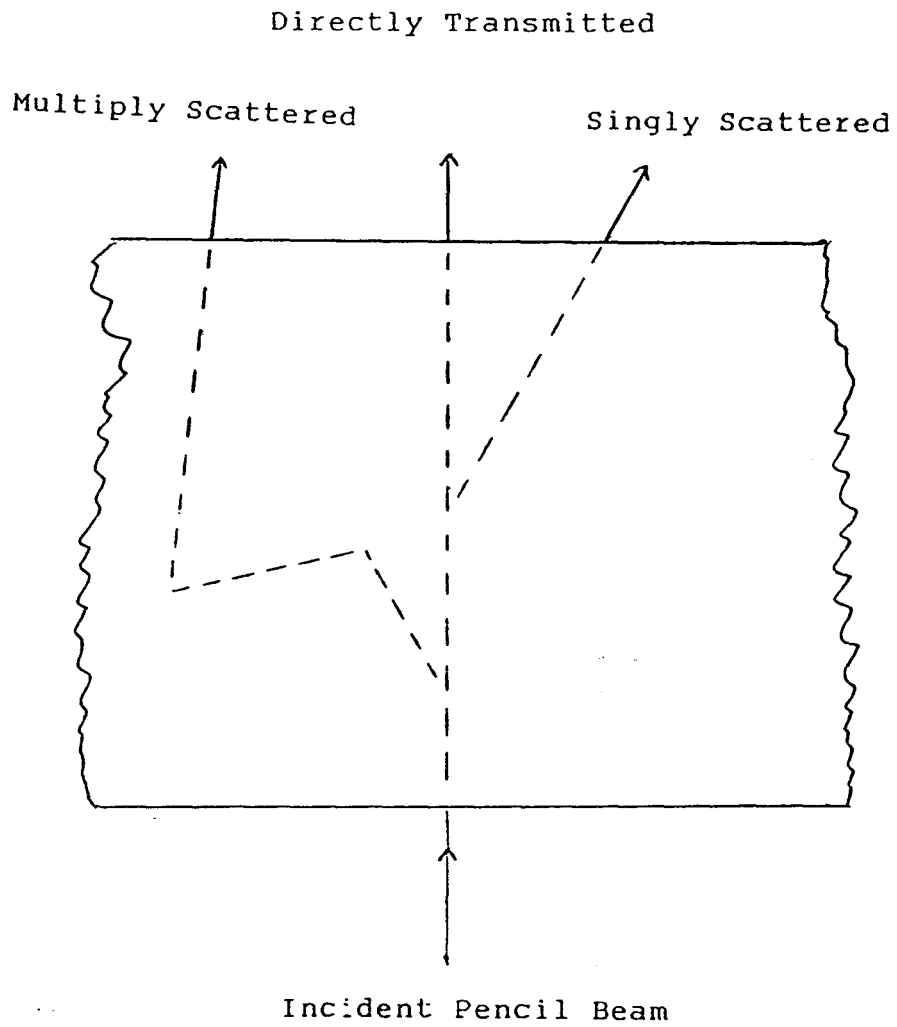


FIGURE 5.3 Mechanisms for photons to be transmitted through a slab of tissue.

of distance from the pencil beam and angle of emergence for a variety of high voltages and thicknesses. In this work however, the photons are mono-energetic, and the energy response of the detector must be considered. Distributions of singly and multiply scattered photons will be generated as a function of energy, position and angle, which can be used for characterization of the experimental apparatus.

#### 5.4 Mechanics of Photon Simulation

The essence of the Monte Carlo method for photon transport is the simulation of the random trajectories of numerous photons in order to estimate the behaviour of real photons in experimental conditions. The trajectory of a single photon is described as a set of state vectors, each of which is a set of parameters which describe the photon at an interaction vertex. These parameters may be real quantities such as position in space, direction of travel, or energy, or they may be contrived such as survival weights. In general, the history of a single photon begins with assigning initial values to the parameters which comprise the state vector. Subsequent state vectors are calculated recursively by determining pathlengths to the next interaction vertex and interaction outcomes by random sampling of the appropriate probability distributions. This procedure is continued until the photon is no longer within the volume of simulation.

For the particular simulation in this study, the state vector consisted of eight parameters: three Cartesian coordinates describing the position of the photon in space, three direction cosines describing the direction of the photon, the energy of the photon and the weight of the photon. The pencil beam of radiation was chosen to be along the positive z axis.

The photon history consisted of the following steps: 1 - creation of the photon at the origin of Cartesian space, 2 - selection of a path length to the next interaction vertex, 3 - determination of new interaction vertex, 4 - selection of either a Coherent or Compton interaction and adjustment of the photon weight by the survival weight, 5 - sampling for the scatter angle and new energy of photon, 6 - calculation of new direction. The photon history was terminated at step 3 if the next interaction vertex was not within the simulation volume, at step 4 if the weight fell below a predetermined value or at step 5 if the energy fell below a predetermined value, usually 20 kev.

Each of these processes is described in more detail, with descriptions of the probability distributions and the sampling techniques which were used in appendix 2. The corresponding BASIC code subroutines are included in appendix 3.

### 5.5 Scoring Scatter Flux

The scattered flux at a detector can be simulated directly by scoring the weight of each photon when it escapes the simulation region either missing or hitting the detector. In the latter case the plane fluence is given by the mean score over the area of the detector, which can be given as a function of photon energy or direction if desired. For convolution of the pencil beam scatter probability with the source geometry many scoring elements may be used. For high resolution these must be small which will adversely affect precision of the simulation.

An alternative to direct scoring is analogue scoring using a collision density estimator (Carter and Cashwell 1975, Persilden 1986). The plane fluence of photons scattered from a given interaction vertex by a given scattering process to a scoring point is given by

$$\phi = \frac{\cos\theta_3'}{\sigma r} e^{-\frac{(\mu(E')r)}{2}} \frac{d\sigma(\theta_0)}{d\Omega} \quad 5.2$$

where  $\mu(E')$  is the linear attenuation coefficient of the scattered photon,  $r$  is the distance from the interaction vertex to the scoring point,  $\theta_3'$  is the polar angle of the scattered photon and  $\sigma$  is the total cross-section for all interactions. The geometry of this is illustrated in figure 5.4. The scoring points can be situated with as fine a

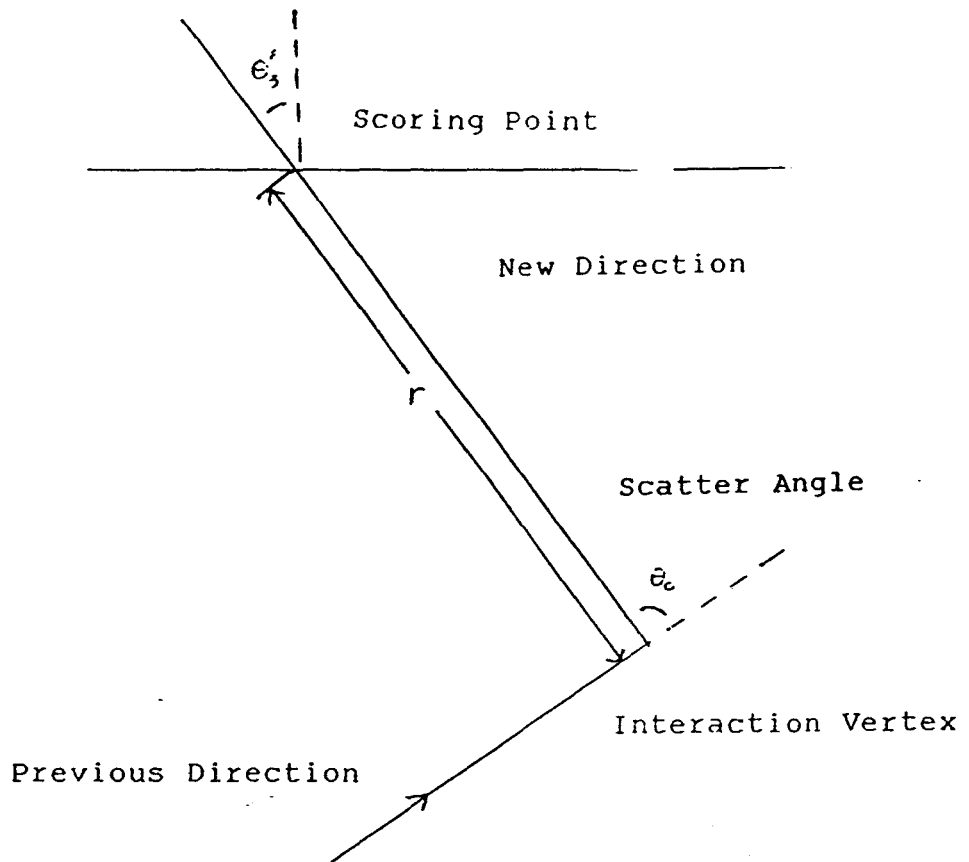


FIGURE 5.4 Geometry of collision density estimator.

resolution as desired and the scattering can be scored at each interaction vertex, thereby generating a series of fluences: those due to single, double, triple, etc. scatters. In this work single and multiple scattered fluences were obtained.

### 5.5.1 Mechanics of Analogue Scoring

The plane flux at a scattering point was found for both coherent and Compton scattering as a function of radius from the point of transmission of the pencil beam. The total cross-section was determined by using the linear attenuation coefficients from the tables described earlier using the relation

$$\sigma = \frac{\mu MW}{p Na} \quad 5.3$$

where MW, p and  $\mu$  are the molecular weight, density and linear attenuation coefficient of the composite material and Na is Avogadro's number. The distance to the scoring position, r, is given by

$$r = [(x'-x)^2 + (y'-y)^2 + (z'-z)^2]^{1/2} \quad 5.4$$

where (x,y,z) and (x',y',z') are the cartesian coordinates of the interaction vertex and scoring point respectively. The direction cosines of the scattered photon are given by

$$\cos\theta_1' = (x'-x)/r \quad 5.5a$$

$$\cos\theta_2' = (y'-y)/r \quad 5.5b$$

$$\cos\theta_3' = (z'-z)/r \quad 5.5c$$

and the cosine of the scattering angle is given by the dot product of the direction cosines

$$\cos\theta_0 = (\cos\theta_1, \cos\theta_2, \cos\theta_3) \cdot (\cos\theta_1', \cos\theta_2', \cos\theta_3') \quad 5.6$$

The linear attenuation coefficient of the scattered photon is found from the tables described earlier, and the differential cross-sections are found using equations A2.11 and A2.19 using the tables of form factors and scattering factors described earlier.

### 5.6 Variance Reduction

A major difficulty with the collision density estimator is estimating the flux at a point which is on the surface or entirely contained within the simulation volume. This arises from the  $1/r^2$  term in equation 5.2 which is unbounded as  $r \rightarrow 0$ . Several solutions to this have been proposed (Kalos 1962, Steinberg and Kalos 1971) which suggest that the variance of the estimator is bounded by reselecting a scattering point if the original interaction vertex is within a small volume about the scoring point. This reselected point is randomly sampled using a distribution which compensates for the  $1/r^2$  term in the flux calculation. The simplest such volume is a sphere with a radius,  $R_s$ , which depends upon the mean free path of the photons in the medium (this will be discussed later). Williamson (1987) showed that this reselection is equivalent to using the mean value of  $1/r^2$  over the sphere for any

interaction vertex within the sphere.

If the flux must be determined at a point on the surface and the angular flux distribution is required, the sphere is not an appropriate reselection volume since it involves the contribution over  $4\pi$  solid angle. The reselection volume was set to be a cone of solid angle  $\Delta$  equal to the angular scoring resolution with length  $R_s$  as illustrated in figure 5.5. The mean value of  $1/r^2$  from the scoring point over this volume is given by

$$\langle 1/r^2 \rangle = \int_0^{R_s} \int_0^{\Delta} \frac{r \, dr \, d\Omega}{Vr} \quad 5.7$$

where  $V$  is the volume of the reselection volume,  $\Delta R_s^3/3$ . The solution of equation 5.7 is given by

$$\langle 1/r^2 \rangle = \Delta R_s/V = 3/R_s^2 \quad 5.8$$

This is equivalent to substituting  $R_s/\sqrt{3}$  for  $r$  in equation 5.2 whenever an interaction vertex is within the reselection volume.

Steinberg (1971) suggested that for a spherical reselection volume the optimal value for  $R_s$  was given by  $1/\mu$  where  $\mu$  is the linear attenuation coefficient of the scattered photon. This was tested for the conical reselection volume by calculating the single scattered plane flux for different reselection lengths and comparing the results to those for direct simulation scoring. The

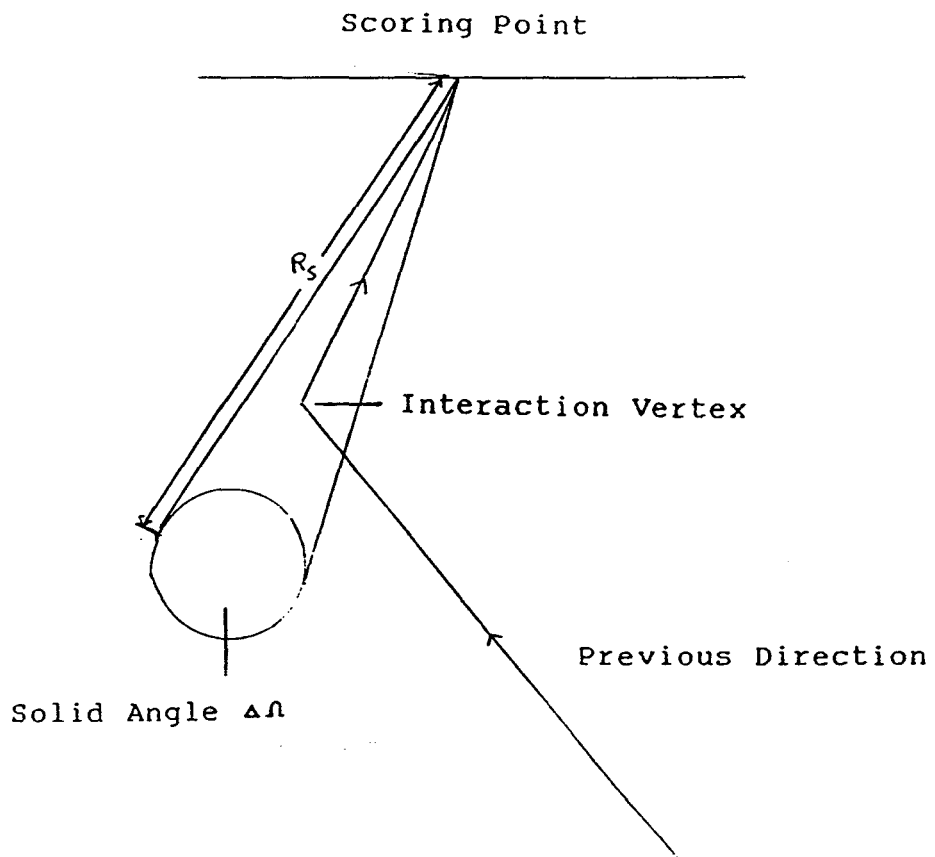


FIGURE 5.5 Reselection volume for collision density estimator.

simulation was performed through 20 cm water for 150 keV photons using 10,000 photons for analogue scoring and 500,000 photons for direct scoring (with similar precision).

The results are shown in figure 5.6 for scoring at the site of the pencil beam and in figure 5.7 for scoring at a position away from the pencil beam. In each of these the analogue scoring flux in arbitrary units is plotted for different reselection lengths, and the direct scoring flux is included for comparison. The analogue scoring flux is equal to the direct scoring flux at a reselection length approximately corresponding to the value  $1/\mu$  of 6.6 cm which is in agreement with the suggestion of Steinberg. The reselection length of  $1/\mu$  was used for further simulations. Results and further analysis will be given in the next chapter and used to analyze the feasibility of TPA at the hip.

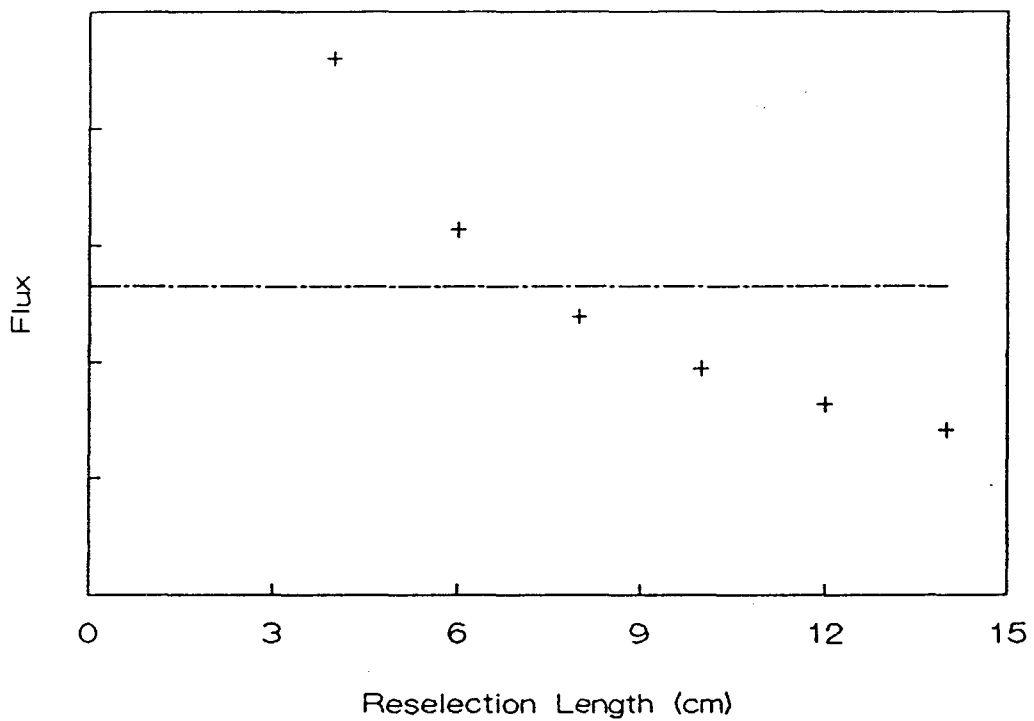


FIGURE 5.6 Comparison of analogue scoring (+) with direct scoring for different reselection lengths for a scoring point on the pencil beam.

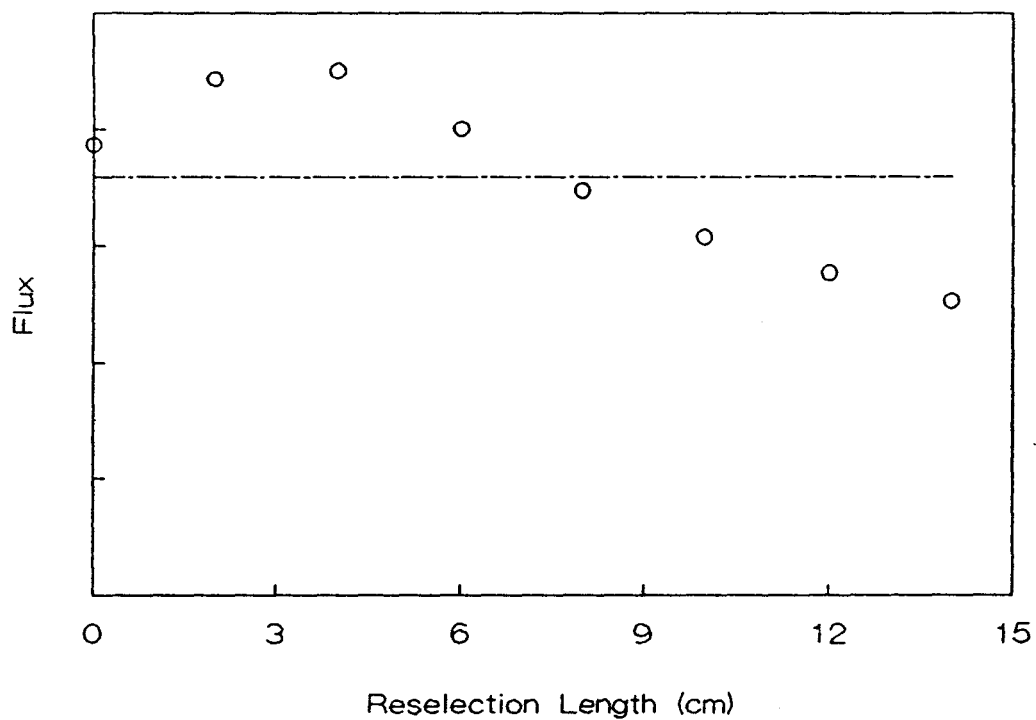


FIGURE 5.7 Comparison of analogue scoring (○) with direct scoring for different reselection lengths for a scoring point not on the pencil beam.

## CHAPTER 6

### THE FEASIBILITY OF TPA AT THE HIP

In chapter four phantom measurements were made using the 203-Hg/141-Ce source. The validity of the technique was established and the variance of aluminum thickness measurements as a function of counting time as estimated (RMS deviation was  $2.36/\sqrt{T}$  for transmission through the steel). In this chapter the variance will be examined in detail using the Monte Carlo model which was described in the previous chapter. Ultimately, the source strength requirements for TPA and the feasibility of TPA will be assessed.

#### 6.1 Variance of TPA

In order to estimate the variance of TPA for geometries (both source and detector collimation and patient) which differ from the experimental situation an expression for the variance must be used. In chapter three the normalized variance was introduced and was given by equation 3.15, reproduced here as equation 6.1

$$V = \sum \left[ (\mu_{(b,E)})^{-1} e^{2Y(E)} \frac{XF(E)}{f(E)} \right] \quad 6.1$$

with the cross-over factor  $XF(E)$  given by equation 3.14, reproduced here as equation 6.2.

$$XF(E) = 1 + \frac{\sum \{ [X(E') + X(E')]^2 f(E') e^{-Y(E')} \}}{f(E) e^{-Y(E)}} \quad 6.2$$

In this instance V was given as the product of the variance and the initial intensity parameter  $I_0'$ , and the intensities at the individual photon energies are given by expression 6.3.

$$I_0(E) = I_0' f(E) \quad 6.3$$

For the phantom measurements, the intensities at the various photon energies are known, and it makes more sense to determine the variance per unit counting time,  $V(T)$ , given as the product of the variance and the counting time. An expression for this is identical to that in equation 6.1 if the intensities at the photon energies are given as

$$I_0(E) = T f(E) \quad 6.4$$

with  $f(E)$  equal to 1021.8, 2620.4 and 2532.6 respectively for Tl X-rays, 145 and 279 keV photons.

If the inverse linear attenuation coefficients,  $\mu$  and the attenuation factors,  $Y(E)$ , are substituted into equation 6.1 for the phantom configuration consisting of 10 cm polyethylene, 0.6 cm aluminum and 0.8 cm steel and the cross-over of 16.75%, the variance per unit counting time is given as  $4.11 \text{ cm}^2$ . The RMS deviation of bone mineral measurements will be given by taking the square root of this, which is  $2.03/\sqrt{T}$  cm bone. This compares favourably with the measured RMS deviation of  $2.36/\sqrt{T}$ . The discrepancy

may be due to the fact that expression 6.1 does not include any systematic effects, and it assumes that the variance in the initial count rates and background is negligible. Nevertheless the agreement supports further use of expression 6.1.

The variance per unit time for more realistic patient geometries can be estimated by determining the appropriate attenuation factors and substituting them into equation 6.1. If this is done for 14 cm polyethylene, 0.6 cm aluminum and 1 cm steel the variance per unit time is given as 70.84 cm and the RMS deviation will be given as  $8.42/\sqrt{T}$  cm aluminum.

It is possible that the variance per unit time can be reduced by adjusting the geometry of the collimators. This will change both the initial intensities at each photon energy and the scatter flux, and hence the cross-over correction, X. If the values of the inverse attenuation coefficients and attenuation factors for the realistic patient geometry are substituted into equation 6.1, an expression for the variance per unit time for arbitrary cross-over factor is given by

$$V(T) = 0.929 + 357.2(X^2 + X) \quad 6.5$$

If the intensities at the three photon energies are equally affected by changes in geometry then the variance per unit

time can be given by

$$V(T) = [ 0.929 + 357.2(X^2 + X) ]/R \quad 6.6$$

where R is the ratio of the intensity at a given geometry to the intensity of the experimental geometry.

The next few sections will be concerned with evaluating the cross-over factor and the intensity ratios for various collimator geometries, and finally with determining the optimal geometry for TPA at the hip.

### 6.2 Intensity ratios of incident beams

The intensity ratio, R, of incident beams for various collimator geometries was determined using a simple Monte Carlo calculation (different from the scatter flux Monte Carlo code). The geometry used for these calculations is shown in figure 6.1 in which the source was a uniform cylinder of length 1 cm (corresponding to the actual active volume of the source) and radius equal to the radius of the source collimator.

Photons were created uniformly within the cylinder and the direction was isotropic within a restricted range of polar angles, from 0 to approximately 12 degrees. The point of intersection of the path of the photon with the exit plane of the source collimator was determined. If this was not within a circle of radius equal to the source collimator the photon was assumed to have been absorbed in the lead

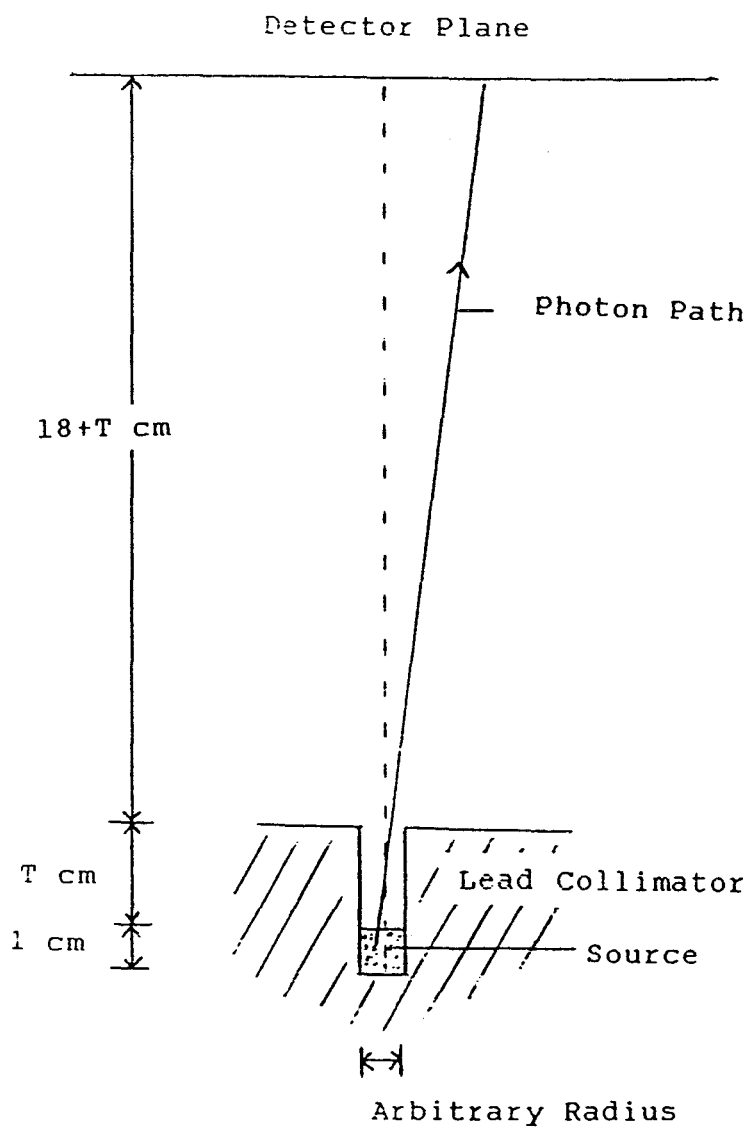


FIGURE 6.1 Schematic diagram of geometry for calculation of intensity ratio for different collimators.

collimator. Self-absorption in the source was not considered because of the different energies of photons.

The flux at the detector plane was scored by determining the point of intersection of the photon path with the plane at the detector and counting the photons which intersect at given radii from the centre of the collimator. The code for this calculation appears in appendix 4.

The results of this calculation for the phantom configuration using 30,000 photons are given in figure 6.2, in which the fraction of the total number of photons leaving the source collimator is given for different radii at the detector plane. It is clear that the beam was not well collimated, and that less than 10% of photons were used in the transmission measurement with a collimator of diameter 8 mm. The other 90% are undesirable both because they contribute to scatter and because they introduce radiation dose for no information gain.

Clearly one would prefer better use of these photons, and in order to maintain spatial resolution of the rectilinear scanner, increasing the radius of the detector collimator is not the ideal solution. To investigate the potential improvement of lengthening the collimators, the calculation was performed for collimators of various radii, each with length 5 cm.

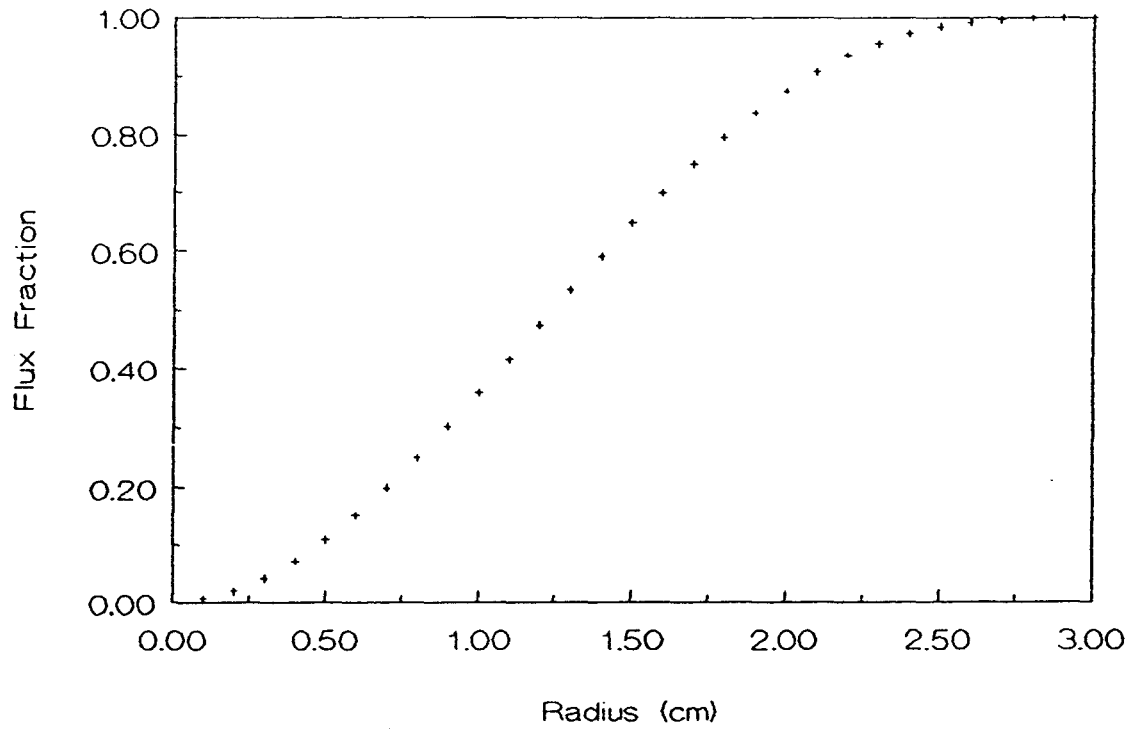


FIGURE 6.2 Plot of fraction of total flux as a function of radius of detector collimator for source collimator used for phantom measurements.

The results are given in figure 6.3 in which the intensity ratio compared with the experimental geometry is given. The collimation is improved with little loss in intensity for source collimators with larger radii. In the next sections the cross-over due to scatter flux will be determined for these geometries, and the results will be combined to determine the variance per unit photon for various geometries.

### 6.3 Monte Carlo Simulation Parameters

The scatter flux was estimated for both the singly and multiply scattered photons using the principles discussed in chapter five; in essence integrating the the probability of scattering to a scoring point multiplied by the photon density at a scattering point, over a scattering volume. For the singly scattered flux, the photon density along a pencil beam is given analytically as an exponentially decreasing function. The integration along the pencil beam was performed numerically by Simpson's rule using 1000 points. The multiply scattered photon density cannot be expressed as a simple analytic expression, so it was sampled using Monte Carlo methods and the scatter flux was estimated using a collision density estimator. The number of photons used for the multiple scatter was 10,000, which was adequate with the variance reduction techniques.

The plane flux per unit photon was estimated at

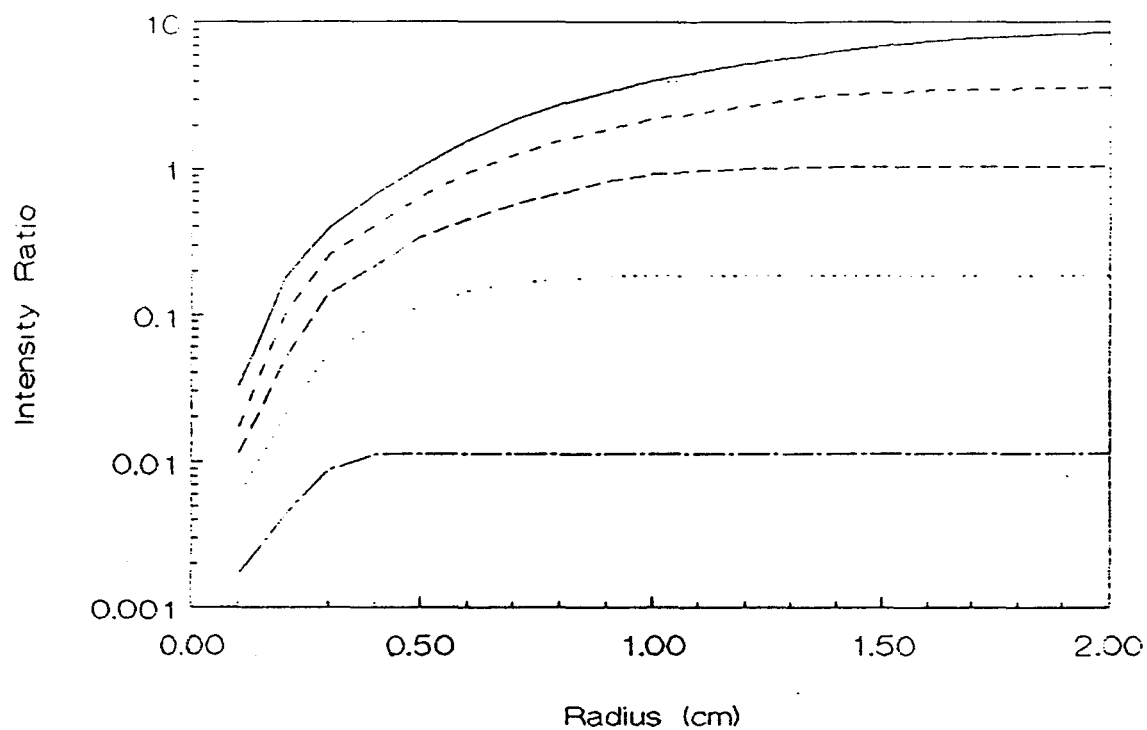


FIGURE 6.3 Plot of intensity ratio as a function of radius of detector collimator for collimators of length 5 cm and radius varying from 2.5 mm (————) to 0.5 mm (—•—•—•—•) in steps of 0.5 mm.

several scoring points along a line perpendicular to the axis of symmetry (the pencil beam) at the plane of the detector. These points were spaced 0.25 cm apart going from the axis to 3 cm from the axis. The flux was estimated as a function of photon energy and polar angle (from axis of symmetry) at each point. The probability for a given photon was added to a bin corresponding to the energy. These bins were 10 keV wide ranging from 0 to 300 keV.

For the multiply scattered photons the flux was also stored as a function of polar angle. It was assumed that the azimuthal angle was not important due to cylindrical symmetry. The cosine of the polar angle was binned with width of 0.02 ranging from 0.8 to 1.0. Angles with cosines less than 0.8 will be greater than 37 degrees, which should be restricted by collimation.

The single scattered flux was estimated as a function of energy only. This was reasonable since the azimuthal angle is directly related to the position of the scoring point on the plane of the detector.

The source to detector distance was limited to approximately 18 cm experimentally. Since commercial DPA devices have fixed minimum distances it seemed reasonable to use 18 cm as a minimum separation for all simulations.

The analysis of the scattered flux generates probabilities of counting scattered photons as either Tl X-

rays or 279 keV gamma rays. This will involve the following tasks: determining the energy response of the NaI detector, convolving the pencil beam profile with the source collimator, and calculating the angular response of the detector collimator.

#### 6.4 Energy response of the 5.08 cm NaI detector

The response of a NaI detector to a photon of a given energy is described in detail in several sources such as Knoll (1979). The energy response is the pulse height spectrum generated by deposition of energy in the crystal. For photon energies below 300 keV the important features are the photopeak which is due to photoelectric absorption, a Compton continuum due to scatter in the crystal and possibly an iodine escape peak which is due to iodine X-rays leaving the crystal following a photoelectric absorption. Generally the photopeak is used to count the number of photons of a given energy.

In this section a different type of energy response is discussed. Since the energies of the transmitted photons are well defined, the photopeaks corresponding to Tl X-rays and 279 keV photons are counted using single channel analyzers (SCA). Scattered photons will add spurious counts in these windows when they give a pulse with height which is within the range of pulse heights accepted by the SCA. This can occur when the photopeak of the scattered photon

overlaps the window, or when a photon has energy greater than that of the window and deposits only a fraction of its energy in the detector. The response of interest is the probability that a photon of a given energy will appear in either of the two photopeak windows.

This response was determined empirically by obtaining the spectra of several different isotopes under conditions identical to those used for phantom measurements. The isotopes and the photon energies are listed in table 6.1. For each photon energy the total counts,  $C_t$ , and the overlap into a given SCA window,  $O(w)$ , were determined. The efficiency of the 5.08 cm NaI crystal,  $\epsilon$ , was calculated using linear attenuation coefficients for NaI(Tl) from Mannhart (1976). The energy response, or the probability that a photon of a given energy will be counted by a given SCA was given by the following expression.

$$P(w) = \epsilon O(w)/C_t \quad 6.7$$

This is plotted for the Tl X-ray window in figure 6.4. The response was fitted using least squares to the sum of two functions. The first was a fourth order polynomial for energies greater than 80 keV, and 0 for energies less than 80 keV. This corresponds to Compton scattered higher energy photons. The second was  $\text{erf}(|E_0 - E|)$  which corresponded to the overlap of a Gaussian into the window of the SCA. Only the second function was used to fit the data for the 279 keV

Table 6.1 Isotopes used to determine detector response

<u>Isotope</u>	<u>Photon Energies (keV)</u>
241-Am	60
153-Gd	103
57-Co	122
143-Ce	145
111-In	173
	247
203-Hg	279

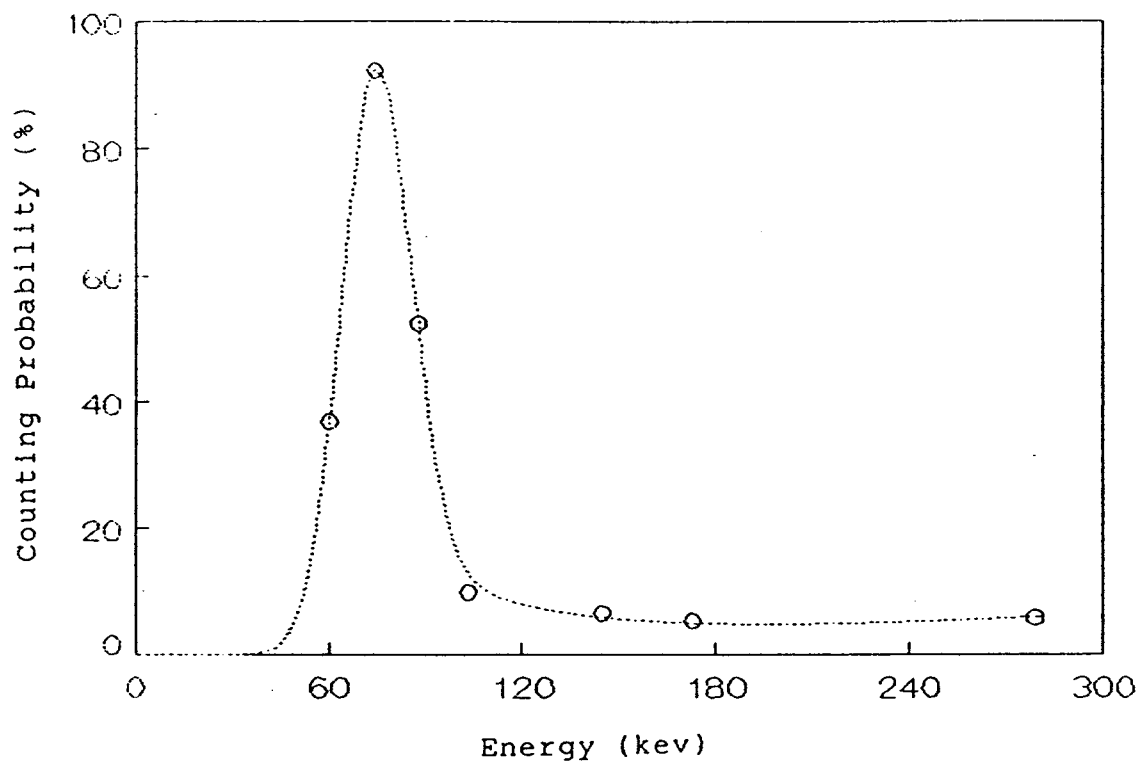


FIGURE 6.4 Plot of probability of counting pulse in Tl X-ray window as a function of photon energy including experimentally measured values (O) and fitted function (.....).

window.

Since the Monte Carlo scatter flux was determined with energy bins of width 10 keV, the mean response over 10 keV intervals was determined for both SCA windows. These are given in figures 6.5 and 6.6 and were used to calculate the scatter count rate in a window from the flux as a function of energy. Further analysis of the Monte Carlo calculations is described in the next sections.

### 6.5 Scatter Flux Estimation

The scatter flux was determined for both singly and multiply scattered photons using the parameters indicated in section 6.3. The energy response was incorporated to yield scatter flux as a function of radius, and for multiply scattered photons as a function of photon direction. The analysis of the data for single and multiple scattering differs from this point.

#### 6.5.1 Single Scatter Flux

The energy response corrected single scatter flux was determined for both the 279 keV photons and the Tl X-ray photons for all phantom configurations. A typical example for the Tl X-rays is shown in figure 6.7 in which the flux probability at the scoring points was used to generate the flux probability for the entire radial function using a cubic spline. Similar data are shown in figure 6.8 for 279 keV photons in which the responses of both SCA windows are

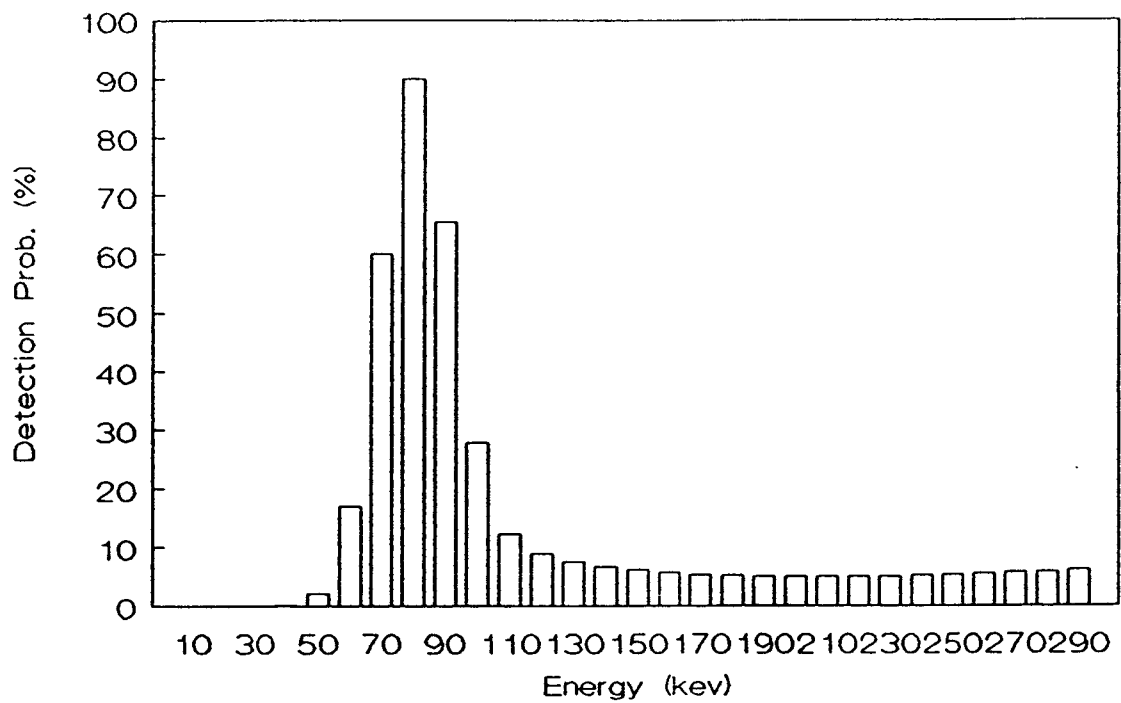


FIGURE 6.5 Plot of mean detector response for 10 keV intervals as a function of photon energy for Tl X-ray window.

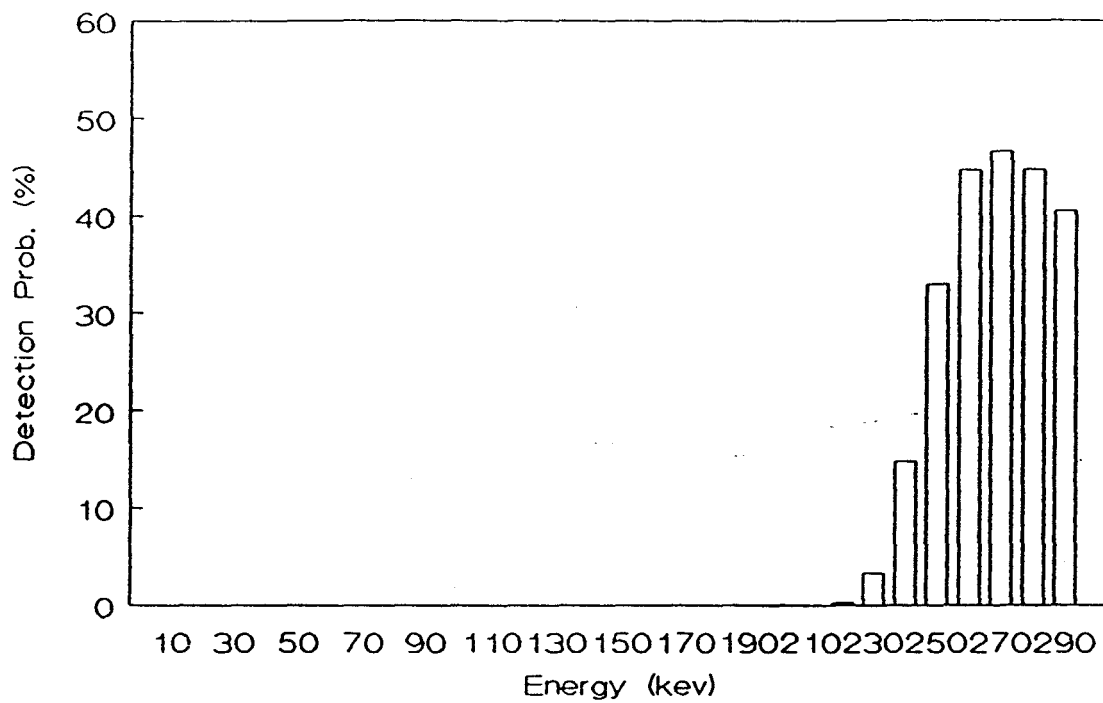


FIGURE 6.6 Plot of mean detector response for 10 kev intervals as a function of photon energy for 279 kev photon window.

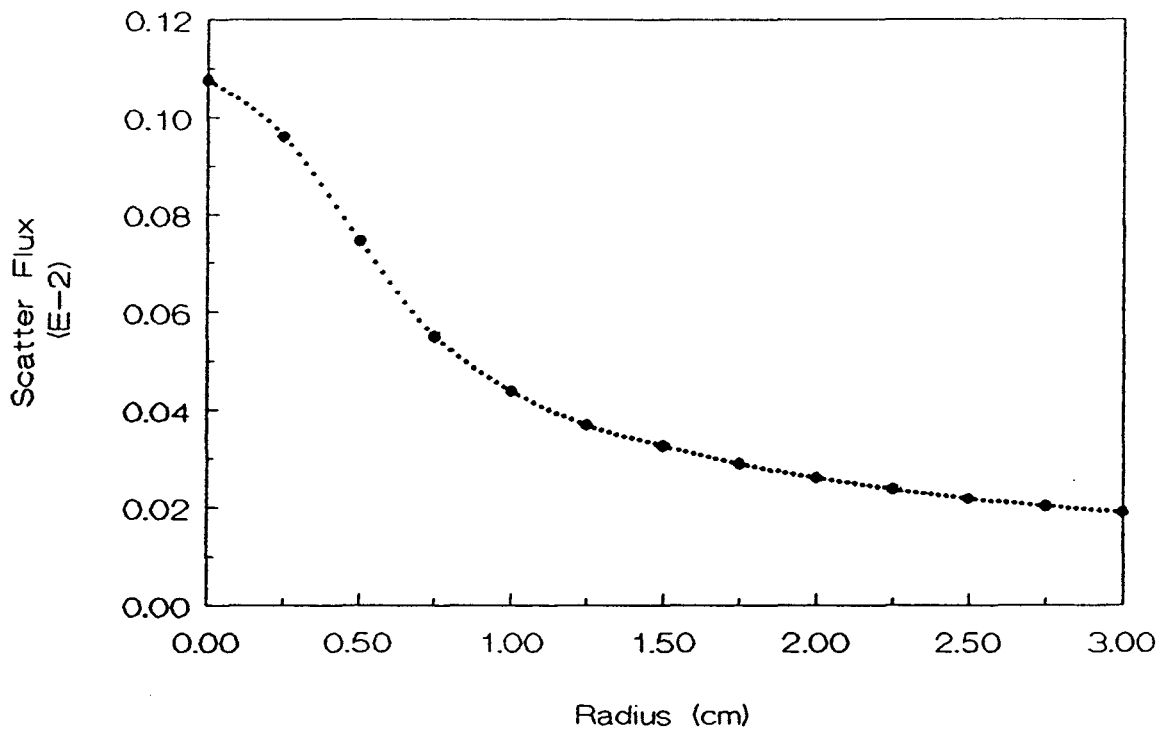


FIGURE 6.7 Probability of single scatter from Tl X-rays within the Tl X-ray window. The object is 9.7 cm polyethylene, 0.6 cm aluminum irradiated with a pencil beam. The data is given for the individual scoring points (●) and as a fitted cubic spline (.....).

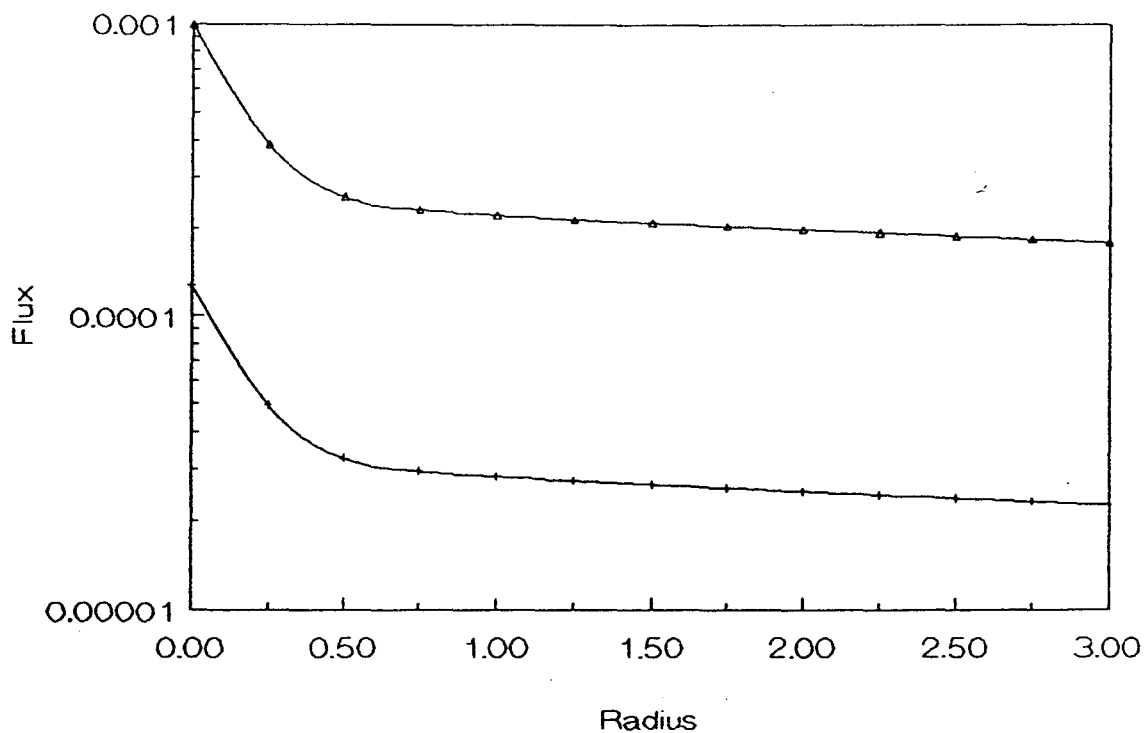


FIGURE 6.8 Probability of single scatter from 279 kev photons within the 279 kev window ( $\Delta$ ) and the Tl X-ray window (+). The object is 9.7 cm polyethylene, 0.6 cm aluminum irradiated with a pencil beam. The data is given for the individual scoring points and as a fitted cubic spline.

shown.

Examination of figure 6.8 reveals that the response of the Tl X-ray window is exactly 12.6% of the 279 kev window (the detector response), and there is in fact no cross-over of 279 kev photons due to scatter in the phantom. This must be expected since all singly scattered photons at small radii will necessarily have energies very near to the initial energy since the scatter angle is also small. Similarly the Tl X-rays which scatter through small angles will not differ in energy from the original energies.

This being the case, the small angle singly scattered photons will be indistinguishable from the transmitted photons and should not be used for calculation of scatter flux. In reality the linear attenuation coefficients were determined experimentally, so that these singly scattered photons would have counted as transmitted photons in the first instance. All further analysis will concern the multiply scattered flux.

#### 6.5.2 Multiply Scattered Flux

The energy response corrected multiply scattered flux probability is a function of both radius and direction of the photon. This was determined for both the 279 kev photons and the Tl X-rays for all phantom configurations. The result of importance was the scatter into the Tl X-ray window and analysis was restricted to such. Typical examples

of the flux probability for 10,000 photons are plotted in figure 6.9 for both 279 keV photons and Tl X-rays.

Examination of figure 6.9 reveals that the probability decreases with radius for  $\cos(\theta)=1$  while it increases for all other values. This trend was observed for all phantom configurations. It was possible to parameterize the flux probability by using two different equations. For  $\cos(\theta)=1$  the parameterization was a function of only the radius, with a quadratic giving reasonably good fits. A typical quadratic fit is shown in figure 6.10. For the rest of the data the parameterization was a function of both the radius and  $\cos(\theta)$ . It was determined that a function of the form

$$P(r, \cos(\theta)) = (1+kr)P(\cos(\theta)) \quad 6.8$$

where  $P(\cos(\theta))$  was a second order polynomial gave good fits with typical reduced Chi-squared values of 1.5-2.0.

The scatter flux probability for a given source collimator geometry was given by convolution of the pencil beam flux probability with the beam profile expected from the source collimator. Since the source collimator was cylindrical it was expected that the beam profile would consist of a uniform circle with radius equal to the collimator radius and that the convolution would itself be circularly symmetric. It was possible to calculate the radial portion of the convolution using only the radial

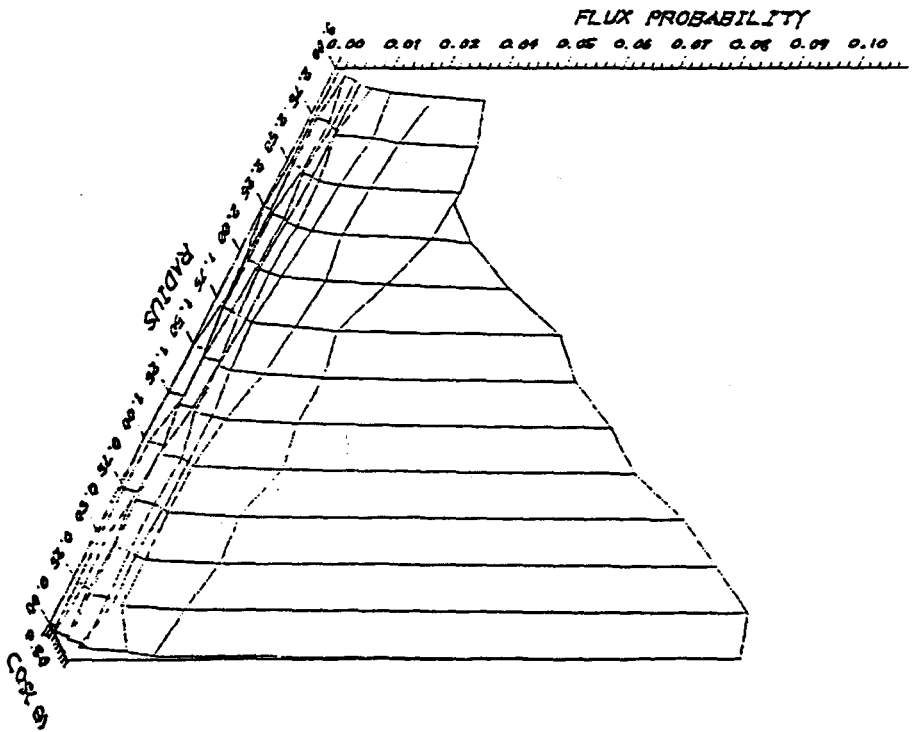
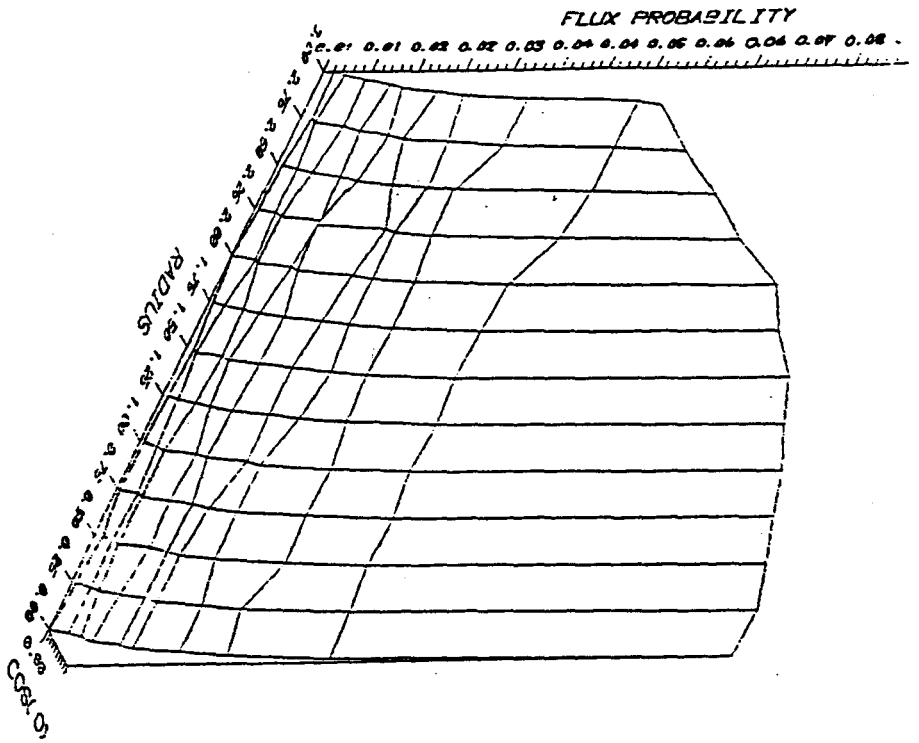


FIGURE 6.9 Multiple scatter window probability for Tl  
 X-ray window for 9.7 cm polyethylene, 0.6 cm  
 aluminum as a function of radius from the pencil beam and  
 cosine of polar angle. Plots are given for 279 keV photons  
 (left) and Tl X-rays (right).

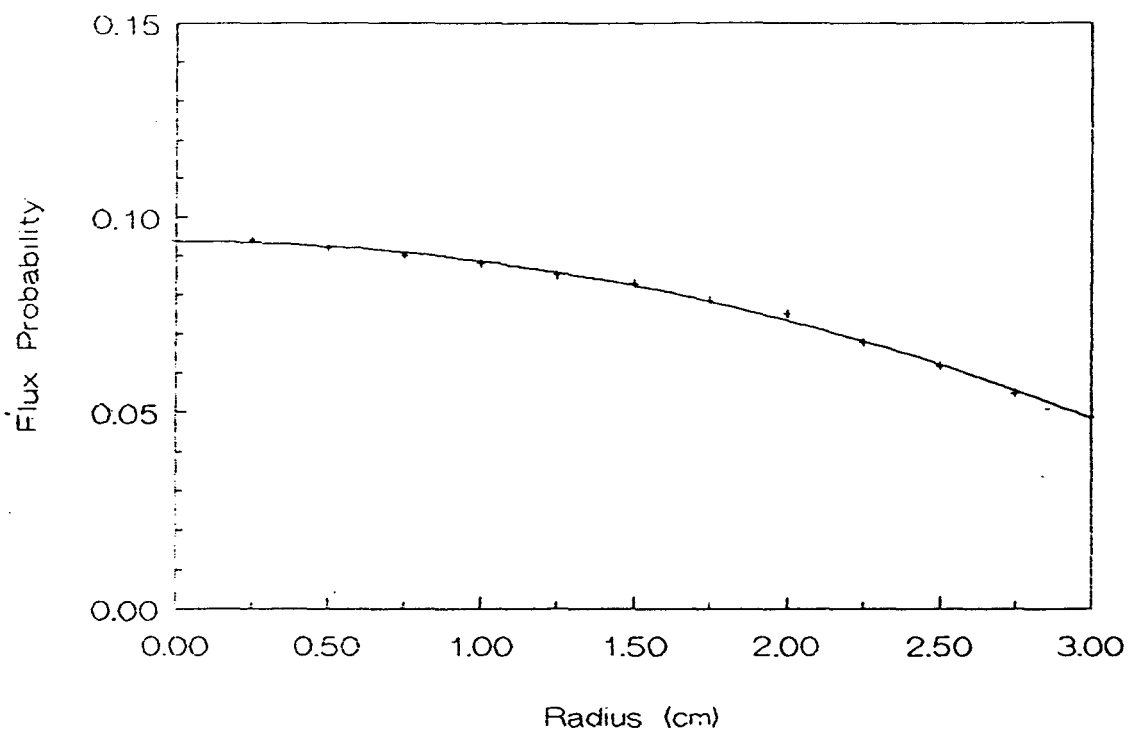


FIGURE 6.10 Multiple scatter window probability for Tl X-ray window for 279 kev photons as a function of radius for cosine of polar angle of photon direction of 1. These are typical data obtained at the scoring points (+) and with the quadratic least squares fit ( ——— ).

portions of the pencil beam flux probability and beam profile. This is described in detail in appendix five.

The result of the convolution was a set of radial functions of the scatter flux probability at the plane of the entrance of the detector collimator, each appropriate for a single photon polar angle. The flux probability at the detector will be due to photons which have radii less than that of the collimator both at the entrance and the exit. The flux entering the collimator could be calculated by integrating the scatter flux probability over the area of the entrance of the detector collimator, however some of these would interact with the collimator wall.

The stipulation that the photon reach the detector was incorporated by assuming that the multiply scattered photon direction would display azimuthal symmetry. A photon at a given radius would give rise to a cone of photons with equal polar angle. The fraction of these which reach the detector was calculated using a method described in appendix six, the geometric efficiency of the collimator.

The scatter flux probability was corrected for angular response and then integrated over the area of the collimator to yield the net scatter flux probability. This is expressed as the number of photons counted in the Tl X-ray window for each photon emitted from the source.

The total scatter flux into the Tl X-ray window is

the sum of the scatter from the 279 keV photons and the Tl X-rays. The unattenuated count rates in these windows were measured in chapter four, and combined with the photopeak efficiency calculated in section 6.4 the ratio of Tl X-rays to 279 keV photons was determined to be approximately 0.22. The total scatter flux per 279 keV photon was calculated by summing the individual scatters using the weights 0.22 and 1 for Tl X-rays and 279 keV photons. The precision of this procedure was estimated to be 5% based upon repeated simulations for selected phantom configurations.

The calculation of scatter flux probabilities made it possible to compare the Monte Carlo results with the phantom results. The scatter flux for the phantom measurements was determined by subtracting from the measured count rate a count rate calculated as the product of the initial count rate and the linear attenuation coefficients. The ratio of the scatter flux at a given configuration to that with only polyethylene was calculated and compared with the ratio determined from the Monte Carlo scatter flux probability. The ratios are given in table 6.2 in which the phantom measurements and the Monte Carlo results agree.

This agreement gives confidence in further analysis which involved calculating the flux probability for the phantom configuration and source detector collimator geometries indicated in section 6.2. These were used to

Table 6.2 Scatter flux ratios for some phantom configurations

<u>Phantom Configuration</u>	<u>Scatter Flux Ratio</u>	
	<u>Measured</u>	<u>Monte Carlo</u>
.314 cm aluminum	1.038	.987 $\pm$ .074
.974 cm aluminum	1.154	1.068 $\pm$ .080
.314 cm aluminum .794 cm steel	.524	.446 $\pm$ .033
.974 cm aluminum .794 cm steel	.498	.407 $\pm$ .031

calculate the cross-over due to scatter, which will be described in the next section.

#### 6.6 Cross-over and Variance for Varying Geometry

The cross-over due to scatter will be given by the scatter flux per photon divided by the transmitted flux per photon calculated for each geometry. The scatter flux was calculated for 10000 photons as described in the previous section. Rather than finding the scatter flux per photon the scatter flux was normalized to the flux for the phantom with 9.7 cm polyethylene. This was done by multiplying the measured phantom scatter flux by the ratio of the scatter flux for a given configuration divided by that for the phantom from Monte Carlo simulation, and multiplying the result by the ratio of total beam intensity for the configuration and the phantom (given as the integral of the intensity ratio from figure 6.3). This was done to eliminate any difficulties arising from assumptions about the fraction of the beam hitting the detector in the phantom measurements.

The transmitted flux was normalized to the phantom flux by dividing the exponential of the attenuation factor,  $\exp(-Y(Tl \text{ X-ray}))$ , for the Monte Carlo configuration by that for the phantom. The result was then multiplied by the product of the transmitted flux for the phantom measurements and the intensity ratio (taken from figure 6.3).

The cross-over due to scatter was determined by dividing the scatter flux by the transmitted flux for the configurations discussed earlier. The results appear in figure 6.11 and can now be combined with the intensity ratio 3 to determine the variance per unit counting time using equation 6.6. However the cross-over appearing in equation 6.6 refers to total cross-over and not just scatter in the phantom. The scatter cross-over was added to .1266, the cross-over from the detector response to give the total cross-over and this was used with the intensity ratio from figure 6.3 to find the variance per unit counting time for various configurations. This is plotted in figure 6.12.

It is clear from figure 6.12 that the variance decreases with increasing radius of source collimator, due primarily to increasing the intensity ratio. The variance also decreases with increasing radius of detector collimator. Although the cross-over increases with increasing detector collimator radius, the intensity ratio affects the variance more strongly than the cross-over. Moreover the effect of decreasing cross-over is limited by the 12.66% cross-over in the detector itself.

The best choice of collimators would be the 2.5 mm source collimator with a large detector collimator. Obviously one is restricted in the choice of detector collimator by resolution of the scanner and should remain

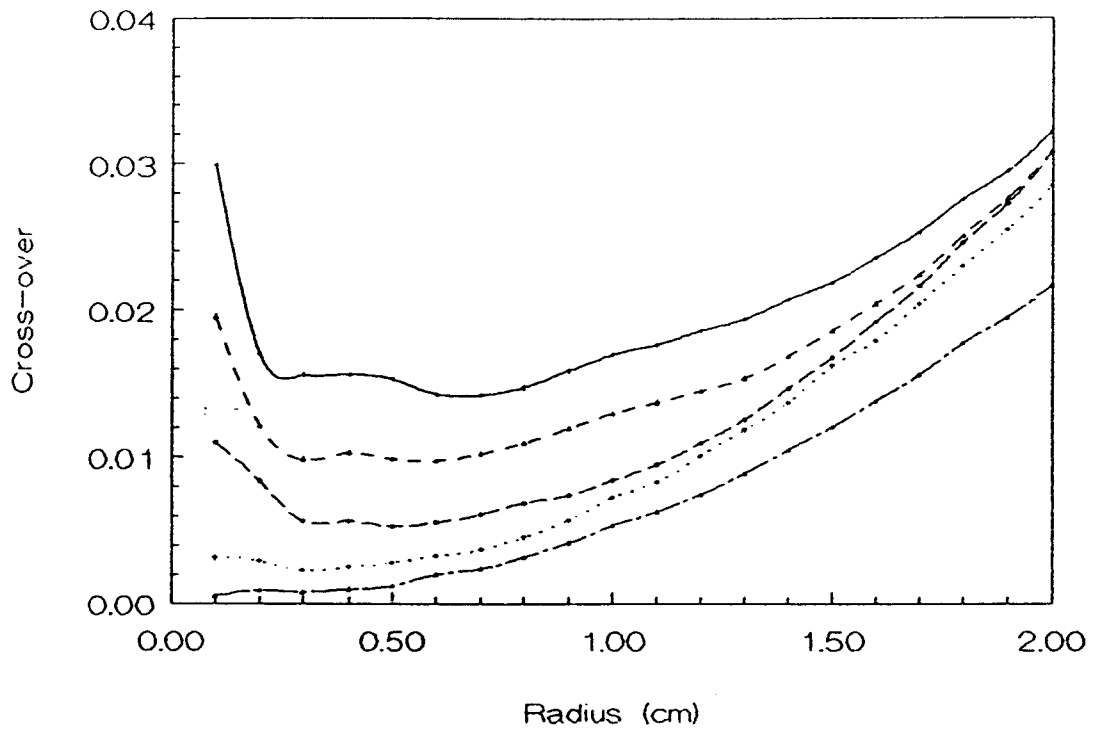


FIGURE 6.11 Plot of cross-over due to scatter as a function of radius of detector collimator for collimators of length 5 cm and radius varying from 2.5 mm (————) to 0.5 mm (—•—•—) in steps of 0.5 mm.

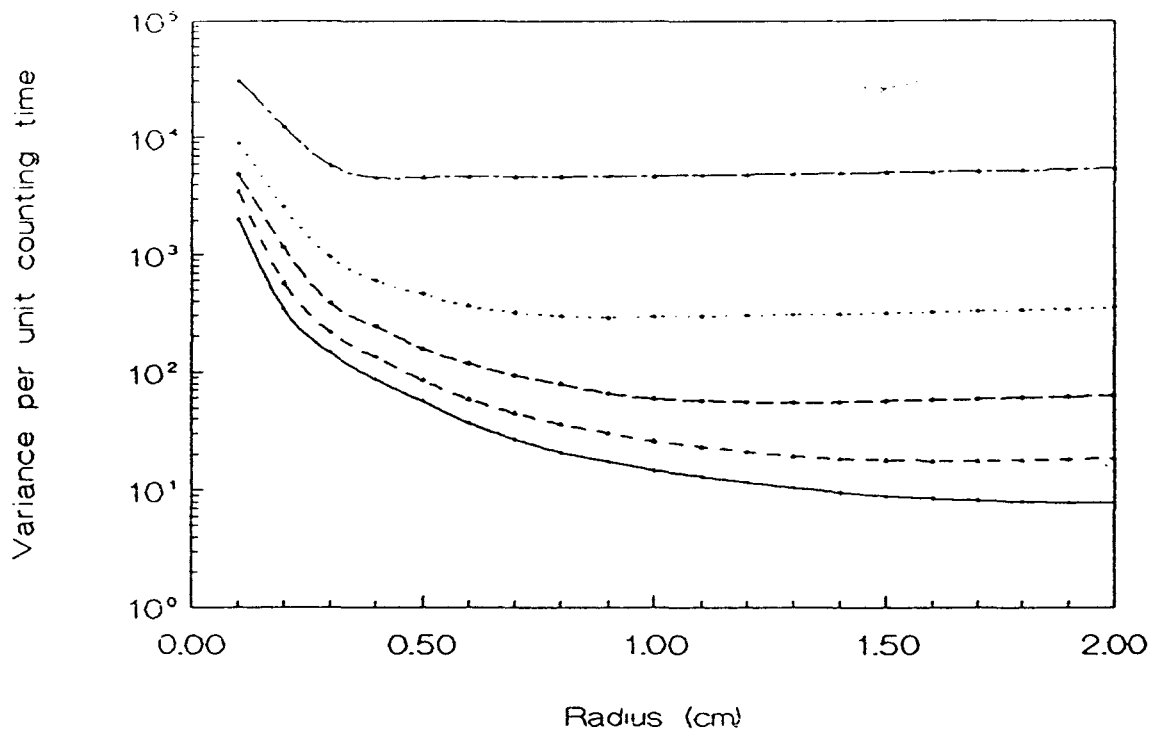


FIGURE 6.12 Plot of variance per unit counting time as a function of radius of detector collimator for collimators of length 5 cm and radius varying from 2.5 mm (————) to 0.5 mm (—•—•—) in steps of 0.5 mm.

with radii below 5mm, a value not very different from the phantom measurement configuration. To choose the radius between 4 mm and 5 mm would give variance between 87 and 56 cm per second counting time. The implications of this will be discussed in the next section.

#### 6.7 Source Strength Requirements and Feasibility of TPA

The results of the Monte Carlo calculations suggest that the lowest variance per unit time which can be achieved using reasonable geometry is  $56 \text{ cm}^2$ . This of course is the variance per pixel, and the variance over the entire bone mineral image will be given by  $56/N \text{ cm}^2$  where  $N$  is the number of pixels with bone mineral. This number will be reduced since the variance over regions without steel is considerably lower (2 orders of magnitude) than with steel, and most of the noise will be over the prosthesis. Using a collimator radius of between 4 and 5 mm one can expect  $N$  to be of the order 20 to 25. This will lead to variance for average thickness of 2.25 cm per unit counting time; that is, a precision of  $1.5/\sqrt{T} \text{ cm}$  where  $T$  is the counting time.

The source strength requirement will depend upon the precision required to demonstrate clinically relevant changes in bone mineral. Unfortunately since these measurements have not been made before, that figure is not known. However based upon normal bone loss of 1-2%, a precision of 3% would be a minimum requirement and precision

of 1% would probably be ideal.

If typical bone mineral areal densities are between 0.6 and 1.0 g/cm<sup>2</sup> then the corresponding thicknesses of aluminum are between .20 and .37 cm. Choosing a midrange thickness of .3 cm aluminum, a precision of 3% is in fact .009 cm aluminum while 1% is .003 cm aluminum. The counting time per pixel to achieve these results will be 7.7 hours and 69 hours respectively.

These counting times are clearly unreasonable. It is conceivable that counting times as long as one hour may be feasible. This will include counting regions away from the prosthesis. It is likely that some form of increasing the counting time for regions including the prosthesis will be necessary and it may mean that the counting time will be restricted almost entirely to the prosthesis. If there are 25 pixels, this will allow counting of approximately 2 minutes per pixel. In order to achieve the same number of counts in the shorter time the source must be approximately 231 times stronger.

The major problem involved in 'boosting' the source activity is that the thermal neutron cross-section of the <sup>202</sup>Hg is low, and the source saturates at its present activity. If a more massive source were used, it would require almost 200 g of Hg<sub>2</sub>F<sub>8</sub> to achieve the desired activity. That would involve considerable self absorption of

the Tl X-rays, which would require a further increase in source strength to obtain a proportionate increase in photon flux. Even if a higher neutron flux were available, an increase of 200 times is required to yield 3% precision.

Ultimately it appears that the cross-over dooms the TPA by increasing the variance. It is unlikely that the precision of the technique can be improved by any means other than using a different source so that TPA with a Hg-Ce source is not a feasible approach to measuring bone mineral about a hip prosthesis.

## CHAPTER 7

### CONCLUSION

#### 7.1 Bone Mineral Absorptiometry at the Spine

Bone mineral absorptiometry at the spine involves measuring the transmission of photons through a three component system including lean, fat and bone mineral. The present commercially available dual photon absorptiometry uses two photon energies to separate bone mineral from a composite soft tissue, assuming a two component system.

The error due to inhomogeneous distributions of fat was estimated by measuring the in-vivo distribution of fat in normal populations using CT scans through the lumbar vertebrae. These results were used in a model which predicted the error due to fat inhomogeneities which was validated by phantom results.

Projected errors were found to have a median value of 8%, and could be either positive or negative. These must be considered a source of variance in the dual photon technique which reduces the sensitivity of such measurements.

The predicted errors are in agreement with Roos et al (1980) who measured the difference between dual photon bone mineral measurements for vertebrae from cadavers both

in situ and excised. More recently Gotfredsen et al (1988) found errors of 10.3% and Eriksson et al (1988) found errors of 6 - 16% also using cadavers. Tothill et al (1987) used CT scans in a method similar to this study to predict errors of 8 - 20%. The inescapable conclusion is that large errors are introduced by fat inhomogeneities. If these errors could be removed, then the discrimination of osteopenic populations from normal populations might be improved.

Triple photon absorptiometry was analyzed as a possible solution for the errors introduced by fat. This seems to be an obvious approach, to use three photon energies to solve a three component system. However, the differences between the attenuation properties of the three components was small. In order for TPA to be viable the attenuation of the photons must be measured extremely accurately with photon energies that give the greatest discrimination of tissue types.

The analysis consisted of determining the optimum set of photon energies by calculating a normalized variance for the bone mineral equivalent thickness for typical patient parameters. This was found to depend strongly upon the cross-over of higher energy photons to lower energy channels and on the set of photon energies. The variance of the bone mineral equivalent using the optimum set was calculated by simulating the TPA measurement including only

statistical noise in the data and eliminating any systematic errors which may occur.

The radiation dose required for TPA measurements with precision similar to present DPA measurements was found to be 3,000 higher than that for DPA. This estimate does not include systematic errors which will exacerbate the situation. If TPA were implemented the increase in accuracy would serve to reduce the variance of the bone mineral measurements. This includes both the normal biological variation of bone mineral as well as the variance due to the errors. The increased radiation dose required to perform TPA will not justify the increase in accuracy.

These results are in contrast to Jonson, Roos and Hansson (1988) who have suggested that TPA may be viable using a combination of  $^{153}\text{Gd}$  and  $^{241}\text{Am}$ . Close examination of their data indicates that the variance to dose ratio is similar to that calculated in chapter three. In fact they concluded that the precision of TPA is not sufficient for clinical purposes.

The linear attenuation coefficient for a third material can be expressed as a linear combination of those for two other materials. These relations do not change much with energy. For TPA the linear combinations are sufficiently similar over the energy range of diagnostic radiology that large numbers of photons must be transmitted

in order to separate the three materials. For DPA fat introduces only small errors (.05 cm bone per cm fat) however since there is considerably more fat than bone mineral the errors are an appreciable fraction of the bone mineral.

### 7.2 TPA at the Hip Prosthesis

TPA at the hip prosthesis involves measuring the bone mineral surrounding the shaft of the femoral component of the hip prosthesis. This is accomplished by decomposing the three phases, metal, bone mineral and soft tissue by using three different photon energies.

An isotopic source consisting of  $^{203}\text{Hg}$  and  $^{143}\text{Ce}$  was produced in the reactor and phantom measurements demonstrated that TPA would work albeit with high variance. Monte Carlo calculations to determine the best precision possible using the present source showed the source to be unfeasible due to extremely long counting times required.

The largest source of variance in the measurements was the cross-over correction for the 279 keV photons in the Tl X-ray window for the  $^{203}\text{Hg}$  source. The transmission flux rates are sufficiently low that the cross-over can be several times the Tl X-ray counts, with the result that the variance of the attenuation factor may be several times larger than the measurement itself.

Unlike the case of TPA at the lumbar spine in which

the differences in attenuation coefficients for the three materials was the limiting factor, in this case the limiting factor is the cross-over in the detector itself. Changing to a detector with better energy resolution, such as a high purity germanium detector, HPGe, does not improve the situation appreciably. Preliminary measurements of the spectrum of  $^{203}\text{Hg}$  using a HPGe indicated that the cross-over in the detector is approximately 3%. This will only reduce counting times by one half. The only solution to improve the variance is to eliminate the cross-over, since changes in geometry have little effect.

If a third isotope such as  $^{109}\text{Cd}$  with an 88 keV photon were used, and the transmission was measured separately for the three photon energies the cross-over would be eliminated. The development of such a source may form the basis for further work in this area.

### 7.3 TPA: a Final Word

Triple photon absorptiometry is an extension of dual photon absorptiometry and any dual energy technique which decomposes a complex combination of materials into two phases. Pundits argued that two phases were sufficient for any number of materials, and in fact that no more than two phases can be decomposed from a mixture of materials.

In this work two different combinations were examined. In the first, the effective atomic numbers of the

constituent materials did not differ greatly, while in the second the steel was considerably different from the other two components. The results suggest that three components can indeed be decomposed using three photon energies (although the variance was high due to cross-over). The difficulty of making these measurements increases as the differences between the effective atomic numbers of the constituents become smaller. The possibility of decomposing three constituents depends upon what are second order terms in the cross-sections, such as atomic scattering factors for incoherent scattering, and coherent scattering (an interaction of little impact in broad beam measurements in planar radiological imaging).

Perhaps the notion that TPA is not possible arose from such modalities as dual energy CT or digital radiology where it is indeed unviable. However it is not correct to assume that under different geometry with materials of sufficient difference that TPA is not possible.

## BIBLIOGRAPHY

- Alvarez RE and Macovski A. 1976. Energy selective reconstructions in X-ray computerized tomography. *Phys Med Biol* 21 733-744.
- Avrin DE, Macovski A and Zata LM. 1978. Clinical application of Compton and photoelectric reconstruction in computerized tomography: preliminary results. *Inves Radiol* 13 217-222.
- Baran DT, Kelly AM, Karellas A, Gronet M, Price M, Leakey D, Stevenson S and McSherry B. 1988. Ultrasound attenuation of the os calcis in women with osteoporosis and hip fracture. *Calcif Tissue Int* 43 138-142.
- Bechtol CO. 1983. Total hip implant: a biomechanical device. In ed Rubin LR. *Biomaterials in reconstructive surgery*. CV Mosby. St Louis.
- Bevington PR. 1969. Data reduction and error analysis for the physical sciences. McGraw-Hill. New York.
- Bhaskar BK. 1984. Study of a new source for dual photon absorptiometry of the lumbar spine. M. Eng Thesis. McMaster University.
- Billingsley FC. 1975. Noise considerations in digital image processing hardware. in *Picture processing and digital filtering*. ed Huang TS. Springer-Verlag. New York.
- Bohr H and Schaadt O. 1983. Bone mineral content of femoral bone and the lumbar spine measured in women with fracture of the femoral neck by dual photon absorptiometry. *Clin Orth* 179 240-245.
- Boone JM, Seibert JA. 1988. Monte Carlo simulation of the scattered radiation distribution in diagnostic radiology. *Med Phys* 15 713-720.

- Bradley DA, Chong CS and Ghose AM. 1986. Photon absorptiometric studies of elements, mixtures and substances of biomedical interest. *Phys Med Biol* 31 267-273.
- Cameron JR and Sorenson J. 1963. Measurement of bone mineral in vivo: an improved method. *Science* 142 230.
- Cann CE and Genant HK. 1980. Precise measurement of vertebral mineral content using computed tomography. *J Comput Assist Tomogr* 4 493-500.
- Carlsson AS and Gentz CF. 1980. Mechanical loosening to the femoral head prosthesis in the Charnley total hip arthroplasty. *Clin Orthop* 147 262.
- Carter LL, Cashwell ED. 1975. Particle-Transport simulation with the Monte Carlo method. USERDA TID-26607.
- Chan HP, Doi K. 1982. The validity of Monte Carlo simulation in studies of scattered radiation in diagnostic radiology. *Phys Med Biol* 28 109-129.
- Chan HP, Doi K. 1986. Some properties of photon scattering in water phantoms in diagnostic radiology. *Med Phys* 13 824-830.
- Cheney W, Kincaid D. 1985. Numerical mathematics and computing. Brooks publishing. Monterey Calif.
- Cohn SH. 1981. Total body neutron activation. in ed Cohn SH. Non-invasive measurements of bone mass and their clinical application. CRC Press. Florida.
- Dunn WL, Wahner H, and Riggs BL. 1980. Measurement of bone mineral content in human vertebrae and hip by dual photon absorptiometry. *Radiology* 136 485-487.
- Eriksson S, Isberg B and Lindgren U. 1988. Vertebral bone mineral measurement using dual photon absorptiometry and computed tomography. *Acta Radiol* 29 89-94.
- Evans RD. 1955. *The Atomic Nucleus*. McGraw-Hill. New York.
- Fishman EK, Magid D, Robertson DD et al. 1986. Metallic hip implants: ct with multiplanar reconstruction. *Radiology* 160 675-681.
- Freiberger RH. 1986. Evaluation of hip prostheses by imaging methods. *Sem Roentg* 21 20-28.

- Garnett ES, Kennet TJ, Kenyon DB, Webber CE. 1973. A photon scattering technique for the measurement of absolute bone density in man. *Radiology* 106 209-212.
- Goodwin PN. 1987. Methodologies for the measurement of bone density and their precision and accuracy. *Semin Nucl Med* 17 293-304.
- Gotfredsen A, Podenphant J, Norgaard H et al. 1988. Accuracy of lumbar spine bone mineral content by dual photon absorptiometry. *J Nucl Med* 29 248-254.
- Haberman ET. 1986. Total joint replacement: an overview. *Sem Roentg* 21 7-19.
- Hawkes DJ, Jackson DF and Parker PP. 1986. Tissue analysis by dual-energy computed tomography. *Br J Rad* 59 537-542.
- Hazan G, Leichter I, Loewinger E, Weinreb A, Robin GC. 1977. The early detection of osteoporosis by Compton gamma ray spectroscopy. *Phys Med Biol* 22 1073.
- Hobble RK. 1987. Interaction of photons and charged particles with matter. Williams LE ed. *Nuclear Medical Physics Volume 1*. CRC Press. Boca Raton Florida.
- Houston JC, Joiner CL, Trounce JR. 1975. *A Short Textbook of Medicine*. English University Press, London.
- Howmedica Inc. 1979. *Vitallium Technical Monograph*.
- Hubbell JH. 1982. Photon mass attenuation and energy absorption coefficients from 1 keV to 20 MeV. *Int J Appl Radiat Isot* 33 1269-1290.
- Hubbell JH, Veigele WJ, Briggs et al. 1975. Atomic form factors, incoherent scatter functions and photon scatter cross-sections. *J Phys Chem Ref Data* 4 471-538.
- Huddleston AL, Bhaduri D. 1979. Compton scatter densitometry in cancellous bone. *Phys Med Biol* 24 310-318.
- Jackson DF and Hawkes DJ. 1983. Energy dependence in the spectral factor approach to computed tomography. *Phys Med Biol* 28 288-293.

- Jonson R, Roos B and Hansson T. 1986 Bone mineral measurement with a continuous roentgen ray spectrum and a germanium detector. Acta Radiol Diagn 27 105-109.
- Jonson R, Roos B and Hansson T. 1988. Triple photon absorptiometry in the measurement of bone mineral. Acta Radiol 29 461-464.
- Joyet G, Baudraz A and Joyet ML. 1974. Determination of the electronic density and the average atomic number of tissues in man by gamma ray attenuation. Experientia 30 1338-1341.
- Kallender W. 1981. Monte Carlo calculations of x-ray scatter data for diagnostic radiology. Phys Med Biol 26 835-849.
- Kalos MH. 1963. On the estimation of flux at a point by Monte Carlo. Nucl Sci Eng 16 111-117.
- Karellas A, Leichter I, Craven JD and Greenfiels MA. 1983. Characterization of tissue via coherent to compton scattering ratio: sensitivity conditions. Med Phys 10 605-609.
- Karjalainen P. 1973. A method for determination of the mineral content of distal radius with gamma ray attenuation. Annal of Clin Res 5 321-237.
- Kerr SA, Kouris K, Webber CE, Kennet TJ. 1980. Coherent Scattering and the assessment of mineral concentration in trabecular bone. Phys Med Biol 25 1037-1047.
- Knoll GF. 1979. Radiation Detection and Measurement. John Wiley and sons. New York.
- Krolner B and Pors Nielsen S. 1980. Measurement of bone mineral content (BMD) of the lumbar spine, 1. Theory and application of a new two-dimensional dual-photon attenuation method. Scand J Clin Lab Invest 40 653-663.
- Laval-Jeantet AM, Roger B, Bouysse S et al. 1986. Influence of vertebral fat content on quantitative CT density. Radiology 159 463-466.
- Lederer CM, Hollander JM, and Perlman I. 1968. Table of Isotopes 6th edition. John Wiley and Sons. New York

- Lehmann LA, Alvarez RE, Macovski A and Brody WR. 1981. Generalized image combinations in dual kvp digital radiography. *Med Phys* 8 659-667.
- Lewis TG. 1975. Distribution sampling for computer simulation. DC Heath. Lexington Mass.
- Lewis TG, Payne WH. 1973. Generalized feedback shift register pseudorandom number generator. *J Assoc Comp Mach* 20 456-468.
- Lindsay R, Anderson JB. 1978. Radiological determination of changes in bone mineral content. *Radiography* 44 295-314.
- Mannhart W and Vonach H. 1976. Gamma-ray absorption coefficients for NaI(Tl). *Nucl Inst Meth* 134 347-351.
- Matthews JH. 1987. Numerical Methods. Prentice Hall. New Jersey.
- Mazess RB. 1979. Measurement of Skeletal Status by Noninvasive Methods. *Calc Tiss Int* 28 89-92.
- Mazess RB. 1981. Noninvasive measurement of local bone in osteoporosis In: *Osteoporosis: Recent Advances in Pathogenesis and Treatment*. Editor: H deLuca. University Park Press, Baltimore.
- Mazess RB. 1983. The Noninvasive Measurement of Skeletal Mass In: *Bone and mineral research Annual 1*. editor WA Peck. Excerpta Medica, Amsterdam.
- Mazess RB Cameron JR, Miller J. 1972. Direct readout of bone mineral content using radionuclide absorptiometry. *Int J Rad Isotopes* 23 471-479.
- Melton LJ and Riggs BL. 1983. Epidemiology of age-related fractures. In Avioli LV ed. *The Osteoporotic Syndrome*. Grune and Stratton. New York.
- Melton LJ, Wahner HW, Richelson LS, O'Fallon WM, and Riggs BL. 1986. Osteoporosis and the risk of hip fracture. *Am J Epid* 124 2 254-211.
- Mjoberg B, Brismar J, Hansson LI et al. 1985. Definition of endoprosthetic loosening. *Acta Orthop Scand* 56 469-473.

- Mjoberg B, Selvik G, Hansson LI et al. 1986. Mechanical loosening of total hip prosthesis. *J Bone Joint Surg* 68-B 770-774.
- Naor E, DiSeghni V, et al. 1972. Intra-observer variability in the determination of the metacarpal cortical index. *Br J Rad* 42 192-197.
- O'Neil DA, Harris WH. 1984. Failed total hip replacement: assessment by plain radiographs, arthrograms and aspiration of the hip joint. *J Bone Joint Surg* 66-A 540-546.
- Paterson M, Fulford P, Denham R. 1986. Loosening of the femoral component after total hip replacement. *J Bone Joint Surg* 68-B 392-397.
- Persliden J, Carlsson GU. 1986. Calculation of the small-angle distribution of scattered photons in diagnostic radiology using a Monte Carlo collision density estimator. *Med Phys* 13 19-24.
- Pratt WK. 1978. Digital image processing. Wiley and Sons. New York.
- Rao PS, and Gregg EC. 1975. Attenuation of monoenergetic gamma rays in tissues. *Am J Roentgenol* 123 631-637.
- Reiderer SJ, Kruger RA and Mistretta CA. 1981. Three Beam K-edge imaging of iodine using differences between fluoroscopic video images: theoretical considerations. *Med Phys* 8 471-479.
- Reiser UJ and Genant HK. 1984. Determination of bone mineral content in the femoral neck by QCT. *Radiology* 153 301.
- Riggs BI, Wahner HW, Seeman E, Offord KP, Dunn WL, Mazess RB, Johnson KA and Melton LJ. 1982. Changes in bone mineral density of the proximal femur and spine with aging. *J Clin Invest* 70 716-723.
- Rosner B. 1986. Fundamentals of biostatistics. Duxbury Press. Boston.
- Roos BO, Hansson TH, and Skoldborn H. 1980. Dual photon absorptiometry in lumbar vertebrae. *Acta Radiol Oncol* 19 111-114.

- Rowntree RR. 1985. Implementation of  $^{153}\text{Sm}$  in dual photon absorptiometry for the detection of BMC. M.Eng. Thesis. McMaster University.
- Rushton N, Coakley AJ, Tudor J, Wraight. 1982. The value of technetium and gallium scanning in assessing pain after total hip replacement. *J Bone Joint Surg* 64-B 313-318.
- Seitz P and Ruegsegger P. 1982. Anchorage of femoral implants visualized by modified computed tomography. *Arch Orthop Trauma Surg* 100 261-266.
- Smith MA, Sutton D, and Tothill P. 1983. Comparison between  $^{153}\text{Gd}$  and  $^{241}\text{Am}$ ,  $^{137}\text{Cs}$  for dual-photon absorptiometry of the spine. *Phys Med Biol* 28 709-721.
- Steinberg HA, Kalos MH. 1971. Bounded estimators for flux at a point in Monte Carlo. *Nucl Sci Eng* 44 406-412.
- Stevenson JC and Whitehead MI. 1982. Postmenopausal osteoporosis. *Br Med J* 285 585-588.
- Tothill P, Pye DW, and Teper J. 1987. The influence of extra-skeletal fat on the accuracy of dual photon absorptiometry. Sixth Int Workshop Bone Soft Tissue Densitometry. Buxton, England, 1987.
- Turner JE, Wright HA, Hamm RN. 1985. A Monte Carlo primer for health physicists. *Health Physics* 48 717-733.
- Uri G, Wellman H, Capello W, Robb J, Greenman G. 1984. Scintigraphic and X-ray arthrographic diagnosis of femoral prosthesis loosening: concise communication. *J Nucl Med* 25 661-663.
- Veigele WJ. 1973. Photon cross-sections for 0.1 keV to 1 MeV for elements  $z=1$  to  $z=94$ . *Atomic Data Tables* 5 51-111.
- Virtama P, Helena T. 1969. Radiographic measurements of cortical bone. *ACTA Orthopaedica Scandinavica Supplement*, 293.
- Vogel JM, Wasnich RD and Ross PD. 1988. The clinical relevance of calcaneous bone mineral measurements: a review. *Bone and Mineral* 5 35-58.

- Wahner HW. 1987. Single and dual-photon absorptiometry in osteoporosis and osteomalacia. *Sem Nucl Med* 17 4 305-315.
- Wahner HW, Dunn WL, Mazess RB, et al. 1985. Dual-Photon Gd-153 Absorptiometry of Bone. *Radiology* 156 203-206.
- Wahner HW, Dunn WL, Riggs BL. 1983. Noninvasive Bone Mineral Measurements. *Sem Nuc Med* 13 3 282-289.
- Wahner HW, Riggs BI, Readout JW. 1977. Diagnosis of osteoporosis: usefulness of photon absorptiometry at the radius. *J Nucl Med* 18 432-437.
- Wasserman SH Burzel US. 1987. Osteoporosis: The state of the art in 1987: A review. *Sem Nucl Med* 17 4 282-292.
- Watt DE. 1975. Optimum photon energies for the measurement of bone mineral and fat fractions. *Br J Rad* 48 265-274.
- Webber CE. 1981. Compton scattering methods. in Cohn SH ed. *Non-invasive measurements of bone mass and clinical application*. CRC Press. Florida.
- Webber CE. 1987. The effect of fat on bone mineral measurements in normal subjects with recommended values of bone, muscle and fat attenuation coefficients. *Clin Phys Physiol Meas* 8 143-158.
- Webber CE. 1988. Some factors which influence the evaluation of a dual photon measurement of lumbar spine bone mineral mass. *J Can Assoc Radiol*. In press.
- White DR and Fitzgerald M. 1977. Calculated attenuation and energy absorption coefficients for ICRP Reference Man (1975) organs and tissues. *Health Phys* 33 73-81.
- Willert HG, Semlitsch M. 1976. Reactions of the articular capsule to artificial joint prosthesis. in ed Williams D. *Biocompatibility of implant materials*. Sector Publishing. Tunbridge Wells, Kent.
- Williamson JF. 1987. Monte Carlo evaluation of Kerma at a point for photon transport problems. *Med Phys* 14 567.
- Wilson CR and Madsen M. 1977. Dichromatic absorptiometry of vertebral bone mineral content. *Invest Radiol* 12 180-184.

- Winter GD. 1976. Wear and corrosion products in tissues and the reactions they provoke. in ed Williams D. Biocompatibility of implant materials. Sector Publishing. Tunbridge Wells, Kent.
- Woo SL, Akeson WH, Coutts RD et al. 1976. A comparison of cortical bone atrophy secondary to fixation plates with large differences in bending stiffness. J Bone Joint Surg 58-A 190-195.
- Wood J. 1982. Computational methods in reactor shielding. Pergamon Press. Oxford.
- Wooten WW, Judy PF, Greenfield MA. 1973. Analysis of the effect of adipose tissue on the absorptiometric measurement of bone mineral mass. Inves Radiol 8 84-89.
- Zeitz L. 1972. Effect of subcutaneous fat on bone mineral content measurements with the single energy photon absorptiometry technique. Acta Radiologica Therapy. Phys Biol 11 401-410.

## APPENDIX 1

### STATISTICAL TESTS OF RANDOM NUMBER GENERATOR

Five different tests were performed on the generalized feedback shift register to determine both the validity of the algorithm and the initialization of the set of integers. These tests are described in detail by Lewis (1975), along with several other tests which could be performed, but a brief discussion of these tests will be given below.

The frequency test assesses the uniformity of the random number generator by determining the occurrence of numbers in sub-intervals of the interval 0-1 for a finite number of random numbers. One hundred sub-intervals were chosen with 10000 random numbers.

The serial test uses pairs of random numbers to fill a two-dimensional analog of the frequency test, that is filling sub-squares on the unit square. One hundred sub-squares were chosen with 10000 random numbers.

The gap test measures the length of gaps between successive occurrences in a given sub-interval such as in the frequency test. Ten sub-intervals were chosen, and the gaps between successive occurrences in the first subinterval were counted for 10000 random numbers.

The Yule's test consists of taking the sum of the decimal digits (the integer part of the multiple of the random number and 10) of 5 consecutive random numbers. The frequency of occurrence of these sums (on the range 0-45) was determined for 10000 random numbers.

The  $D^2$  test involves selection of two points randomly in the unit square (as in the serial test). The distribution of the square of the distance between the points was determined over 20 sub-intervals for 10000 random numbers.

Comparisons with expected distributions (as described by Lewis) are given for some of these tests in figure A1.1 and chi-squared values for deviations are given in table A1.1 with 5% probability levels from Rosner (1986). The random number generator passes all but the frequency test at the 5% probability level, but passes even this at the 2.5% probability level. The random number generator and the initialization seem to be adequate for use in the Monte Carlo simulation.

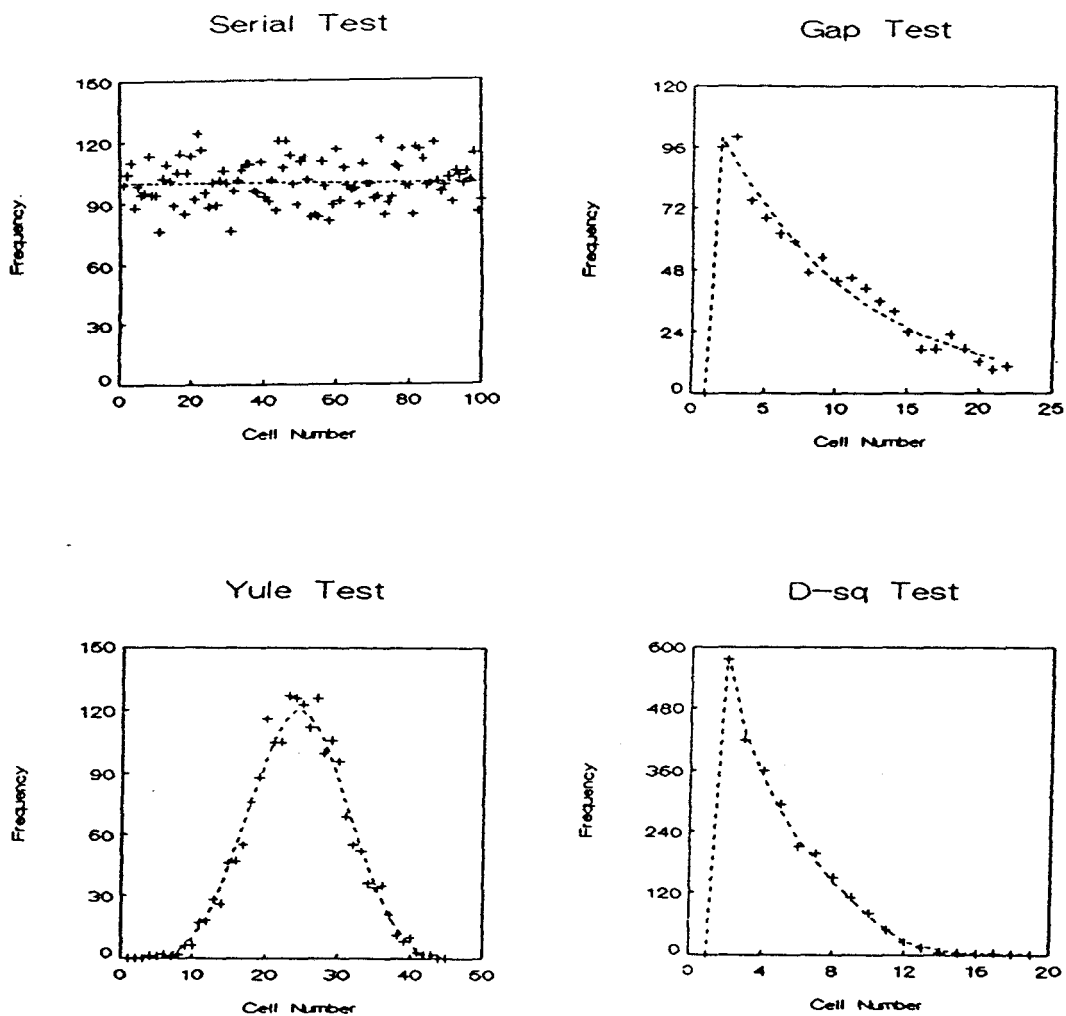


FIGURE A1.1 Frequency distributions for some Random number statistical tests including expected distributions.

Table A1.1 Chi-squared values for statistical tests of  
random number generator

Test	Degrees of Freedom	Chi-squared	5% Probability Levels
Frequency	99	74.38	77.93 - 124.34*
Serial	99	112.16	77.93 - 124.34
Gap	21	12.71	11.59 - 32.67
Yule	44	31.89	30.63 - 61.63
<sup>2</sup> D	19	10.86	10.12 - 30.14

\* 2.5% probability levels 74.22 - 129.56

## APPENDIX 2

### SIMULATION PROCESSES

#### A2.1 Photon Creation

Since the simulation involves determining the point source response, the photons all begin with the same state vector. The initial position of the photon is at the origin of the three dimensional Cartesian coordinate system with initial direction along the positive z axis. The initial weight of the photon is 1 and the initial energies of each photon are identical, a parameter input for each simulation.

#### A2.2 Path and Path Length Determination

The pathlength,  $s$ , is sampled by inversion of the normalized cumulative distribution of the pathlengths. If a material has a linear attenuation coefficient  $\mu$ , the distribution of pathlengths is given by

$$P(s) = \exp(-\mu s) \quad \text{A2.1}$$

and the normalized cumulative distribution is given by

$$C(s) = 1 - \exp(-\mu s) \quad \text{A2.2}$$

If a random number,  $R$ , is assigned to  $C(s)$ , then the pathlength is determined by inversion to be

$$s = -\ln(1-R)/\mu \quad \text{A2.3}$$

Since both  $R$  and  $1-R$  are uniformly distributed over the interval 0-1 an alternate form

$$s = -\ln(R)/\mu \quad \text{A2.4}$$

is used.

The linear attenuation coefficient will depend upon the energy of the photon as well as the material with which it interacts. The coefficient was found from a table of attenuation coefficients for integral values of photon energy in kev from 30 to 300 kev. For non-integral energies the attenuation coefficients are determined by linear interpolation. The table was filled by using a parametrization of the individual interaction mass attenuation coefficients (ie coherent, incoherent and photoelectric absorption) of the form

$$\ln(\mu/p) = \sum_{i=0}^4 a(i)E^i \quad \text{A2.5}$$

where  $E$  is the energy of the photon in kev. The coefficients for biological material were taken from White and Fitzgerald (1977) and for phantom materials from fitting cross-section from Hubbel et al (1975).

If the simulation included more than one material a single attenuation coefficient for a composite homogeneous mixture of the materials was used. The composite mass attenuation coefficient was given by

$$\mu/p = \sum w(i)\mu/p(i) \quad \text{A2.6}$$

where

$$w(i) = p(i)t(i)/MW(i) \quad \text{A2.7}$$

and  $p(i)$ ,  $t(i)$  and  $MW(i)$  are the density, thickness and molecular weight respectively of material  $i$ .

The position of the photon at a specific vertex is given by the Cartesian coordinates,  $(x,y,z)$ , and the direction of the photon is given by the direction cosines  $(\cos\theta_1,\cos\theta_2,\cos\theta_3)$ . The position of the next interaction vertex,  $(x',y',z')$  is given by

$$x' = x + s \cos\theta_1 \quad \text{A2.8a}$$

$$y' = y + s \cos\theta_2 \quad \text{A2.8b}$$

$$z' = z + s \cos\theta_3 \quad \text{A2.8c}$$

### A2.3 Determination of Interaction Type

At the energies used in these simulations the photon interactions which are possible include photoelectric absorption, Compton scattering and coherent scattering. For photoelectric absorption in biological materials as well as steel and vitallium the fluorescent X-rays are considered to have energies too low to be of interest, resulting in loss of the photon from the simulation. Rather than follow a photon for a long part of its history only to lose it in a photoelectric interaction, no photoelectric interactions are included. In order to remove the bias due to the loss of this interaction the weight of the photon is reduced by multiplication with the survival probability, which is the probability of Compton or coherent scattering divided by the total interaction probability. The survival probability is

obtained from a table similar to that for the linear attenuation coefficient using the partial interaction linear attenuation coefficients described earlier.

The scatter type is determined by choosing a random number,  $R$ , between 0 and 1. The ratio of the Compton scatter cross-section to the total scatter cross-section (the sum of the Compton and coherent cross section) is determined. If  $R$  is less than this ratio the photon is Compton scattered, and otherwise is coherently scattered. This ratio is also stored in a table similar to the linear attenuation coefficient which was obtained from the individual interaction linear attenuation coefficients. The determination of the scatter angle is described in the next sections.

#### A2.4 Coherent Scattering

Coherent scattering involves the scatter of the photon by the entire atom with no loss in energy of the photon. The differential scattering cross-section for a single electron is given by the Thompson cross-section

$$\frac{d\sigma(\text{Th})}{d\cos\theta} = \pi R_0^2 (1 + \cos^2 \theta) \quad \text{A2.9}$$

where  $R_0$  is the classical electron radius and  $\theta$  is the scattering angle. For the entire atom interference from individual electrons is possible, and the cross-section is multiplied by the square of the form factor  $FF(Z, \nu)$  where  $Z$

is the atomic number and  $v$  is the momentum transferred by the scattering process, given by

$$v = kE \sqrt{1 - \cos\theta} \quad \text{A2.10}$$

where  $E$  is the photon energy in electron rest mass units and  $k$  is a constant  $29.1433 \text{ cm}^{-1}$ . The coherent differential cross-section is given by

$$\frac{d\sigma(\text{Coh})}{d\cos\theta} = FF^2(Z, v) \frac{d\sigma(\text{Th})}{d\cos\theta} \quad \text{A2.11}$$

This is sampled to generate random scatter angles using the generalized rejection technique of Carter and Cashwell (1975). They showed that if  $v^2$  is sampled rather than  $\cos\theta$  the probability distribution of  $v^2$  is given by

$$P(v^2)dv^2 = C F^2(v^2) \frac{d\sigma(\text{Th})}{d\cos\theta} dv^2 \quad \text{A2.12}$$

where

$$F^2(v^2) = \frac{FF^2(Z, v^2)}{A(Z, v^2)} \quad \text{A2.13}$$

where  $v_m^2$  is  $v^2$  at  $\theta = \pi$ , and

$$A(Z, y) = \int_0^y FF^2(Z, v^2) dv^2 \quad \text{A2.14}$$

Tables of  $FF^2(Z, v)$  taken from Veigele (1973) were used to construct cumulative tables of  $A(Z, v^2)$  by numerical integration. At a given energy the value  $A(Z, v^2)$  was found and a random number,  $R$ , was used to select  $v^2$  by

$$A(Z, v^2) = R A(Z, v^2 m) \quad A2.15$$

and interpolating from the tables.

The scattering angle was determined by inverting equation 5.11 to give

$$\cos\theta = 1 - (v/kE)^2 \quad A2.16$$

where  $k=0.057$ , and  $E$  is the photon energy in kev. A rejection technique was used to include the Thompson cross-section. A random number,  $R$ , was used to accept the scattering angle if  $R < (1 + \cos \theta)/2$ , otherwise to choose a new  $v^2$ .

This sampling procedure was tested by generating 100,000 scatter angles and comparing with the expected distributions for water at 40, 100, 150 and 300 kev obtained from the differential cross-section. As seen in figure A2.1 the technique is valid for 40 and 100 kev, but is not as good for 150 and 300 kev. This is probably due to difficulty in determining the expected distributions for these energies rather than with the sampling technique since the scattering is highly forward peaked. This should not be a great problem since coherent scattering is not predominant at these energies.

### A2.5 Compton Scattering

Compton scattering involves elastic scattering of the photon by a free electron. The differential scattering

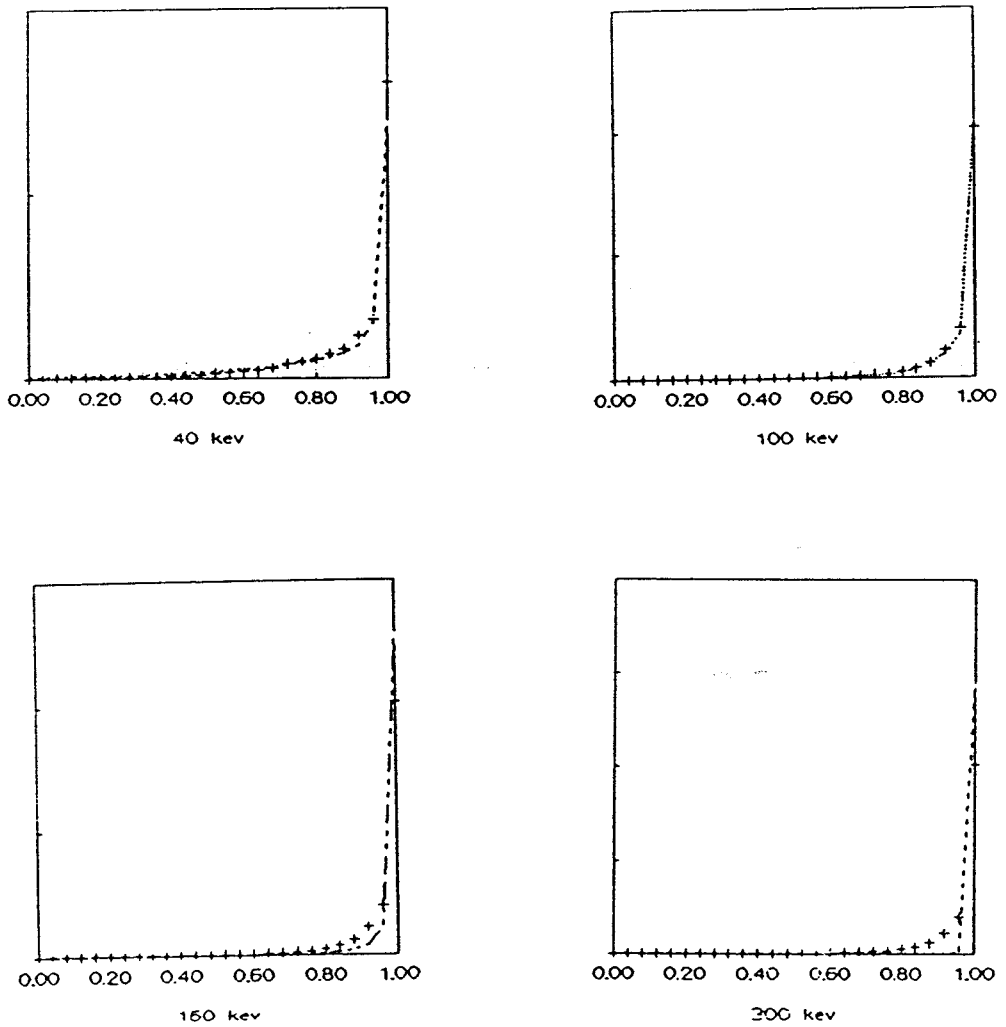


FIGURE A2.1 Frequency distributions generated by sampling Coherent scatter angle for water including expected distributions.

cross-section is given by the Klein-Nishini formula (Evans 1955)

$$\frac{d\sigma(\text{KN})}{d\cos\theta} = \pi R_0^2 \left( \frac{E'}{E} \right) \left[ \left( \frac{E'}{E} \right) + \left( \frac{E}{E'} \right) + \cos^2 \theta - 1 \right] \quad \text{A2.17}$$

where  $E$  and  $E'$  represent the photon energies in electron rest mass units before and after scattering respectively, and  $R_0$  is the electron radius as before. Energy and momentum are conserved, which gives the relation between  $E$ ,  $E'$  and scatter angle

$$E' = \frac{E}{1 + E(1 - \cos\theta)} \quad \text{A2.18}$$

For incoherent scattering, atomically bound electrons scatter the photon and the cross-section must be modified to include binding energies, especially at small scatter angles. The differential scatter cross-section is given by the Compton cross-section multiplied by a scattering factor  $I(Z, \nu)$ , with  $Z$  the atomic number and  $\nu$  the momentum transfer (as for coherent scattering), and is given as

$$\frac{d\sigma(\text{Inc})}{d\cos\theta} = I(Z, \nu) \frac{d\sigma(\text{KN})}{d\cos\theta} \quad \text{A2.19}$$

This is sampled using a modified rejection method, by first sampling the Compton cross-section to obtain  $\cos\theta$ , then choosing a random number,  $R$ , and accepting if  $R < I(Z, \nu) / I(Z, \nu_m)$ . The values of  $I(Z, \nu)$  were obtained from tables generated from data by Veigele (1973).

The Compton cross-section is difficult to invert, so it is sampled by a method due to Kahn (Wood 1982) which uses three random numbers to generate  $\cos\theta$ . The scheme of this method is indicated in figure A2.2.

This method was tested by generating 100,000 random scatter angles and comparing with the expected distributions for water at 40, 100, 150 and 300 keV obtained from the differential cross-section. As indicated in figure A2.3 the technique is valid over this energy range.

#### A2.6 Calculation of New Direction Cosines

The previous two sub-sections described the sampling of the cosine of the scattering angle,  $\theta_0$ , in the local reference frame of the photon; that is, the angle of scatter from the previous direction of travel. The azimuthal angle,  $\phi$ , is uniformly distributed over  $2\pi$  and is sampled by a rejection technique the scheme of which is given in figure A2.4 wherein the sine and cosine of  $\phi$  are generated. The new direction of the photon is given by the direction cosines  $\cos\theta_1'$ ,  $\cos\theta_2'$  and  $\cos\theta_3'$  which are found from spherical trigonometry using the scheme of Carter and Caswell (1975) by the following

$$\cos\theta_1' = \cos\theta_1 \cos\theta_0 + \frac{\sin\theta_0}{\sin\theta_3} [\cos\theta_1 \cos\theta_3 \cos\phi - \cos\theta_2 \sin\phi] \quad \text{A2.20a}$$

$$\cos\theta_2' = \cos\theta_2 \cos\theta_0 + \frac{\sin\theta_0}{\sin\theta_3} [\cos\theta_2 \cos\theta_3 \cos\phi + \cos\theta_1 \sin\phi] \quad \text{A2.20b}$$

$$\cos\theta_3' = \cos\theta_3 \cos\theta_0 - \sin\theta_3 \sin\theta_0 \cos\phi \quad \text{A2.20c}$$

```

 $\lambda \leftarrow 511/E$ 
Choose  $R_1, R_2, R_3$ 
if  $R_1 > \frac{(1+2/\lambda)}{(9+2/\lambda)}$  go to *

 $ER \leftarrow \frac{(1+2/\lambda)}{(1+2R_2/\lambda)}$ 

 $K \leftarrow \frac{2}{[(\lambda - ER\lambda + 1) + 1/ER] / 2}$ 

if  $R_3 > K$  then reject
go to **

*  $ER \leftarrow 1 + 2R_2/\lambda$ 

 $K \leftarrow 4 \left[ \frac{1}{ER} - \frac{1}{ER^2} \right]$ 

if  $R_3 > K$  then reject

**  $\cos\theta \leftarrow 1 + (1-ER)\lambda$ 

```

FIGURE A2.2 Scheme for random sampling Compton scattering angle due to Kahn.

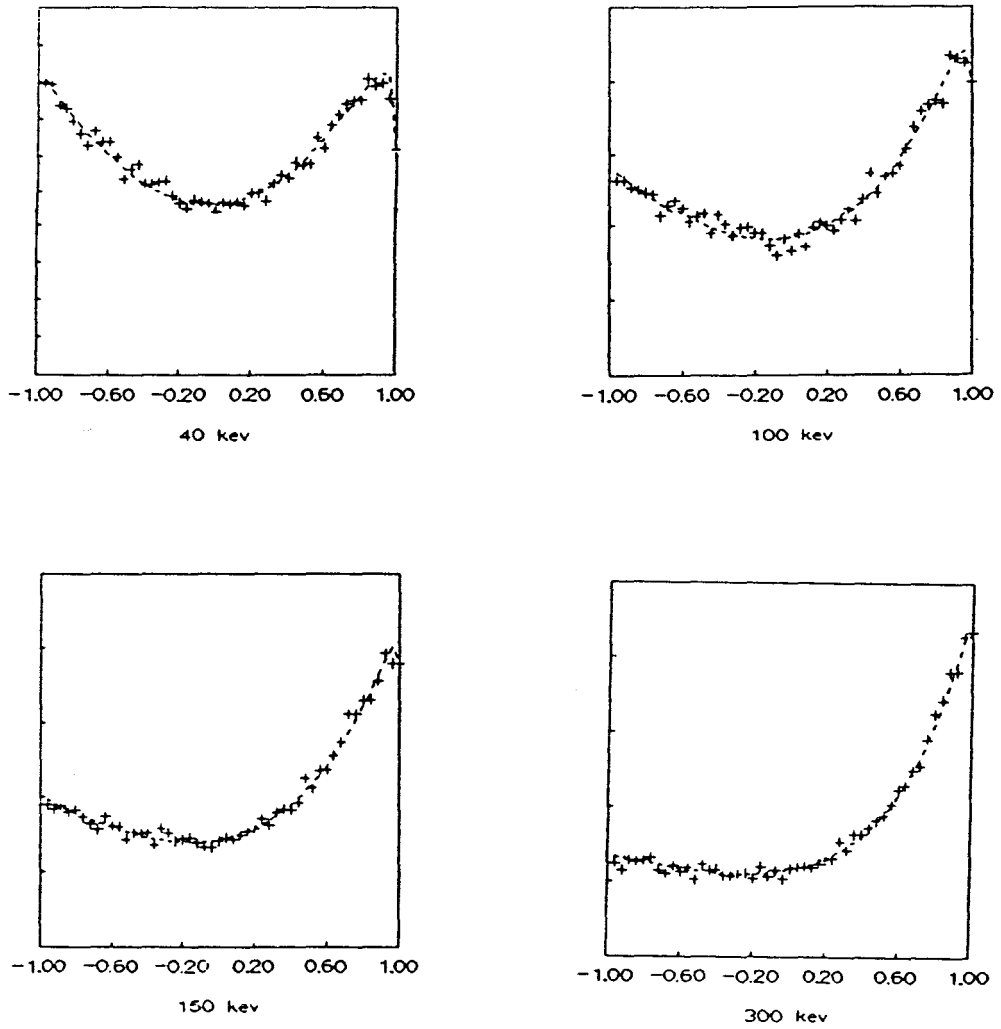


FIGURE A2.3 Frequency distributions generated by sampling incoherent scatter angle for water including expected distribution.

choose R1 R2 random numbers

$$x \leftarrow 2R1 - 1$$

$$y \leftarrow 2R2 - 1$$

$$r \leftarrow \sqrt{x^2 + y^2}$$

if  $r > 1$  then reject

$$\cos\phi \leftarrow x/r$$

$$\sin\phi \leftarrow y/r$$

FIGURE A2.4 Scheme for random sampling sine and cosine of azimuthal angle

If  $\cos\theta_3=0$  these are modified to the following form

$$\cos\theta_1' = \sin\theta\cos\phi \quad \text{A2.21a}$$

$$\cos\theta_2' = \sin\theta\sin\phi \quad \text{A2.21b}$$

$$\cos\theta_3' = \cos\theta\cos\theta_3/|\cos\theta_3| \quad \text{A2.21c}$$

### APPENDIX 3

#### BASIC CODE FOR MONTE CARLO SUBROUTINES

```

DIM TABLE(6,32): REM FORM FACTORS, ATOMIC SCATTERING FACTORS
DIM CRSX(6,300): REM ATTENUATION COEFFICIENTS
DIM CT(6): REM DIRECTION COSINES
REM  BINARY TABLE SEARCH TO FIND
REM  POSITION IT%
REM  GIVEN VALUE XT
TABLOOK: IT%=17: JT%=8
WHILE JT%>=1
IF TABLE(KT%,IT%)=XT THEN RETURN
IF TABLE(KT%,IT%)<XT THEN IT%=IT%+JT% ELSE IT%=IT%-JT%
JT%=JT%/2: WEND
IF TABLE(KT%,IT%)>XT THEN IT%=IT%-1
RETURN

REM  RANDOM NUMBER GENERATOR
REM  RETURNS RANDOM NUMBER XR ON (0,1)
REM  USING INITIALIZED SET RN%(31)
RAND: JR%=JR%+1: IF JR%>31 THEN JR%=1
KR%=JR%+13: IF KR%>31 THEN KR%=KR%-31
RN%(JR%)=RN%(JR%) XOR RN%(KR%)
IF RN%(JR%)=0 OR RN%(JR%)=XRM THEN GOTO RAND
XR=RN%(JR%)
XR=XR/XRM: RETURN

REM  DIRECTION CHANGE
REM  FINDS SINE AND COSINE OF AZIMUTHAL ANGLE (CP,SP)
REM  AND NEW DIRECTION COSINES (CT(4),CT(5),CT(6))
REM  GIVEN SCATTERING ANGLE CT0
REM  RETURNS DIRECTION AS CT(1),CT(2),CT(3)
ANGLES: GOSUB RAND
ANGLES1: P=2*XR-1: GOSUB RAND: Q=2*XR-1
CP=Q*Q+P*P: IF CP>1 THEN GOSUB RAND: GOTO ANGLES1
CP=SQR(CP): SP=Q/CP: CP=P/CP
ST0=SQR(1-CT0*CT0)
IF ABS(CT(3))>0.9999 THEN GOTO ANGLES2
ST=SQR(1-CT(3)*CT(3))
CT(4)=CT(1)*CT0+ST0*(CT(1)*CT(3)*CP-CT(2)*SP)/ST
CT(5)=CT(2)*CT0+ST0*(CT(2)*CT(3)*CP+CT(1)*SP)/ST
CT(6)=CT(3)*CT0-ST*ST0*CP
CT(1)=CT(4): CT(2)=CT(5): CT(3)=CT(6): RETURN
ANGLES2: CT(1)=ST0*CP: CT(2)=ST0*SP
CT(3)=CT0*CT(3)/ABS(CT(3))
RETURN

```

```

REM   SAMPLE COHERENT SCATTERING ANGLE
REM   RETURNS SCATTERING ANGLE CT0
COHER: VM=(0.080655*E)^2: REM MAXIMUM MOMENTUM TRANSFER
IF VM>36 THEN VM=36
KT%=1: XT=VM: GOSUB TABLOOK: REM FIND VM IN LOOKUP TABLE
Q=TABLE(2,IT%)+(VM-TABLE(1,IT%))*TABLE(5,IT%)*0.5
Q=TABLE(3,IT%)+Q*(VM-TABLE(1,IT%)): REM MAX INTEGRAL FORM
COHER1: GOSUB RAND: REM FACTOR SQUARED FFS
KT%=3: XT=XR*Q: GOSUB TABLOOK: REM SAMPLE INTEGRAL FFS
P=2*(XT-TABLE(3,IT%))/TABLE(5,IT%)
P=SQR(P+(TABLE(2,IT%)/TABLE(5,IT%))^2)+TABLE(2,IT%)/TABLE(5,IT%)
P=TABLE(1,IT%)-P: CT0=1-P/VM
GOSUB RAND: ST0=XR
P=(1+CT0*CT0)/2: IF ST0>P THEN GOTO COHER1: REM REJECTION
RETURN

```

```

REM   SAMPLING COMPTON SCATTER ANGLE
REM   RETURNS SCATTER ANGLE CT0 AND CHANGES THE ENERGY
REM   OF THE PHOTON
COMPT: VM=(0.080655*E)^2: REM MAX MOMENTUM TRANSFER
IF VM>36 THEN VM=36
KT%=1: XT=VM: GOSUB TABLOOK: REM POSITION OF VM IN TABLE
IZV=TABLE(4,IT%)+(VM-TABLE(1,IT%))*TABLE(6,IT%): REM ATOMIC
REM SCATTERING FACTOR ASF
E=E/511: REM ELECTRON REST MASS UNITS
COMPT1: GOSUB RAND
IF XR>(1+2*E)/(9+2*E) THEN GOTO COMPT2
GOSUB RAND: ER=1+2*XR*E: REM ER IS E/E(SCATTER)
GOSUB RAND
IF XR<=4*(1/ER-1/ER^2) THEN GOTO COMPT3 ELSE GOTO COMPT1
COMPT2: GOSUB RAND
ER=(1+2*E)/(1+2*XR*E): REM E/E(SCATTER)
GOSUB RAND
XCOM=((1/E-ER/E+1)^2+1/ER)/2
IF XR<=XCOM THEN GOTO COMPT3 ELSE GOTO COMPT1
COMPT3: CT0=1+(1-ER)/E: IF ABS(CT0)>0.9999 THEN GOTO COMPT1
E=E*511: REM BACK TO KEV
XT=(0.0570317*E)^2*(1-CT0): REM MOMENTUM TRANSFER OF SCATTER
KT%=1: GOSUB TABLOOK
P=TABLE(4,IT%)+(XT-TABLE(1,IT%))*TABLE(6,IT%): REM ASF
GOSUB RAND: IF XR>P/ST0 THEN GOTO COMPT1: REM REJECT
E=E/ER: EI%=INT(E): DE=E-EI%
RETURN

```

```

REM   CALCULATE PATHLENGTH S
PATH: P=CRSX(1,EI%)+DE*CRSX(4,EI%): REM TABLE OF ATTEN COEFF
GOSUB RAND: S=-LOG(XR)/P
RETURN

```

```

REM   DETERMINE SCATTER TYPE AND CHANGE WEIGHT
SCATTER: WT=WT*(CRSX(2,EI%)+DE*CRSX(5,EI%)): REM WEIGHT
P=CRSX(3,EI%)+DE*CRSX(6,EI%): GOSUB RAND: REM SCATTER RATIO
IF XR<=P THEN GOSUB COMPT ELSE GOSUB COHER: REM SCATTER
RETURN

```

```

REM   CALCULATE COHERENT DIFF CROSS-SECTION
REM   GIVEN SCATTER ANGLE
COHXS: XT=(1-CT0)*(0.0570317*E)^2: REM MOMENTUM TRANSFER
IF XT>36 THEN XT=36
KT%=1: GOSUB TABLOOK
XS=TABLE(2,IT%)+(XT-TABLE(1,IT%))*TABLE(5,IT%): REM FFS
XS=XS*(1+CT0*CT0): REM DIFF CROSS-SECTION * PI Ro^2
RETURN

```

```

REM   CALCULATE COMPTON DIFF CROSS-SECTION
REM   GIVEN SCATTER ANGLE
COMXS: XT=(1-CT0)*(0.0570317*E)^2: REM MOMENTUM TRANSFER
IF XT>36 THEN XT=36
KT%=1: GOSUB TABLOOK
XS=TABLE(4,IT%)+(XT-TABLE(1,IT%))*TABLE(6,IT%): REM ASF
P=1/(1+E*(1-CT0)/511): XE=P*E
XS=XS*(P^3+P^2*(CT0*CT0-1)+P): REM KLEIN-NISH FACTOR
RETURN

```

```

REM   CALCULATE DISTANCE AND DIRECTION AND SCATTER
REM   ANGLE TO SCORING POINT (S0,Y0,T)
FORANG: S=SQR((T-Z)^2+(X0-X)^2+(Y0-Y)^2): REM DISTANCE
CT(6)=(T-Z)/S: CT(5)=(Y0-Y)/S
CT(4)=(X-X0)/S: REM DIRECTION COSINES
CT0=CT(1)*CT(4)+CT(2)*CT(5)+CT(3)*CT(6): REM SCATTER ANGLE
P=CRSX(1,EI%)+DE*CRSX(4,EI%)
P=1/P: REM RESELECT LENGTH
IF S>=P THEN PRBSC0=1/S^2 ELSE PRBSC0=3/P^2
PRBSC0=PRBSC0*CT(6)*CRCOR: REM COMMON FOR COH AND COMPTON
RETURN

```

```

REM   CALCULATE COHERENT PROBABILITY
REM   GIVEN SCATTER ANGLE, DISTANCE, AND ENERGY
PRBCOH: P=CRSX(1,EI%)+DE*CRSX(4,EI%)
P=P*EXP(S1*P)
PRBSCT=PRBSC0/P: REM ALL BUT DIFF X-SEC.
GOSUB COHXS
PRBSCT=PRBSCT*XS: REM CRCOR IS 1/ATTEN COEFF* PI Ro^2
RETURN

```

```
REM   CALCULATE COMPTON PROBABILITY
REM   GIVEN SCATTER ANGLE, DISTANCE AND ENERGY
PRBCOM: P=CRSX(1,EI%)+DE*CRSX(4,EI%)
PRBSCT=PRBSC0/P
GOSUB COMXS: REM SCATTER ENERGY IS XE
EI1%=INT(XE): DE1=XE-EI1%
P=CRSX(1,EI1%)+DE1*CRSX(4,EI1%)
PRBSCT=PRBSCT*XS*EXP(-S1*P)
RETURN
```

## APPENDIX 4

### BASIC CODE FOR INTENSITY RATIO CALCULATION

```

rem generates sum of flux as function of radius in flx(45)
dim flx(45)
gosub rndini: rem random number generator initialization
tpi=8*atn(1)
input "radius of collimator (cm) ",rmax
input "collimator length (cm) ",cl
rmax2=rmax*rmax
input "number of points ",np%
for i%=1 to np%
gosub posit: rem position in source
gosub direc: rem direction of photon
gosub colint: rem intersection point of collimator exit
if r1>rmax2 then cyclend
gosub detint: rem intersection point at detector
r3=sqr(r2)
ir=int(r3*10)+1
flx(ir)=flx(ir)+1
cyclend: next i%
end
posit: gosub rand: z=xr
posit1: gosub rand: x=(2*xr-1)*rmax
gosub rand: y=(2*xr-1)*rmax
r=x*x+y*y: if r>rmax2 then posit1 else return
direc: gosub rand: ct=1-.019*xr
gosub rand: phi=tpi*xr
st=sqr(1-ct*ct)
cty=st*sin(phi)
ctx=st*cos(phi)
return
colint: dz=cl+z: s=dz/ct
x1=x+ctx*s: y1=y+cty*s
r1=x1*x1+y1*y1
return
detint:s=(17.5+cl)/ct
x2=x1+s*ctx: y2=y1+s*cty
r2=x2*x2+y2*y2
return

```

APPENDIX 5  
CONVOLUTION OF CIRCULARLY SYMMETRIC FUNCTION  
WITH A UNIFORM CIRCLE

In the Monte Carlo simulations the flux probability for a pencil beam was assumed to be a radial function with no dependence on azimuthal angle. The flux probability for a finite beam will be given by the convolution of the pencil beam flux probability with the flux density of the beam at the source collimator. This density was assumed to be uniform over a circle of radius equal to the radius of the collimator with density equal to the reciprocal of the area of the collimator. In this way the convolved flux density will be normalized by the number of photons in the entire beam.

The most obvious approach to perform the convolution would be to generate two dimensional sets of data corresponding to the radial functions for the pencil beam flux probability and the beam flux density and to convolve these either by direct calculation or by using Fourier transforms. A quicker and more elegant (in my opinion) approach was to calculate the radial function of the convolution directly using the two known radial functions. This involved considering the two dimensional flux

probability to be composed of several uniform rings of different diameters and heights. The convolution of the entire radial function with the uniform circle is then the sum of the convolutions of the rings with the uniform circle.

The convolution of a ring with a uniform circle can be determined by considering the effect of convolving a point with a uniform circle. In figure A5.1a a ring of radius  $R_1$  and thickness  $\Delta R_1$  is convolved with a circle of radius  $R_2$ . The point  $P_1$  will be uniformly spread over the circle surrounding it, so that the contribution of the point  $P_1$  to any point within the circle, say  $P_2$ , will be the reciprocal of the area of the circle,  $1/\pi R_2^2$ . For an arbitrary point at a position  $R_3$  the convolution,  $C(R_3)$ , will be the integral of the contribution from all points on the ring which fall within a circle of radius  $R_2$  about that point. This will be given by the product of the area of the ring within the circle and the contribution from each point, that is

$$C(R_3) = \frac{\text{Area}}{\pi R_2^2} \quad \text{A5.1}$$

If  $R_1$  is greater than  $R_2$  then the area is zero when  $R_3$  is less than  $R_1 - R_2$  or when  $R_3$  is greater than  $R_1 + R_2$ . Otherwise the area is given by the product of the arc length,  $2R_1\phi$ , and thickness,  $\Delta R_1$ , of the portion of the ring

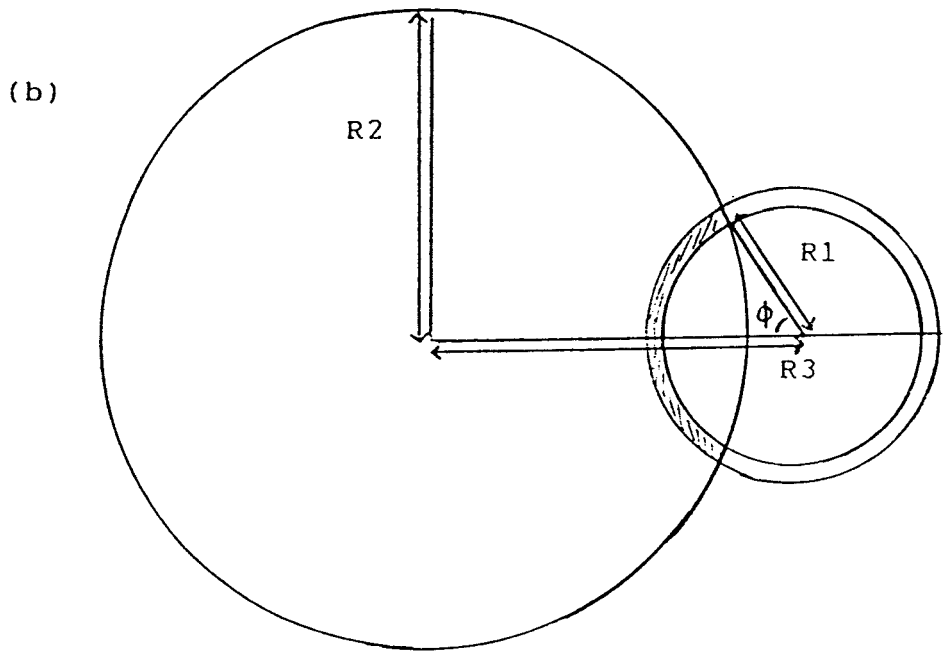
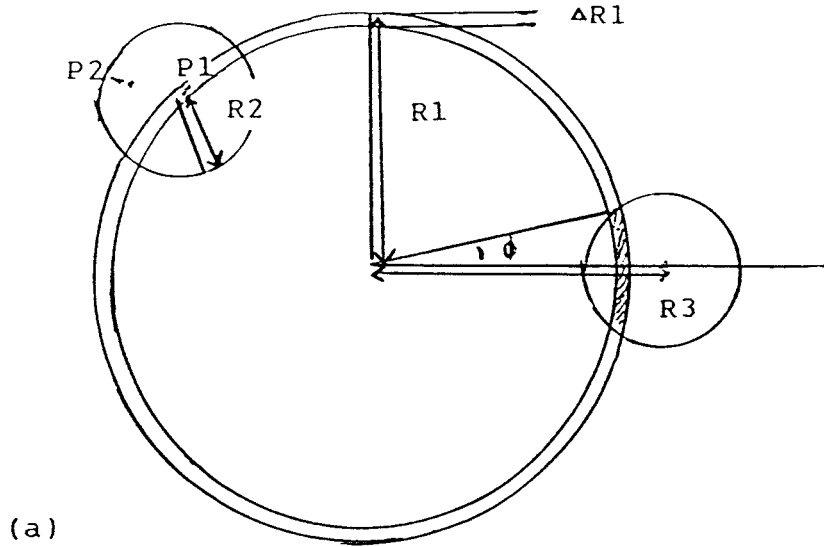


FIGURE A5.1 Evaluation of convolution of a ring with a uniform circle when the radius of the ring is greater than the circle (a) and when the radius of the ring is less than the circle (b).

in the circle.

If  $R_2$  is greater than  $R_1$ , as indicated in figure A5.1b then the area is zero when  $R_3$  is greater than  $R_1+R_2$  and if  $R_3$  is less than  $R_2-R_1$  the area is  $2\pi R_1 \Delta R_1$ . For other values of  $R_3$  the area is given by the product of the arc length and thickness as above.

The convolution at a radius  $R_3$  is given by the following expressions

Case 1:  $R_1 > R_2$

$$C(R_3) = 0 \quad R_3 < R_1 - R_2$$

$$C(R_3) = \frac{2R_1 \pi \Delta R_1}{2\pi R_2} \quad R_1 - R_2 < R_3 < R_1 + R_2$$

$$C(R_3) = 0 \quad R_1 + R_2 < R_3$$

Case 2:  $R_2 > R_1$

$$C(R_3) = \frac{2R_1 \pi \Delta R_1}{2\pi R_2} \quad R_3 < R_2 - R_1$$

$$C(R_3) = \frac{2R_1 \pi \Delta R_1}{2\pi R_2} \quad R_2 - R_1 < R_3 < R_2 + R_1$$

$$C(R_3) = 0 \quad R_2 + R_1 < R_3$$

Examples of the radial convolutions are given in figure A5.2 for cases with  $R_1$  greater than  $R_2$  and  $R_1$  less than  $R_2$ .

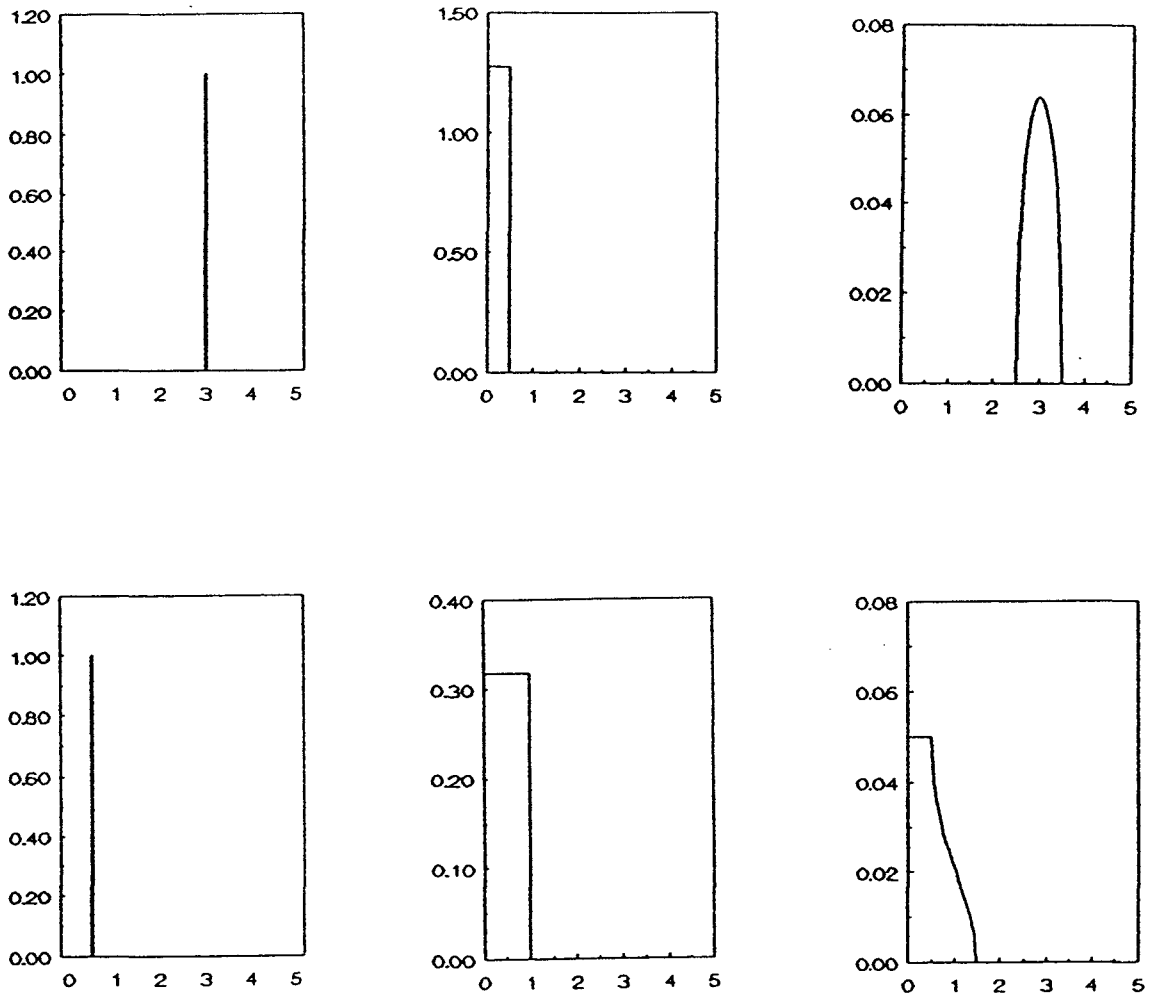


FIGURE A5.2 Plots of radial functions from left to right of a ring with unit height, a uniform circle and the convolution of the ring and the circle. These are shown for radius of the ring greater than for the circle (upper) and for the radius of the ring less than the circle (lower).

## APPENDIX 6

### GEOMETRIC EFFICIENCY OF DETECTOR WITH PHOTON ANGLE

The results of the Monte Carlo simulations were distributions of flux probabilities as a function of radius and photon direction. It was assumed that the multiply scattered photons would have azimuthal symmetry in their direction and that the polar angle would be sufficient to describe the direction. For an arbitrary position at the entrance of the detector collimator at a given polar angle the flux probability is uniform over a cone with apex equal to the polar angle, and the photons will strike the detector in a circle which is the intersection of the cone with the plane of the detector. This is illustrated in figure A6.1.

As is evident from figure A6.1 the intersection of the cone with the detector plane will include paths through the collimator itself, which must be discounted. The angular response is the fraction of photons at a radius,  $r$ , with polar angle,  $\theta$ , which hit the detector without hitting the collimator. This was the fraction of the circle which intersects the circle of the detector collimator as in figure A6.1. This was determined simply as the ratio of the arc length within the collimator divided by the entire circumference of the circle.

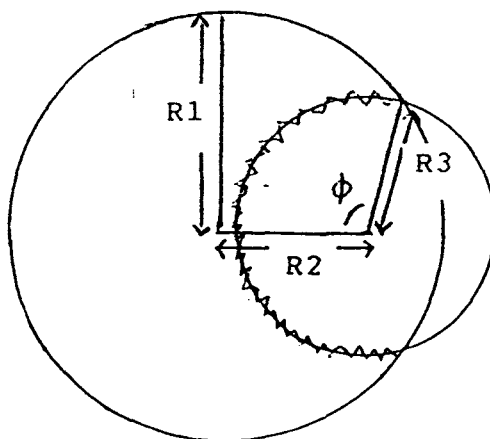
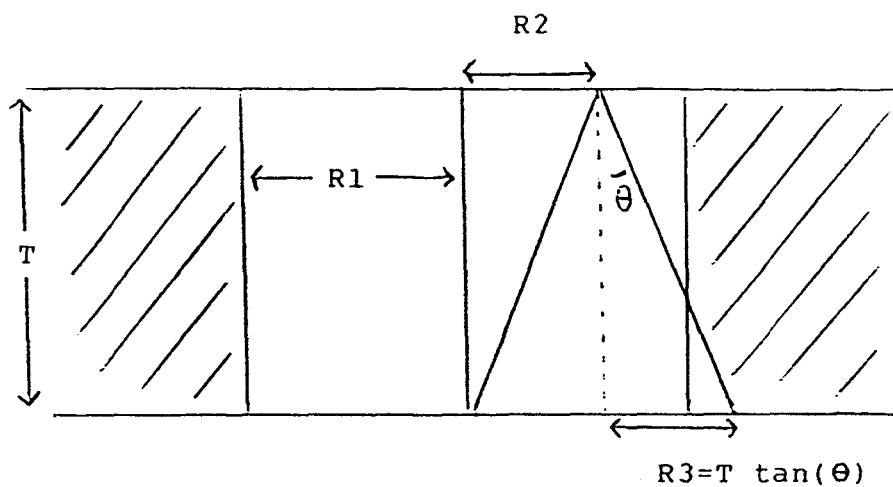


FIGURE A6.1 Evaluation of geometric efficiency of detector collimator of radius  $R_1$  for a point at  $R_2$  with polar direction  $\theta$ . The upper diagram indicates the cone of directions with polar angle  $\theta$  while the lower diagram shows the overlap of the intersection of the cone with the detector plane and the detector collimator (  ). The efficiency will be given as  $\phi/\pi$ .